REAL-TIME IMAGING SYSTEM FOR A GROUND PENETRATING RADAR

BY

EDUARDO ROGELIO CORRAL SOTO

A Thesis Submitted to the Faculty of Graduate Studies in Partial Fulfillment of the Requirements for the Degree of

MASTER OF SCIENCE

Department of Electrical and Computer Engineering
University of Manitoba
Winnipeg, Manitoba, Canada

THE UNIVERSITY OF MANITOBA

FACULTY OF GRADUATE STUDIES

*****

COPYRIGHT PERMISSION PAGE

REAL-TIME IMAGING SYSTEM FOR A GROUND PENETRATING RADAR

BY

Eduardo Rogelio Corral Soto

A Thesis/Practicum submitted to the Faculty of Graduate Studies of The University of Manitoba in partial fulfillment of the requirements of the degree of

Master of Science

Abstract

This thesis introduces an imaging system that generates two-dimensional radar images in real time for the detection of shallow buried objects in homogeneous sand. Although metal detectors are available for locating buried metal-made objects, they are not effective with non-metallic objects, such as plastic landmines. Hence, the use of a ground penetrating radar (GPR) is more suitable for this application, in which microwave signals penetrate into the ground until a buried object reflects them back and the reflected signals are sampled and processed in order to extract information about the object's depth and reflectivity. The main imaging problem is that the plastic dielectric constant is close to that from the sand, which causes a small contrast between their reflections. Furthermore, the reflected signals contain information from the ground surface and other buried objects that obscure the reflections from the targeted object. Therefore, in order to contribute to the development of practical systems for detecting buried non-metallic objects, a signal processing algorithm was developed in this work. The algorithm generates complex range profiles by applying the Inverse Fourier Transform (IFFT) to the data and corrects the position shift of the scatterers due to the GPR system delay. Afterwards, the first difference is applied to the data in order to enhance the final image and discriminate the response transitions between the targeted object and the sand. In order to improve resolution, a synthetic array (SAR) is formed as the GPR moves to the next position. Azimuth compression is applied followed by integration in order to generate a focused image column. The reflections of the surface are removed adaptively and an adaptive subtraction is performed between the new column and a stored reference with the objective of emphasizing the responses of the buried object. A sandbox was built, and the algorithm was implemented in order to form an updated image at each antenna position. The results obtained indicate that the imaging system is capable of generating real time images of buried objects, which provide accurate information about their depth and location. The final images showed better visual quality than images obtained using other clutter reduction techniques.

Keywords: Ground penetrating radar, digital signal processing, real-time image formation, synthetic aperture radar, object recognition.

Acknowledgements

The author wants to gratefully thank his research advisor Dr. Gabriel Thomas for his encouragement, support, guidance and comments during the time when this research was conducted. In addition many thanks are given to Dr. Joe LoVetri for his criticism and suggestions to this project and his support provided in the laboratory. Many thanks are given to Dr. Ian Ferguson for criticizing the thesis and for providing important feedback. This research project has been greatly aided by Mike Phelan and Su Hong with the construction of the wooden sandbox and by Scott Peters and Arturo Solis with the implementation of the motorized mechanism and circuit. Thanks are given to the technical group of the Electrical and Computer Engineering department for supplying all of the necessary materials and help, such as the GPIB Ethernet interface and the antenna's arm mechanism.

Table of Contents

List of Tables.

List of Figures.

List of Acronyms.

A/D, ADC	Analog-to-Digital Converter
DC	Direct Current
DSK	DSP Software Development Kit
DSP	Digital Signal Processing
EEPROM	Electrically Erasable Programmable Read Only Memory
EVM	Evaluation Module
GHZ	Giga Hertz
GPIB	General Purpose Instrument Bus
GPR	Ground Penetrating Radar
GUI	Graphical User Interface

I2C	Inter-Integrated Circuit
IDE	Integrated Design Environment
IF	Intermediate Frequency
IFFT	Inverse Fast Fourier Transform
I/O	Input/Output
IQ	Inphase and Quadrature
LO	Local Oscillator
MHZ	Mega Hertz
MSE	Mean Square Error
NDT	Non-destructive testing
PC	Personal Computer
RADAR	Radio Detection and Ranging
RF	Radio Frequency
RTDX	Real Time Data Exchange
SAR	Synthetic Aperture Radar
SFCW	Stepped Frequency Continuous Wave
TX/RX	Transmitter/Receiver
VCO	Voltage Controlled Oscillator

List of Symbols.

α	Angle between antenna center and reflecting point.
β	Bandwidth.
Γ	Reflection coefficient.
δR	Quadratic distance from SAR array center to a given point.
Δf	Frequency step.
Δd_c	Length of the cross-range step.
Δr_c	Cross-range resolution.
Δr_s	Range resolution.
ε	Permitivity of the medium.
ε_o	Permitivity of free-space.
γ	Complex propagation constant.
η	Wave impedance.
θ	Phase shift.
λ	Wavelength.
λ_c	Wavelength of the center frequency.
μ	Permeability of the medium.
μ_o	Permeability of free-space.
π	Pi.
ρ	Electric charge density.
σ	Conductivity of the medium.
ϕ	Real part of the propagation constant (Attenuation rate).

ψ	Imaginary part of the propagation constant (Phase shift).
χ_e	Electric susceptibility.
χ_m	Magnetic susceptibility.
ω	Radian frequency.
a_p	The *pth* prediction coefficient.
$\overline{B}$	Magnetic flux density.
c	Propagation speed.
c_{sand}	Propagation speed in sand.
$c_{a_{n,m}}$	Homogeneous part of the clutter.
$c_{b_{n,m}}$	Non-homogeneous part of the clutter.
d_{as}	Distance between antenna and the surface.
d_c	Length of the synthetic antenna.
d_{int}	Depth of interest.
$d_{\max}$	Maximum distance to be mapped in the image.
d_s	Distance between antenna and object.
d_{syst}	Distance which includes the GPR internal and external cables.
d_x	Horizontal distance between the center of antenna and the object
d_z	Distance used to estimate the location of the surface.
$\overline{D}$	Electric flux density.
E	Correction exponential vector.
$\overline{E}$	Electric field intensity.
$\overline{E}_i$	Incident electrical field.
$\overline{E}_r$	Reflected field.
$E_{sar\,k,l}$	Correction exponential matrix .
$\overline{E}_t$	Transmitted field.
f	Frequency.
fi	Intermediate frequency.
f_{end}	End frequency.
fl	Local oscillator frequency.
f_o	Initial frequency.
F	Final output image.
$\overline{H}$	Magnetic field intensity.
I	Inphase component.
j	Imaginary part of a complex number (square root of -1).
$\overline{J}$	Electric current density.
k	Integer number (index).
κ	Wavenumber.
l	Integer number (index).

$M^{'}$	Range migration.
$\overline{M}$	Fictitious magnetic current density.
N	Number of data points.
l_{ant}	Length of the real antenna,
L	Number of columns in the SAR array.
p	Predictor order.
$\overline{P_e}$	polarization of the atoms.
Q	Quadrature component.
R	Range from SAR array center to a given point.
$rMSE$	Mean square error between the new column and reference column.
T_1	Threshold for energy transitions detection.
T_2	Threshold for similarity between the new column and reference.
S	Sampled complex data vector.
$sar_{n,l}$	Synthetic aperture array.
$sar_{f\,n,l}$	Corrected SAR array.
$sbin$	Estimated range bin of the sand surface.
$s_{cder\,n,m}$	First difference applied in cross-range.
$s_{cmp\,n}$	Azimuth-compressed complex range profile.
S_{corr}	Phase-corrected signal.
s_{corr}	Complex range profile.
s_{cf}	Vector containing the range bins of interest.
$s_{der\,n}$	First difference vector applied in the range direction.
$sMSE$	Mean square error between adjacent range profiles.
$s_{ref\,n}$	Reference column.
S_t	Transmitted signal.
$s_{sub\,n,m}$	Subtraction column.
$\hat{S}(k)$	Extrapolated signal.
t	Time.
$t_{n,m}$	Contribution of a known target under search.
T	Transmission coefficient.

1. Introduction

Ground Penetrating Radar (GPR) technology is being widely adopted in many civil applications such as in geological, environmental and glaciology engineering and construction, archeology and forensic science fields [1], [2], [19]. In this technology, microwave signals penetrate into the ground until a buried object reflects them back. The reflected signals are then sampled and processed in order to extract valuable information about the buried objects, such as depth and reflectivity. GPR applications can be divided into two main classifications: *i)* Geological applications, in which the depth of penetration tends to be more important than fine resolution, and *ii)* Engineering or non-destructive testing (NDT) applications, in which fine resolution is required. In geological applications, pulsed GPR systems are often used in which a train of very short-duration pulses in the order of nanoseconds is transmitted and the received signals are sampled in the time domain. Because of the short duration of the pulses, they have to be transmitted with a very high peak power in order to be able to penetrate into the medium, return to the receiver and be detected. When fine range resolution is required, the whole system including acquisition and antennas must have a bandwidth that satisfies the required resolution, which in practice implies a complex and high-cost system design. An alternative type of GPR system, which is used in this thesis in order to detect buried objects in sand, is the Stepped Frequency Continuous Wave (SFCW) system which removes the requirements of a wide instantaneous bandwidth and high sampling rates. Unlike the pulsed system, the sampling is performed in the frequency domain in which a series of microwave pulses are transmitted stepped in frequency from pulse to pulse over a defined bandwidth. The duration of each transmitted frequency component needs to be sufficient to produce a steady-state echo response at the receiver, in which the received signals are down-converted into baseband signals that can be sampled at low rates in order to synthesize a time domain range profile by the use of the Fourier Transform (FT). Thus, measurements of a target's echo signal in the time and frequency domains provide equivalent data for determining valuable information about the buried targets. If a SFCW GPR is used to transmit one train of signals at each ground location as shown in Figure 1.1, then by analyzing and processing the phase shifts and magnitudes of the received

signals, the responses of the reflecting objects at different depths in the sand and at different antenna positions can be obtained and a GPR image can be formed.

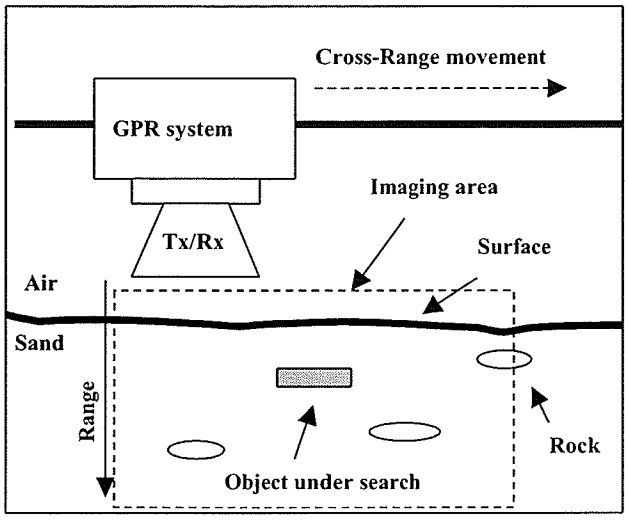

Figure 1.1 GPR scanning a sand region that contains buried objects.

The goal of this work is to contribute to the development of practical systems for the generation of images of small shallow buried objects. Specifically, the thesis is focused on the detection of plastic landmines with dimensions in the order of 15cm, that are buried in homogeneous sand at depths of 2 to 10cm. The main problem is that the dielectric constant of plastic is close to that from the sand, which causes a small contrast between their reflections. Furthermore, the reflected signals contain information from the ground surface and other buried objects that obscure the reflections from the targeted object. Algorithms for detection of buried objects by clutter reduction can be found in the literature, in which a scan is performed on a region of the ground that does not contain any buried object. The obtained complex average data is subtracted from the new collected data at each position [13], or the complex data matrix is subtracted from a new data matrix obtained at several positions of an area of the ground in which an object may be present [5]. There are other algorithms that reduce clutter by estimating the unwanted responses using models in an iterative fashion [3]. Although these algorithms are

effective, the drawbacks are that the stored reference complex matrix obtained at a specific location may not be suitable to be subtracted from data obtained at other locations due to changes in the ground characteristics. On the other hand, the iterative algorithms require intensive computations, and they are not suitable for real time implementation. This thesis presents an algorithm that was developed and implemented in order to generate an image as the GPR moves in the cross-range direction. The algorithm makes use of the synthetic aperture radar (SAR) approach in order to improve the cross-range resolution and to focus the array by applying azimuth compression. It also applies the first difference as well as an adaptive reference subtraction in order to emphasize the responses of the buried plastic landmine. A pre-recorded signature of the object is stored in memory, and it is used to attempt to recognize its presence under the ground by the use of fast correlation and the mean square error. This work presents the basic theory of plane waves reflection and the analysis of an existing stepped-frequency GPR system as well as practical aspects of SAR and GPR design. The real time implementation and experiments are presented in the later sections.

1.1 Problem definition

Based on the previously explained background, the main problem attacked in this thesis is the imaging of a weak reflecting object (specifically a plastic landmine) buried in sand. This problem encompasses the removal of the sand's surface response that obscures the presence of the landmine, and the enhancement of the buried landmine's response.

1.2 Contribution

The main contribution of this thesis is the development of an algorithm and its implementation in real time, which processes each incoming data vector obtained at each GPR ground location and generates a two-dimensional image which contains the enhanced responses of a weak-reflecting buried plastic landmine. The algorithm includes a method to remove the strong responses from a rough surface, as well as a method to enhance the responses of the buried objects by the use of an adaptive reference subtraction. The results of a set of laboratory experiments indicate that the algorithm works effectively in generating real time GPR images of a buried landmine. Other

contributions are the presentation of a technique that attempts to improve the range resolution by extrapolating the data, and the application of focusing methods used in airborne radar into GPR images.

2. Basic Plane Wave Reflection Theory

Although the analysis of the physical scattering mechanisms that occur inside the sand where the signals are reflected is not presented in this work, it is necessary to have a basic understanding of the characteristics of the medium, and how the signals travel and are reflected when a medium interface is present. This section presents the basic theory of plane wave reflection from a lossy medium interface. A more detailed explanation can be found in [6].

The electromagnetic properties of materials are related to their composition, which directly controls the propagation speed and the attenuation of electromagnetic waves traveling through them. When two materials with different properties are adjacent, a contrast between their relative dielectric constants gives rise to reflection when an incident wave travels from one material towards a second one.

As the first step for the discussion of this basic electromagnetic theory, the Maxwell equations in phasor form are presented as

$$\nabla \times \overline{E} = -j\omega\overline{B} - \overline{M}, \tag{2.1}$$

$$\nabla \times \overline{H} = j\omega\overline{D} + \overline{J}, \tag{2.2}$$

$$\nabla \cdot \overline{D} = \rho, \tag{2.3}$$

$$\nabla \cdot \overline{B} = 0. \tag{2.4}$$

Where

$\overline{E}$ is the electric field intensity.

$\overline{H}$ is the magnetic field intensity.

$\overline{D}$ is the electric flux density.

$\overline{B}$ is the magnetic flux density.

$\overline{M}$ is the (fictitious) magnetic current density.

$\overline{J}$ is the electric current density.

ρ is the electric charge density.

The electric and magnetic current sources are $\overline{J}$ and $\overline{M}$.

If an electric field $\overline{E}$ is applied to a dielectric material, then a polarization of the atoms of the material is generated. This polarization $\overline{P}_e$ generates dipole moments that cause an electric displacement flux $\overline{D}$. When $\overline{P}_e$ is in the same direction as $\overline{E}$, it is said that the material is isotropic. The total displacement flux $\overline{D}$ is expressed as

$$\overline{D} = \varepsilon_o \overline{E} + \overline{P}_e . \tag{2.5}$$

Where $\varepsilon_o = 8.854 \times 10^{-12}$ F/m is the permitivity of free-space.

In a linear medium the electric polarization $\overline{P}_e$ is related to the electric field as

$$\overline{P}_e = \varepsilon_o \chi_e \overline{E} , \tag{2.6}$$

where χ_e is known as the electric susceptibility, and can be a complex number.

If $\overline{P}_e$ is substituted in (2.5) then

$$\overline{D} = \varepsilon_o \overline{E} + \varepsilon_o \chi_e \overline{E} , \tag{2.7}$$

$$\overline{D} = \varepsilon_o (1 + \chi_e) \overline{E} , \tag{2.8}$$

where the factor

$$\varepsilon = \varepsilon_o (1 + \chi_e) \tag{2.9}$$

is known as the *permitivity* of the medium, which may be complex and its imaginary part accounts for the loss in the medium (heat) due to damping of the vibrating dipole moments. When the permitivity is real, then the medium is lossless, such as the case of free-space. In a similar way, if a magnetic field $\overline{H}$ is applied to a magnetic material, then magnetic dipole moments may be aligned in the material, causing a magnetic polarization. This polarization $\overline{P}_m$ (magnetization) generates a magnetic flux $\overline{B}$ as

$$\overline{B} = \mu_o (\overline{H} + \overline{P}_m), \tag{2.10}$$

where $\mu_o = 4\pi \times 10^{-7}$ H/m is the free-space permeability.

In a linear medium the magnetic polarization $\overline{P}_m$ is related to the magnetic field as

$$\overline{P}_m = \chi_m \overline{H} , \tag{2.11}$$

where χ_m is known as the magnetic susceptibility, and can be a complex number.

If $\overline{P}_m$ is substituted in (2.10) then

$$\overline{B} = \mu_o(1+\chi_m)\overline{H}, \tag{2.12}$$

where the factor

$$\mu = \mu_o(1+\chi_m), \tag{2.13}$$

is known as the *permeability* of the media, and its imaginary part accounts for the loss in the medium due to damping forces.

The electromagnetic properties of a medium can be characterized by its permitivity ε, permeability μ, and conductivity σ. For example, the permeability and permitivity for aluminum are obtained respectively as $\varepsilon = (1)\cdot\varepsilon_o$, and $\mu = (2000)\cdot\mu_o$. For lossy media, ε has an imaginary part, which accounts for loss, whereas for lossless media, it is a real number.

2.1 Plane waves traveling in a general lossy medium

If the conductivity σ of a medium is different than zero, then the medium is lossy. Hence the Maxwell's equations can be written as

$$\nabla \times \overline{E} = -j\omega\mu\overline{H}, \tag{2.14}$$

$$\nabla \times \overline{H} = j\omega\varepsilon\overline{E} + \sigma\overline{E}. \tag{2.15}$$

Which can be used to obtain the following equation for $\overline{E}$

$$\nabla^2\overline{E} + \omega^2\mu\varepsilon\left(1 - j\frac{\sigma}{\omega\varepsilon}\right)\overline{E} = 0, \tag{2.16}$$

and

$$\kappa^2 = \omega^2\mu\varepsilon\left(1 - j\frac{\sigma}{\omega\varepsilon}\right), \tag{2.17}$$

where κ is known as the wave number.

Note that if the media were lossless, the conductivity σ would be zero and then $\kappa^2 = \omega^2\mu\varepsilon$. From (2.16), a complex propagation constant $\gamma = j\kappa$ is defined as

$$\gamma = j\omega\sqrt{\mu\varepsilon}\sqrt{1 - j\frac{\sigma}{\omega\varepsilon}}, \tag{2.18}$$

which has a real and imaginary part

$$\gamma = \phi + j\psi. \tag{2.19}$$

Then if (2.18) is substituted in (2.16), we obtain

$$\nabla^2 \overline{E} - \gamma^2 \overline{E} = 0. \tag{2.20}$$

Assuming that the electric field is aligned with the x–axis, parallel to the surface of the medium according to Figure 2.1,

$$\nabla^2 \overline{E}_x + \gamma^2 \overline{E}_x = 0, \tag{2.21}$$

which has solutions

$$E_x(z) = E^+ e^{-\gamma z} + E^- e^{\gamma z}. \tag{2.22}$$

It can be noticed that the positive traveling wave has a propagation factor

$$e^{-\gamma z} = e^{-\phi z} e^{-j\psi z}, \tag{2.23}$$

which in the time domain has the form

$$e^{-\phi z} \cos(\omega t - \psi z). \tag{2.24}$$

This represents a plane wave traveling in the z direction. It is weighted by a decaying exponential that attenuates it with distance, at a rate of ϕ.

In a similar way, an expression can be obtained from the point of view of the magnetic field $\overline{H}$ as follows

$$H_y = \frac{1}{\eta}\left(E^+ e^{-\gamma z} - E^- e^{\gamma z}\right), \tag{2.25}$$

where η is called the wave impedance

$$\eta = \frac{j\omega\mu}{\gamma}. \tag{2.26}$$

The wavelength in terms of ψ (the imaginary part of γ) is

$$\lambda = \frac{2\pi}{\psi}. \tag{2.27}$$

The wave propagation speed is given by the permitivity and permeability of the medium

$$c = \sqrt{\frac{1}{\varepsilon\mu}} \tag{2.28}$$

For example, for free-space, $c = \sqrt{\dfrac{1}{8.854\times10^{-12} 4\pi \times 10^{-7}}} = 3\times10^8$.

2.2 Plane waves reflection from a media interface

Assuming that an incident plane wave has an electric field vector oriented along the x-axis and is propagating along the z direction towards a lossy medium, such as sand, with an incidence angle of zero with respect to the z-axis. At the point when the wave reaches the media interface (i.e. the transition point when the medium changes from free-space to sand), a portion of the incident field $\overline{E}_i$ is reflected as $\overline{E}_r$, and other portion of it is transmitted as $\overline{E}_t$. This can be visualized in Figure 2.1.

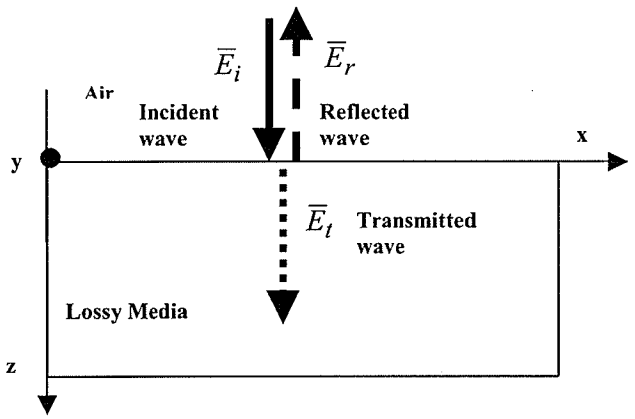

Figure 2.1 Incident wave being reflected by a medium interface.

The incident electrical field $\overline{E}_i$ can be expressed as

$$\overline{E}_i = \hat{x} E_o \, e^{-j\kappa_o z}, \tag{2.29}$$

and its related magnetic field as

$$\overline{H}_i = \hat{y} \frac{1}{\eta_o} E_o e^{-j\kappa_o z} \ . \tag{2.30}$$

Where E_o is the amplitude at which the electric field was emitted, η_o is the free-space wave impedance, $\hat{x}$ and $\hat{y}$ are unit vectors and κ_o is the wave number in free-space. $\overline{E}_r$ is located in the free-space region, but since it was reflected, it travels in the opposite way of $\overline{E}_i$. Hence, it is expressed as

$$\overline{E}_r = \hat{x} \Gamma E_o \, e^{+j\kappa_o z}, \tag{2.31}$$

and its related magnetic field as

$$\overline{H}_r = -\hat{y}\frac{\Gamma}{\eta_o}E_o e^{+j\kappa_o z} \quad . \tag{2.32}$$

Where Γ is the reflection coefficient of the electric field.

In the case of $\overline{E}_t$, it can be expressed as

$$\overline{E}_t = \hat{x}\mathrm{T}E_o\, e^{-\gamma z}, \tag{2.33}$$

and its related magnetic field as

$$\overline{H}_t = \hat{y}\frac{\mathrm{T}}{\eta_o}E_o e^{-\gamma z} \quad . \tag{2.34}$$

Note that γ has to be used because $\overline{E}_t$ is traveling in a lossy medium. T is the amplitude of the transmission coefficient.

For vertically incident waves, Γ and T are given by

$$\Gamma = \frac{\eta - \eta_o}{\eta + \eta_o}, \tag{2.35}$$

$$\mathrm{T} = \frac{2\eta}{\eta + \eta_o} \quad . \tag{2.36}$$

2.3 Conclusions

From this section the following points are observed:

1. –When the wave travels in a lossy medium such as sand, the propagation constant is complex. The imaginary part accounts for the loss. The wave is weighted by a decaying exponential. Hence it gets attenuated with the traveled distance.
2. –The wave propagation speed depends on the permitivity and permeability of the medium.
3. –The incident wave is reflected when there is a medium change. The reflected field is weighted by a reflection coefficient, which depends on the contrast of the wave impedance of the two media.

3. SFCW GPR Transceiver Analysis

The development of the imaging system presented in this thesis was originally targeted to complement an existing hardware transceiver previously developed by students of the University of Manitoba as a part of an undergraduate thesis [8]. The hardware is a stepped-frequency continuous wave ground penetrating radar (SFCW GPR) system, which was built with off-the-shelf parts. Figure 3.1 shows a picture of the actual hardware. The GPR supports a bandwidth of $\beta = 1$ GHz, and operates from an initial frequency $f_o = 1.13$ GHz to an end frequency $f_{end} = 2.13$ GHz, with a variable number of frequency steps from 2 to 512.

The theory of the operation of the SFCW GPR transceiver is presented in this section in order to understand how the RF signals are transmitted and received.

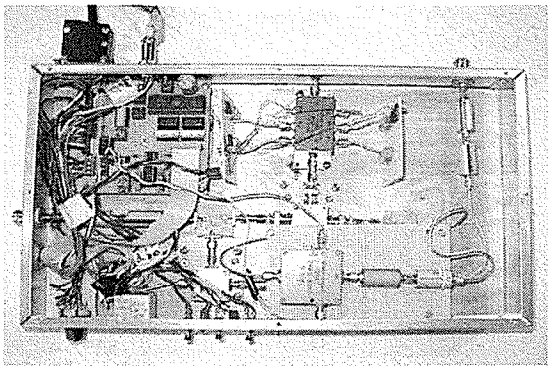

Figure 3.1 GPR hardware developed at the university of Manitoba.

3.1 The transmitter

A block diagram of the transmitter of the SFCW GPR is shown in Figure 3.2. In the diagram, *IF* is a reference oscillator fixed at 0.88 GHz, and *LO* is a local oscillator with a variable frequency ranging from 0.25 GHz to 1.25 GHz. The outputs of *IF* and *LO* are mixed and then band-pass filtered and amplified in order to be transmitted via a horn-type antenna.

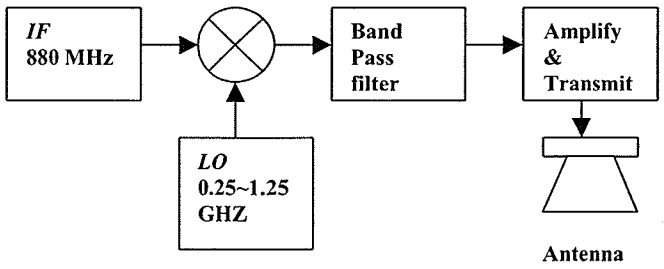

Figure 3.2 Block diagram of the transmitter.

Let the *IF* and *LO* signals be the cosine functions cos(*A*) and cos(*B*) respectively.

Where

$$A = 2\pi f_i t\,, \tag{3.1}$$

$$B = 2\pi f_l t\,. \tag{3.2}$$

Here, f_i is the fixed reference frequency and f_l is the *LO* frequency which is being varied linearly from 0.25 GHz up to 1.25 GHz.

The result of mixing *IF* with *LO* is

$$IF \times LO = \frac{1}{2}\left[\cos(A-B) + \cos(A+B)\right], \tag{3.3}$$

however, the term cos(*A*-*B*) yields frequency components ranging from –0.37 GHz to 0.63 GHz which are outside of the targeted operating range. Therefore a band-pass filter is applied to filter this term out, and at the output of the filter we have

$$S_t = \frac{1}{2}\cos(A+B)\,. \tag{3.4}$$

Note that the term cos(*A*+*B*) yields frequencies that are within the range of 1.13 GHz up to 2.13GHz, which is the targeted operating range for this specific GPR design.

By substituting (3.1) and (3.2) in (3.4), we have

$$S_t = \frac{1}{2}\cos\left(2\pi(f_i + f_l)t\right). \tag{3.5}$$

This signal is amplified and transmitted towards the targeted object for detection.

3.2 The receiver

At the receiver, the reflected signal is first filtered with a band-pass filter identical to the one used at the transmitter in order to pass only the frequencies which are within the targeted operating range. Then the filtered received signal is mixed with LO to perform demodulation and leave only the signal IF_r, which is a received version of IF that has a *modified* phase and amplitude. A block diagram of the receiver is shown in Figure 3.3.

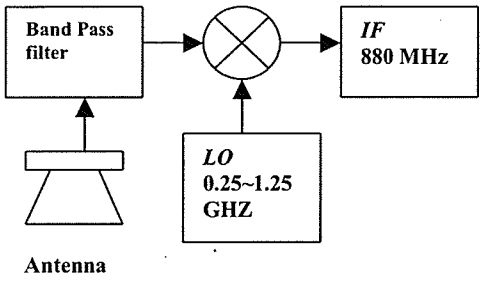

Figure 3.3 Block diagram of the receiver.

If we assume that there is a single reflecting point, then the received signal S_r is a version of the transmitted signal S_t, but with a different phase and amplitude caused by the traveled distance and the reflectivity of the object as explained in section 2. Then, from (3.4), we have

$$S_r = \frac{|\Gamma|}{2}\cos(A + B + \theta). \tag{3.6}$$

Where Γ represents the reflection coefficient of the object and θ represents the phase shift. Hence at the output of the mixer we have

$$S_r \times LO = \frac{|\Gamma|}{4}\left[\cos(A + \theta) + \cos(2B + A + \theta)\right] \tag{3.7}$$

Again, the term $\cos(2B + A + \theta)$ is eliminated as in the transmitter, and the remaining signal is

$$IF_r = \frac{|\Gamma|}{4}\cos(A + \theta), \tag{3.8}$$

and using (3.1)

$$IF_r = \frac{|\Gamma|}{4}\cos(2\pi f_i t + \theta). \tag{3.9}$$

In order to extract the reflecting object's information, the received IF_r is compared against the original reference IF. This process is key to detect differences in the amplitude and phase of the transmitted signal due to the reflector's material and distance. The comparison is performed by the use of a synchronous IQ demodulator. The inputs to the demodulator are the IF and IF_r signals and the outputs are two DC levels (I and Q) which are sampled and processed. Figure 3.4 shows the IQ demodulator block diagram.

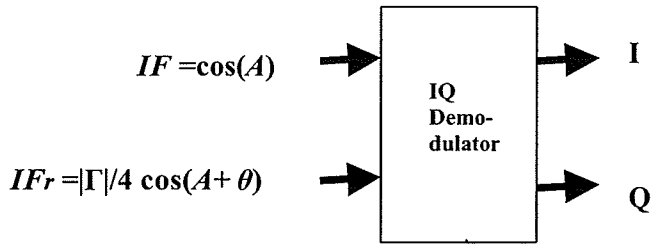

Fig. 3.4. The I and Q demodulator.

There are two mixers inside the demodulator. They both have the IF_r signal as input. The first mixer multiplies it by the IF signal $\cos(A)$, resulting in the inphase I output, and the second one multiplies it by a 90-degree shifted version of IF: $\cos(A+\pi/2)$, yielding the quadrature Q output. The inphase I output can be expressed as

$$I = \frac{|\Gamma|}{8}\left[\cos(A - A - \theta) + \cos(A + A + B)\right], \tag{3.10}$$

$$I = \frac{|\Gamma|}{8}\left[\cos(-\theta) + \cos(2A + B)\right], \tag{3.11}$$

and after low-pass filtering

$$I(\theta) = \frac{|\Gamma|}{8}\cos(-\theta). \tag{3.12}$$

In a similar way, the quadrature Q signal is obtained as

$$Q(\theta) = \frac{|\Gamma|}{8}\sin(-\theta). \tag{3.13}$$

The I and Q levels are the signals of interest in the system implemented in this research, since they contain important information, such as location and reflectivity of the objects, and they are easy to sample with an analog-to-digital converter.

3.3 Mapping phase shift to traveled distance

After the I and Q levels are sampled at the IQ demodulator, it is desirable to translate the phase shift θ into a physical measurable quantity such as distance.

As it was explained in section 2, a plane wave traveling in the z direction in a general lossy medium can be represented as

$$e^{-\phi z}\cos(\omega t - \psi z), \tag{3.14}$$

where ϕ and ψ correspond to the real and imaginary part of the complex propagation constant respectively, z is a unit vector, t is the time variable and $\omega = 2\pi f$ is the radian frequency.

The phase delay θ in the I and Q signals correspond to the phase shift in (3.14) as

$$\theta = \psi z, \tag{3.15}$$

and from (2.27)

$$\psi = \frac{2\pi}{\lambda} \tag{3.16}$$

where the wavelength is given by

$$\lambda = \frac{c}{f}. \tag{3.17}$$

The traveled distance z of a reflected signal is equal to two times the distance d_s between the transmitter antenna and the reflector, then by substituting (3.15), (3.16) and (3.17) in the I and Q expressions given in (3.12) and (3.13) we obtain

$$I = \frac{|\Gamma|}{8}\cos(-2\pi\frac{2ds}{c}f), \tag{3.18}$$

$$Q = \frac{|\Gamma|}{8}\sin(-2\pi\frac{2ds}{c}f). \tag{3.19}$$

From (3.18) and (3.19) it can be observed that I and Q are functions of three variables: the distance d_s, the traveling speed c which depends on the medium characteristics according to (2.28), and the transmitted frequency f, given by $f = fo + k\,\Delta f$, where f_o is the initial frequency, Δf is the frequency step, and k is an integer ranging from 0 to N, where N is the total number of transmitted frequencies. The amplitudes of I and Q are governed by the magnitude of the reflectivity Γ. The higher the magnitude of the reflectivity, the higher the amplitude of the I and Q signals.

In order to illustrate how the phase delay θ varies with the traveled distance, Figures 3.5 and 3.6 show a wave traveling two different distances respectively. In the first case, the traveled distance is exactly one cycle of the signal (i.e. one wavelength λ) and the reflecting object is located at position $d_s = 100$ units in the plot. Hence, the received reflected signal arrives in the receiver with zero phase shift, which would yield $\theta = 0$ in the I and Q signals. In the second case, the position of the reflector is shifted to $d_s = 105$ units, which causes the received reflected signal to arrive with a phase shift. Therefore, θ will be different than zero in the I and Q signals.

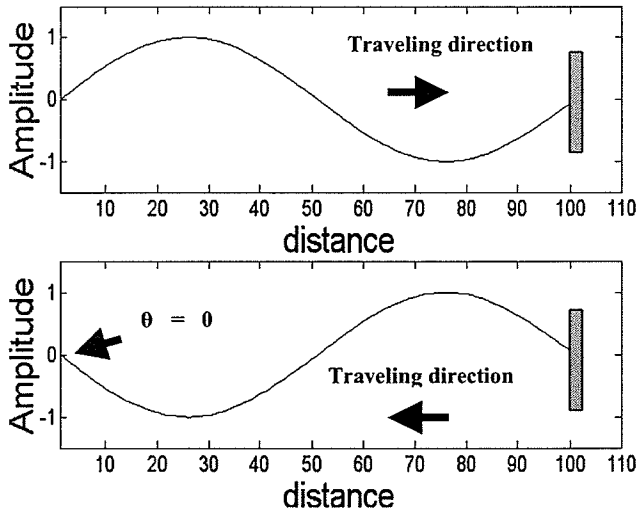

Figure 3.5 Wave traveling a distance equal to its wavelength.

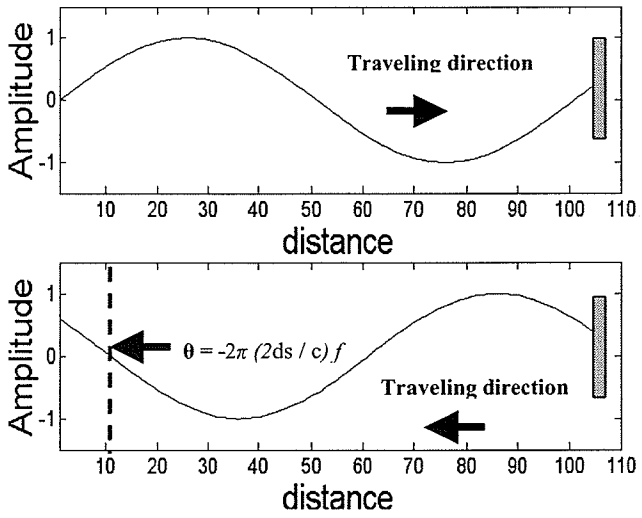

Figure 3.6 Wave traveling a distance different than its wavelength.

In reality, the received I and Q signals are the sum of many individual responses coming from different reflecting points located at different distances and angles with respect to the antenna. This can be expressed as

$$I = \sum_r \frac{\Gamma_r}{8} \cos(-2\pi \frac{2ds_r}{c} f), \tag{3.20}$$

$$Q = \sum_r \frac{\Gamma_r}{8} \sin(-2\pi \frac{2ds_r}{c} f), \tag{3.21}$$

however, for simplicity a single reflector was considered in the previous analysis.

3.4 Experiments

In order to confirm the theory explained above, it was decided to perform two simple experiments with the actual GPR system:

1. -Set a fixed frequency and vary the distance between an object and the antennas.

2. -Set a fixed distance and vary the frequency step by step.

The experiment was done in air, using a 15cm diameter aluminum disc as a reflecting object. An oscilloscope was connected to the I channel of the IQ demodulator at the GPR in order to collect the voltage readings. Figure 3.7 shows the set up of the experiment.

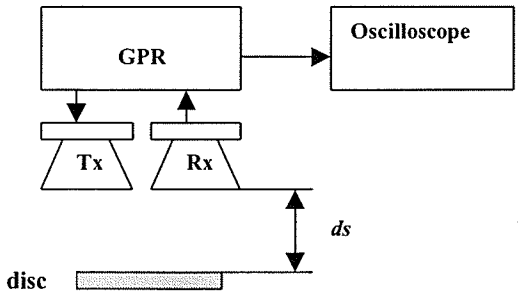

Figure 3.7 Set up used for the experiments with the I and Q signals.

In experiment 1, the object was moved to increase the distance d_s from 0cm up to 50cm with steps of 1cm. This was performed with a fixed transmitted signal frequency $f = 1.13$ GHz. Figure 3.8 shows the waveform of the I channel obtained by increasing the distance d_s.

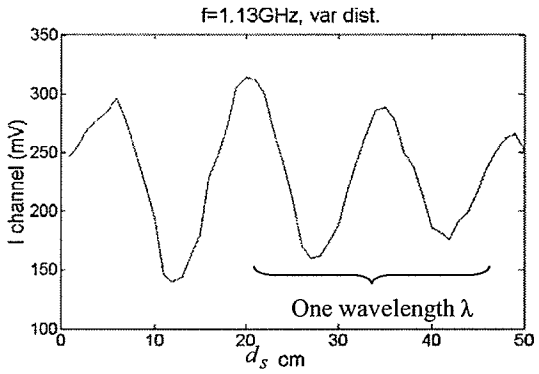

Figure 3.8 I channel waveform obtained by increasing the distance ds.

The wavelength of the transmitted signal is given by $\lambda = \frac{c}{f} = 26.55\,\text{cm}$, where $c = 3 \times 10^8$ is the propagation speed in free space, and $f = 1.13$ GHz. Hence if the distance d_s in (3.18) is increased by one wavelength λ, then the actual round trip traveled distance will be equal to two wavelengths. Therefore two cycles of the I channel waveform are drawn as shown in the plot from which it can be confirmed that when d_s is increased from 20cm to 46.55cm, approximately two cycles of the I waveform are drawn.

Notes:

1.- Although the *I* channel waveform plotted in Figure 3.8 appear to be a continuous function, it is actually a discrete function.

2.- The *I* channel waveform has a DC offset of approximately 225mV, which was set intentionally in order to match the input voltage range of the analog-to-digital converter of the GPR system.

In experiment No. 2, the object was set at a fixed distance $d_s = 20\,\text{cm}$, and the frequency f was varied from 1.13 GHz up to 2.13 GHz with 512 steps. In this case, the *I* channel was sampled with an analog-to-digital converter. Figure 3.9 shows the obtained waveform.

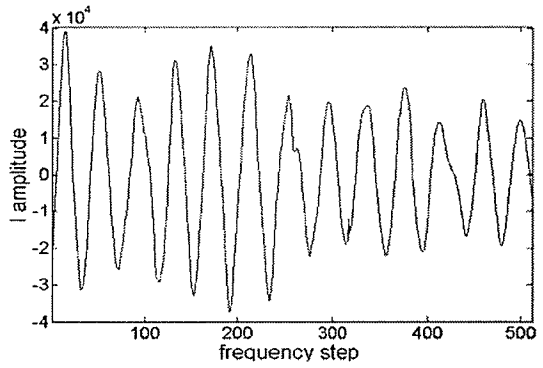

Figure 3.9 I channel waveform obtained with a fixed distance ds=20cm, and a variable frequency.

It is found that the frequency of the observed waveform changes with the length of the cables used. This is due to a phase shift experienced by the signal caused by the transmission line. In the case of Figure 3.9, the length of the cables was 1.5m. Figure 3.10 shows the waveform obtained using cables with a length of 9.3m.

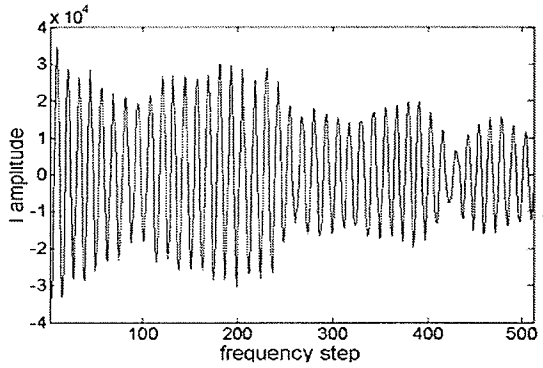

Figure 3.10 I channel waveform obtained with ds=20cm, variable frequency, and cables length of 9.3m.

Conclusions

From this section the following points are observed:

1. -The I and Q signals are functions of frequency, distance and propagation speed.

It is therefore possible to obtain information from reflected objects by changing either the separation distance d_s, the transmission frequency f, or even the propagation speed.

2. -The length of the antenna cables used causes the frequency of the I and Q waveforms to vary proportionally, because of the extra distance traveled. This will cause a peak shift in the range profiles, as will be explained in section 5. It is then important to take into consideration the cables length in the processing of the I and Q signals.

3. -The magnitude of I and Q is determined by the reflectivity of the object.

4. GPR Image Formation

This section explains how 2-dimensional focused images in synthetic aperture radar (SAR) airborne systems are formed in a line-by-line processor [11, 12]. This approach was followed in this work in order to be applied with a SFCW GPR. A signal burst (i.e. a set of continuous wave signals) with N frequencies is transmitted, received and stored at the current GPR location and the Inverse Fast Fourier Transform (IFFT) is applied to it in order to obtain a complex range profile as it will be explained in section 5.3. Then the GPR moves to the next position over the ground by advancing one cross-range step Δd_c and the process is repeated until a set of L complex range profiles is collected and a SAR complex data array with dimensions $N \, x \, L$ is stored, as shown in Figure 4.1.

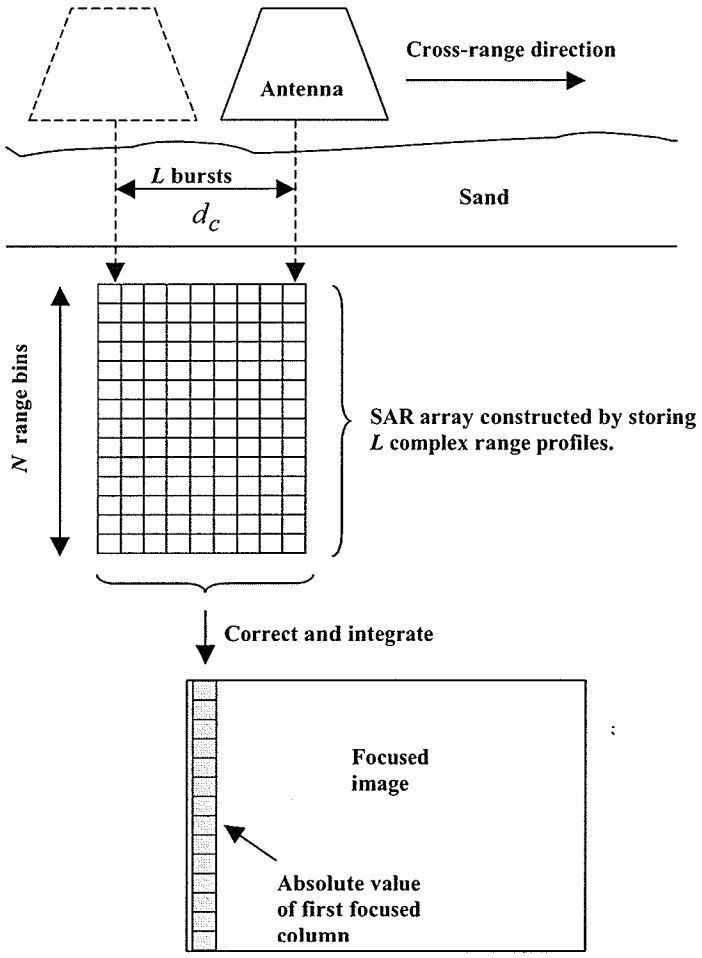

Figure 4.1 Focused SAR image being formed.

The set of L data vectors can be viewed as the equivalent of the received signal of a *single* antenna with a length $d_c = L \cdot \Delta d_c$. This process is known as *synthetic aperture radar*. The SAR response is the integration of the signal received from a point target at each of the L antenna positions.

4.1 Unfocused SAR array

If the absolute value of the SAR array were displayed at this point then a two-dimensional image of size N x L would be obtained, however such an image would be *unfocused*. This occurs due to the distance differences between the center of the synthetic antenna and the reflecting object at each cross-range location. Assuming that the reflecting target is a point located at a fixed position, then if a real antenna travels in the cross-range direction over such a point as shown in Figure 4.2, then as the antenna approaches the point, the distance $R+\delta R$ from the center of its aperture to the point decreases until it becomes the distance R, and after the antenna passes by the point, the distance increases again. At each antenna cross-range location the phase and the magnitude of the received signal varies according to the distance. Therefore the response of the point in the SAR array image, appears as an hyperbola having the maximum response when the distance is equal to R. An actual example of an unfocused image showing a hyperbolic response will be shown in Figure 5.13.

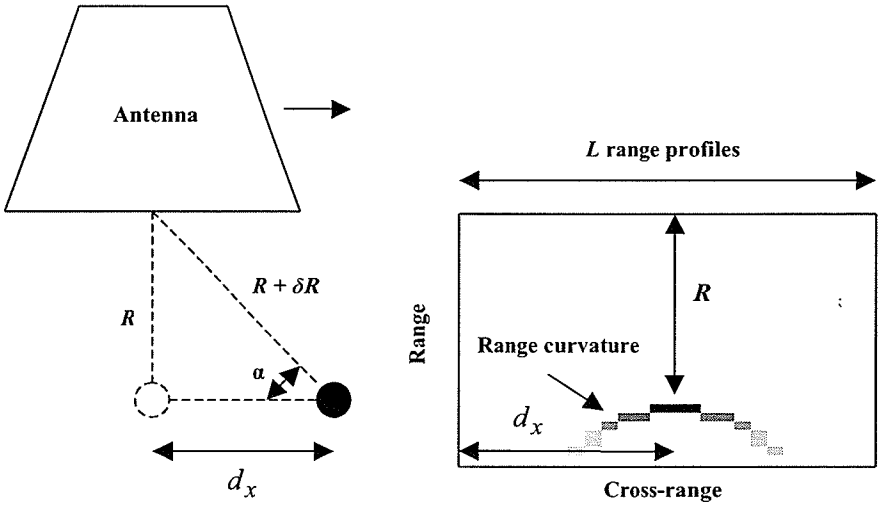

Figure 4.2 (left) GPR antenna moving in cross range direction over a target point. (right) Example of unfocused image obtained by displaying the absolute value of the SAR array, which shows range curvature.

4.2 Range curvature correction

By analyzing the dotted triangle in Figure 4.2, we have,

$$\delta R = \sqrt{R^2 + {d_x}^2} - R, \tag{4.1}$$

where δR is a quadratic distance that modifies the phase of the received signals according to the cross-range position d_x and a given range R. It causes a range migration $M^{'}$ to occur

$$M^{'} = \frac{\delta R}{\Delta r_s}, \tag{4.2}$$

Where, Δr_s is the range resolution as will be defined in (4.5).

In order to correct the range curvature in the SAR array, δR is estimated for each response cell in the array with respect to the center of the synthetic antenna. The value of d_x for each array cell can be obtained by knowing L and d_c, and R is set to a desired focusing center range. In this work, a complex correction matrix of size $N \times L$ is prepared which contains L complex exponential columns as

$$E_{sar\,k,l} = e^{-j2\pi \frac{2\delta R_{k,l}}{c} f} \tag{4.3}$$

Where k and l are rows and columns indexes respectively, f is the transmitted frequency, and c is the propagation speed which depends on the characteristics of the medium. This exponential is point by point multiplied with the SAR array in the frequency domain as will be explained in section 5.5 in order to produce a phase shift in each of the L range profiles so the responses become aligned as shown in Figure 4.3.

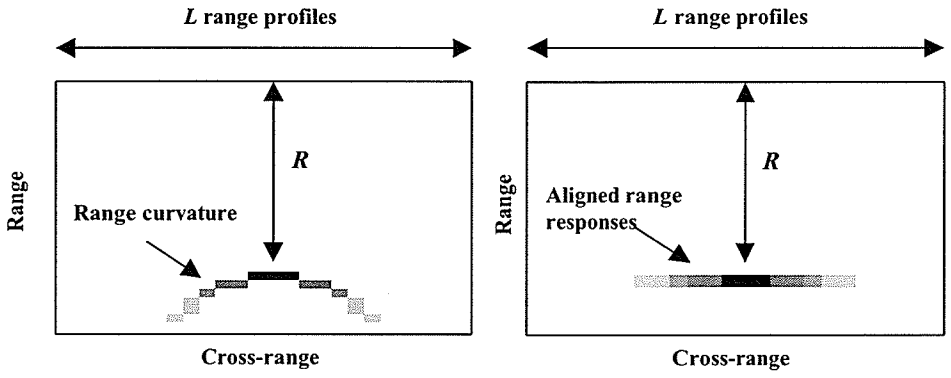

Figure 4.3 SAR array before and after phase correction.

Once the responses are aligned in range, the total response at the synthetic antenna can be obtained by performing integration of the SAR array. This is performed by summing all of the complex range columns horizontally, hence producing a single focused complex range column. The absolute value of this column is appended into the final image matrix in order to be displayed. The next column of the final image is generated by moving the GPR by one cross-range step Δd_c, hence appending a new complex range profile column into the SAR array and eliminating the oldest complex range profile column in the array, and by repeating the curvature correction and integration processes. Note that the size of the SAR array is kept constant as the GPR moves to the next location. This focusing process is known as *azimuth compression* and more details can be found at [11 (sections 6.3, 6.4, 6.7, 6.8)], and [12 (chapter 31)]. Figure 4.4 shows a block diagram of the process.

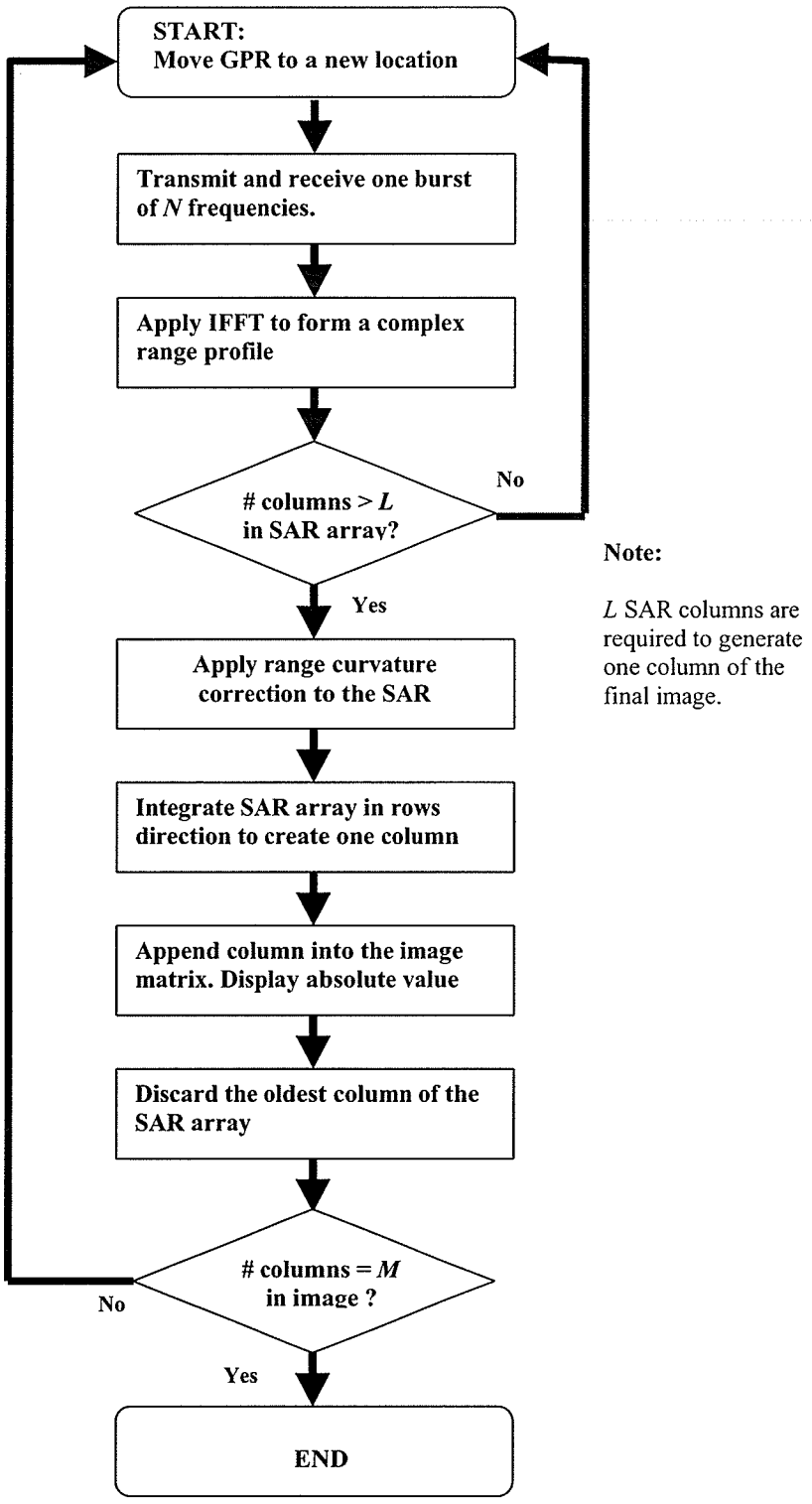

Figure 4.4 SAR processing flowchart.

4.3 Radar imaging parameters

The geometry of the imaging problem studied in this work is depicted in Figure 4.5. Based on this geometry, the GPR system parameters are defined appropriately in order to generate images of the targeted object, which is the plastic landmine shown in Figure 6.4.

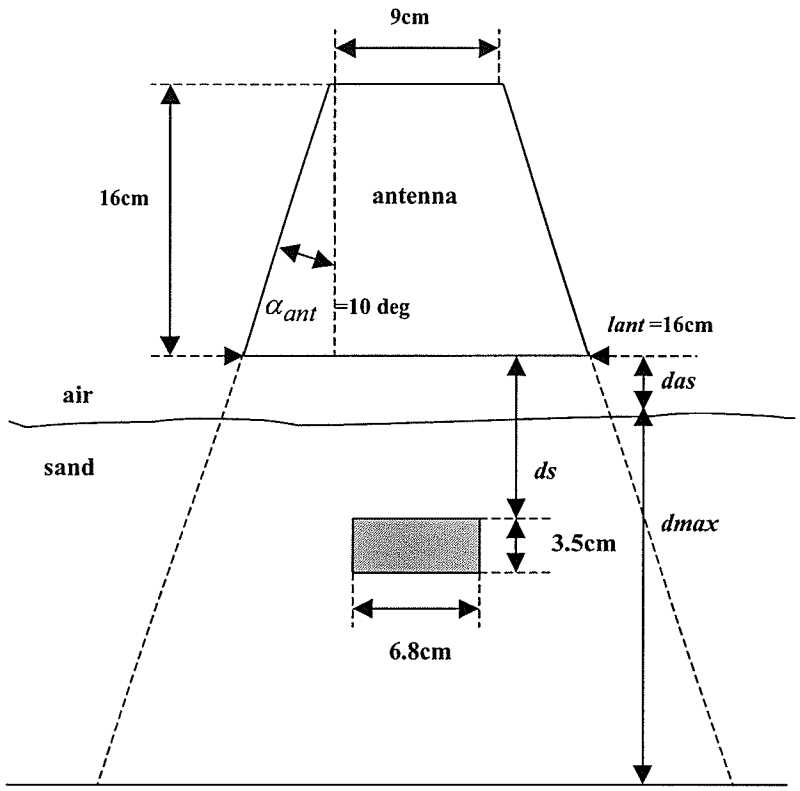

Figure 4.5 Geometry of the problem under consideration.

Resolution cell

According to [11 (pg. 394)], the required size of one resolution cell in a high-resolution radar image, should be from 1/5 to 1/20 of the major dimension of the smallest object to be recognized, as shown in Figure 4.6. Hence, for the plastic mine under consideration, the smallest dimension is 3.5cm, which is its height. Therefore, the desired size of one resolution cell would be 7 mm x 7 mm.

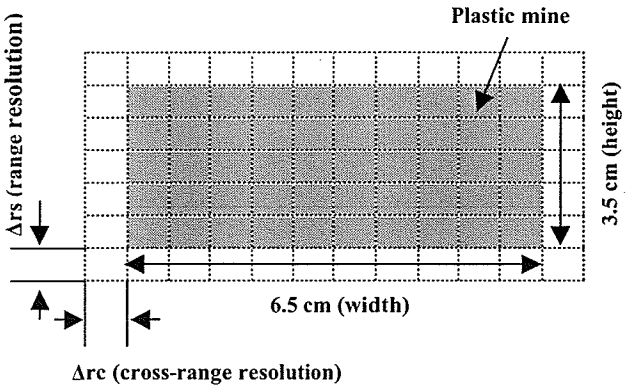

Figure 4.6 Plastic mine resolution cells.

4.4 Range resolution

From [12 (page 95)], in a stepped-frequency radar system, the desired maximum unambiguous range $d_{\max}$ to be mapped, determines the maximum frequency step Δf to be used according to the Nyquist criteria

$$\Delta f = \frac{c_{sand}}{2 \cdot d_{\max}}, \tag{4.4}$$

where c_{sand} is the propagation speed of the microwaves in sand.

If $d_{\max}$ is set to 20cm, and $c_{sand} = 1.8245 \times 10^8$ m/sec, then the maximum frequency step to be used is $\Delta f = 456.125$ MHz.

The range resolution is given by

$$\Delta r_s = \frac{c_{sand}}{2 \cdot N \cdot \Delta f}, \tag{4.5}$$

where N is the number of transmitted frequency steps in one burst. Hence, in order to achieve the desired range resolution cell of $\Delta r_s = 7$ mm, N would have to be set to 28, yielding a required system bandwith $\beta = 13.03$ GHz. Where $\beta = N \cdot \Delta f$.

4.5 Cross-range resolution

From [12 (eq. 6.14)], the cross-range resolution of the real aperture is given by

$$\Delta r_c = 0.64 \cdot R \frac{\lambda_c}{l_{ant}}, \tag{4.6}$$

where λ_c is the wavelength of the center frequency in the burst, l_{ant} is the length of the real antenna, and R is a given range.

Hence, for λ_c = 2.68cm, l_{ant} = 16cm, and R = 6cm, the resolution would be Δr_c = 6.4cm.

Figure 4.7 shows the actual cross-range resolution obtained by moving the real antenna shown in Figure 6.2 in front of a 12mm-diameter metal rod located at R = 6cm from the antenna in the same way as shown in Figure 4.2. By finding the half power points in cross range of the power of the response shown in Figure 4.7, the resolution is found to be approx. Δr_c = 7cm, which is close to the theoretical 6.4cm. As can it can be noticed the 7cm cross-range resolution of the real antenna beam is rather far from the desired 7mm resolution cell. Therefore, SAR processing is required in order to improve the cross-range resolution as explained next.

From [12 (eq. 6.40)], the cross-range resolution when the SAR array is focused is given by

$$\Delta r_c = \frac{\lambda_c \cdot R}{2 \cdot d_c}, \tag{4.7}$$

where d_c is the length of the synthetic array. Note that the resolution has a dependency on the range R. Hence the SAR array length can be chosen in order to achieve a required cross-range resolution obtained at a given range R. For example, for the same metal rod at R = 6cm, if the length of the synthetic aperture is defined to be d_c = 20cm, then the cross-range resolution becomes Δr_c = 4mm. And for the ranges 5, 10 and 20cm, the corresponding resolutions are 3.35mm, 6.7mm and 1.34 cm, which satisfy the required resolution cell size, assuming that the landmine will be buried at depths from 2 to 10cm.

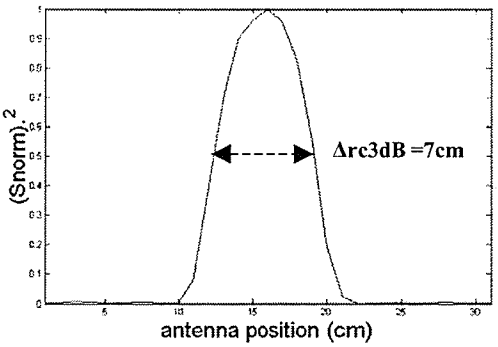

Figure 4.7 Squared normalized cross-range response of a metal row showing the actual cross-range resolution of the real antenna beam.

5. Digital Signal Processing Algorithm

The objective of this work is to develop a computer imaging system that uses a SFCW GPR hardware to transmit and receive microwave signals and that processes the data in order to generate 2-dimensional images which contain the responses of objects buried in sand. The targeted object to be imaged is the plastic landmine shown in Figure 6.4. Although the airborne SAR image formation algorithm explained in section 4 is used in this work in order to generate images, it is not enough for this GPR application in which the following problems have to be addressed:

1. –The reflections from the surface of the sand are significantly stronger that those from the buried objects.
2. -The dielectric constants of the sand and plastic are close to each other, which causes the reflection coefficient to be small, hence producing a weak response which is obscured by the responses of the surface and other objects.
3. -It is required to generate the GPR images in real-time.

This section explains an algorithm that was developed as a part of this thesis in order to generate real-time GPR images by considering the problems cited above. The proposed algorithm is divided into three processing stages: range processing, SAR processing and cross-range processing. Each incoming data vector obtained at each antenna cross-range position is processed as soon as it becomes available in the memory of the computer system. A flow diagram of the algorithm is shown in Figure 5.1, then each process is explained in detail in the next pages. The algorithm was developed and tested with actual data from GPR measurements and it assumes that the following conditions are met:

1. -A GPR system with a bandwidth of at least 12 GHz is available in order to achieve a resolution cell of approximately 8mm.
2. -The landmine is buried in homogeneous dry sand.
3. -A single plastic landmine is buried.
4. -The geometrical characteristics and reflectivity of the landmine are known.
5. -The landmine is buried at depths from 2cm to 10cm.
6. -The GPR moves in discrete steps, and a complete burst is transmitted and sampled at each step.

Algorithm Flow Diagram

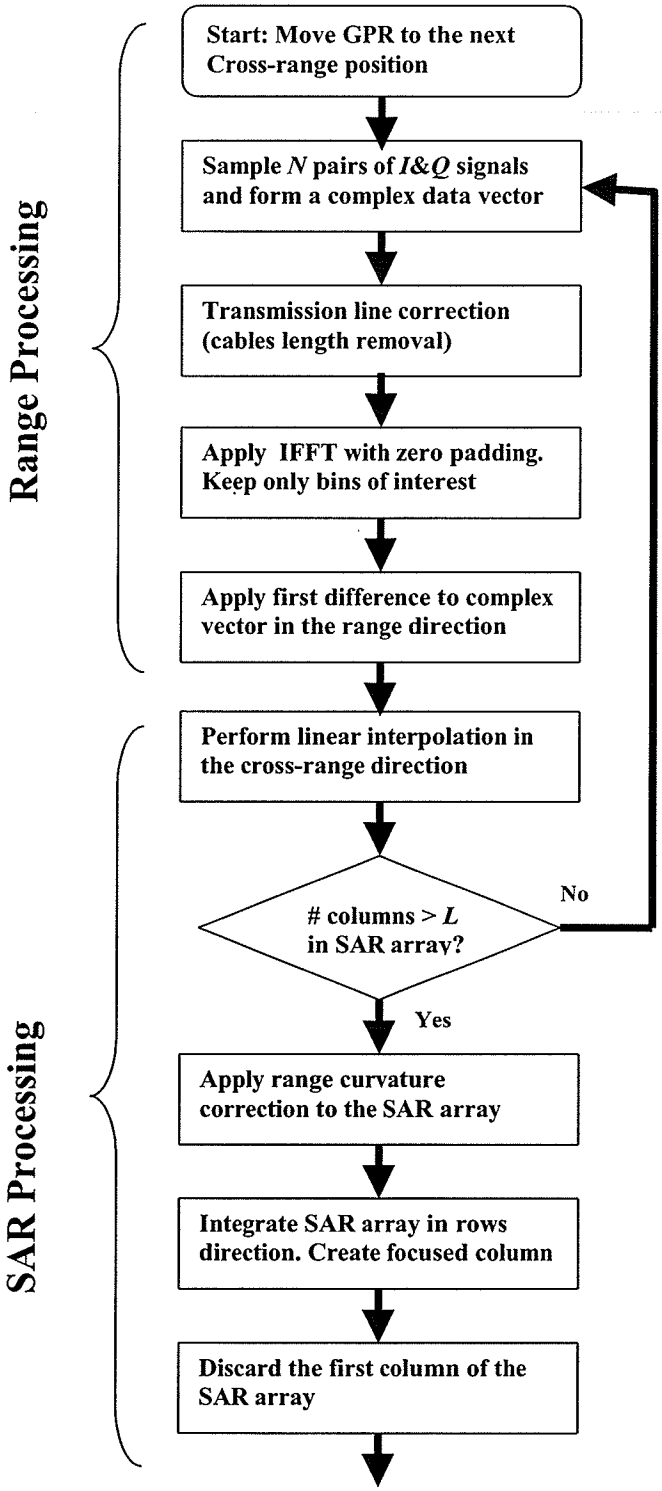

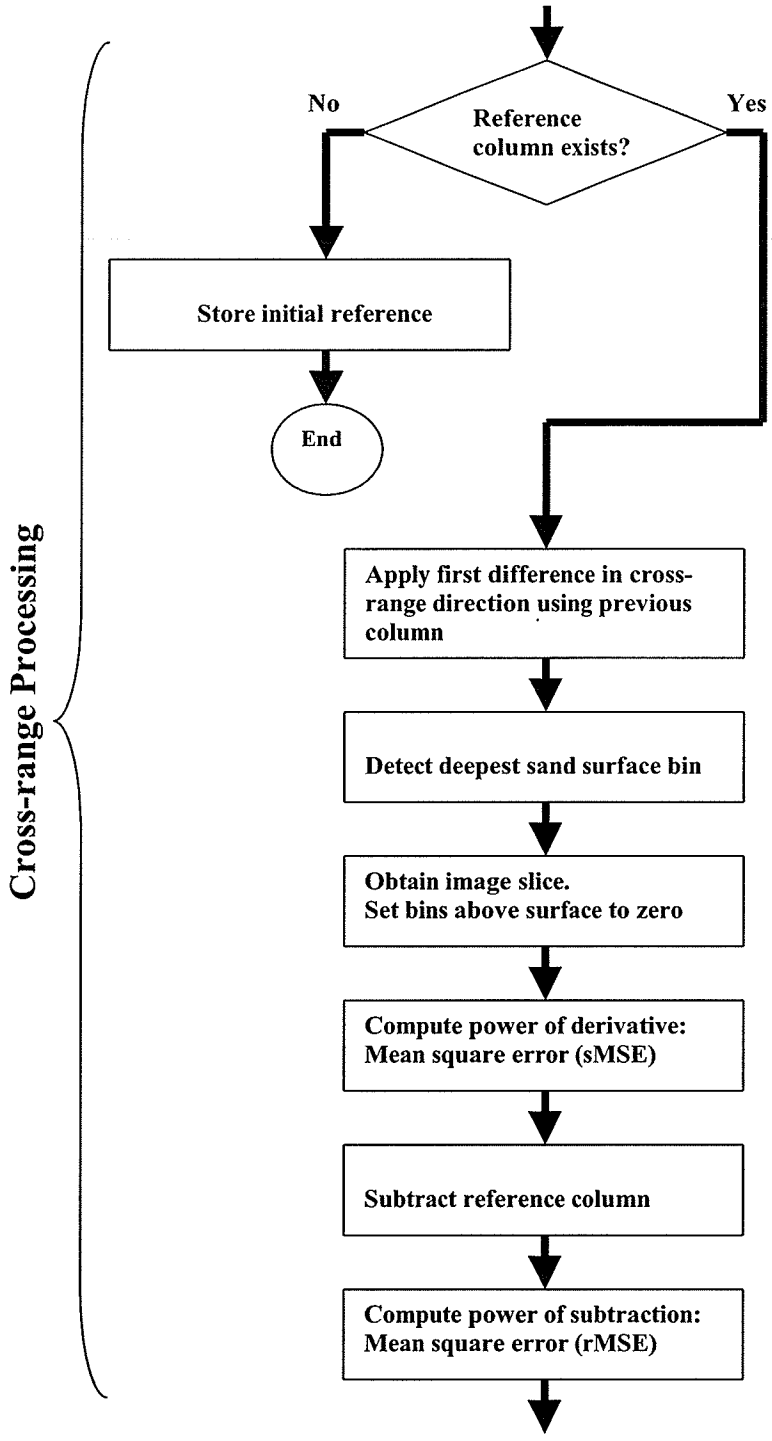
Cross-range Processing
No
Reference column exists?
Yes
Store initial reference
End
Apply first difference in cross-range direction using previous column
Detect deepest sand surface bin
Obtain image slice.
Set bins above surface to zero
Compute power of derivative: Mean square error (sMSE)
Subtract reference column
Compute power of subtraction: Mean square error (rMSE)

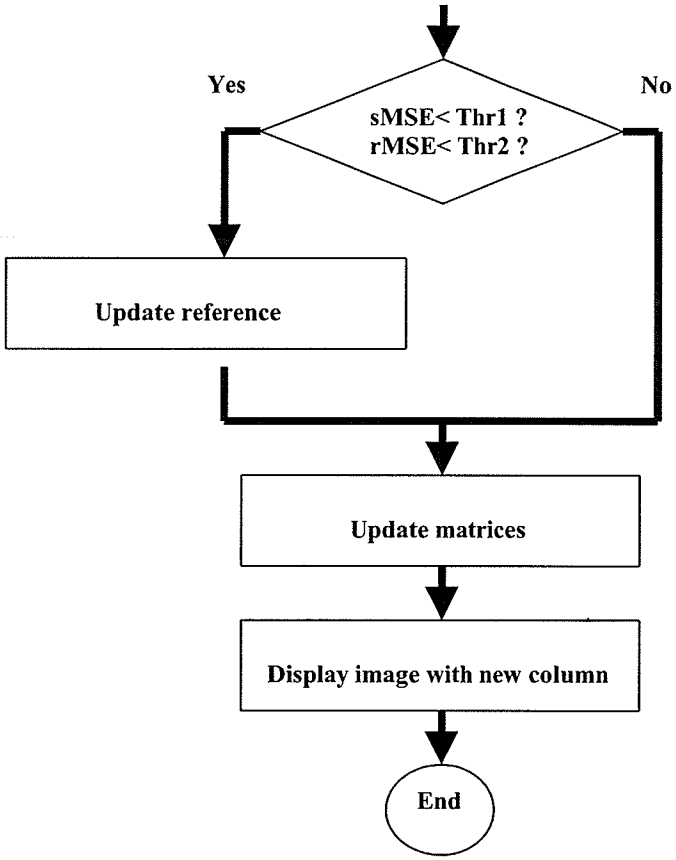

Figure 5.1 Flow diagram of the algorithm presented in this work.

5.1 *I* & *Q* signals sampling

The expressions for the I and Q signals with a single reflecting object and with a constant propagation speed c were given in section 3 as

$$I(d,f) = \frac{|\Gamma|}{8}\cos(-2\pi\frac{d}{c}f) \tag{5.1}$$

$$Q(d,f) = \frac{|\Gamma|}{8}\sin(-2\pi\frac{d}{c}f) \tag{5.2}$$

In SFCW, N microwave pulses are transmitted stepped in frequency by Δf from pulse to pulse over a defined bandwidth. After the *kth* pulse was reflected by the farthest object, and arrived in the receiver, the argument in the I and Q functions will remain constant. Consecutively each I and Q analog voltage at the GPR will be in steady-state. This is graphically illustrated in Figure 5.2.

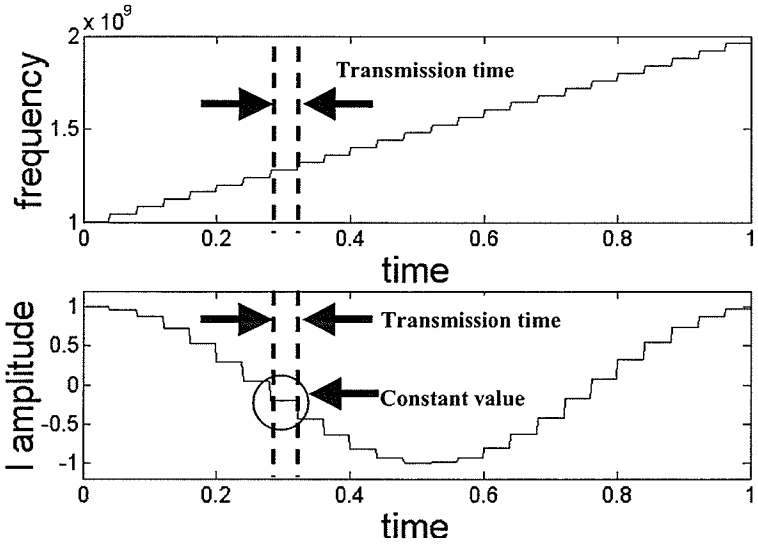

Figure 5.2 (Top) Frequency step ramp function, (Bottom) *I* channel waveform.

The analog-to-digital converter is synchronized with the stepped ramp in order to acquire the I and Q samples at the time when a stable level has been reached, which occurs after the signal reflected by the farthest object has arrived in the receiver. Enough time must be given to the hardware to stabilize after tuning it to a new frequency. Note that the sampling is actually performed in the frequency domain, and the Nyquist criteria is followed by properly selecting the frequency step Δf by using (4.4). Hence, by collecting the I and Q samples for each transmitted frequency, an approximation of the frequency response of the measured medium is obtained for that bandwidth. When the GPR system shown in Figure 3.1 is used, mean removal is applied immediately after sampling in order to eliminate the bias added by an operational amplifier used to adapt the I and Q levels to the available A/D converter input range. Once N samples of the I and Q signals are available, a complex data vector S is made as

$$S = I + jQ\,. \tag{5.3}$$

From (5.1) and (5.2),

$$S(d,f) = A \cdot e^{-j2\pi\frac{d}{c}f}, \tag{5.4}$$

where $A = |\Gamma|/8$ is the magnitude of the phasor, which is proportional to the object reflection coefficient, and d is the total distance traveled by the microwave signal.

5.2 Transmission line correction (cable length removal)

As mentioned in section 3, the signal traveled distance d includes the length of the GPR system cables. Therefore the distance d is expressed as

$$d = d_{syst} + 2d_s, \tag{5.5}$$

where d_{syst} is the traveled distance which includes the GPR internal and external cables and the antenna length, and d_s is the separation distance between the end of the antenna and the reflecting object (i.e. the surface of the sand). Note that a factor of 2 is included which accounts for the round trip.

Then, by substituting (5.5) in (5.4),

$$S(d_s, f) = A \cdot E_s \cdot e^{-j2\pi \frac{2d_s}{c} f}, \tag{5.6}$$

where

$$E_s = e^{-j2\pi \frac{d_{syst}}{c} f} \tag{5.7}$$

is the term that causes a phase shift in the S signal.

Hence, an exponential signal vector E is generated and stored which is equal to E_s but with opposite sign in its phase

$$E = e^{+j2\pi \frac{d_{syst}}{c} f}, \tag{5.8}$$

which is multiplied point-by-point with (5.6) in order to obtain a corrected signal S_{corr} as

$$S_{corr} = S \cdot E, \tag{5.9}$$

i.e.

$$S_{corr}(d_s, f) = A \cdot e^{-j2\pi \frac{2d_s}{c} f}. \tag{5.10}$$

By multiplying the signal by the correction exponential in the frequency domain, a time (range) shifting will be produced when the Inverse Fourier Transform is applied to the signal as explained in the next section. This is equivalent of applying the time shifting property of the Fourier Transform. Figure 5.3 shows the range profiles (absolute value of the IFFT of the data) of a sampled signal S and the corrected signal S_{corr}.

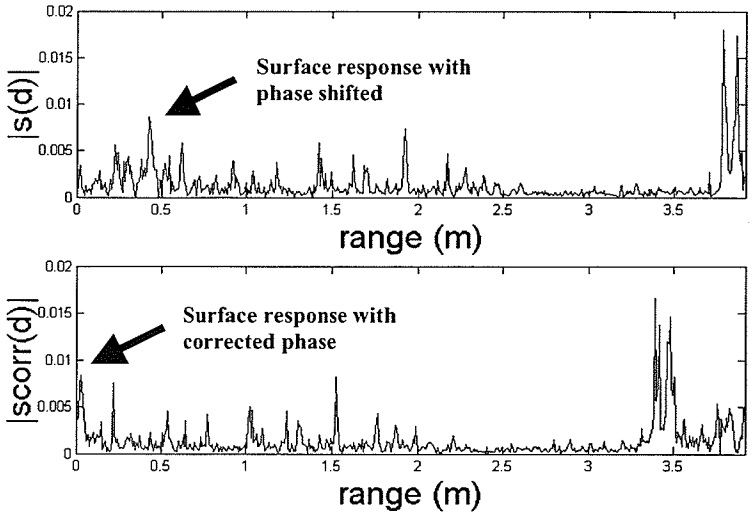

Figure 5.3 (Top) Sampled signal range profile, (Bottom) Corrected signal range profile.

The plots were generated with a plastic landmine buried 5cm in sand. Once the phase correction is made, all the responses are translated to their proper range positions, as can be observed with the response of the sand surface, which is close to the zero bin corresponding to the antenna location. The response of the landmine is not visible, because it is obscured by the other stronger peaks which correspond to reflections of objects at deeper locations (i.e. the scan was performed at the fifth floor of a building).

The propagation speed used in (5.10) was $c = 1.82 \times 10^8$ m/s, which is an approximation of the speed in the sand. The distance d_{syst} was obtained by physically measuring and summing all of the system-related distances traveled by the signals as follows:

cable length $= 2 \times 10.8$ m.

antenna length $= 2 \times 0.12$ m.

other system delays $= 5.78$ m (system internal wiring, other).

d_{syst} = *cable length* + *antenna length* + *other system delays.*

$d_{syst} = 27.62$ m.

Note: There are calibration procedures for network analyzers in order to apply corrections to the data. However, the phase correction process was included in this work in order to be used with the GPR hardware shown in section 3, which does not have a calibration option.

5.3 IFFT and removal of unwanted range responses

In order to obtain the responses of the objects located at different ranges (distances), the Inverse Fourier Transform is applied to the phase-corrected complex data vector S_{corr}, which is a function of frequency. Therefore, both the obtained complex range profile s_{corr}, and the frequency domain data S_{corr}, will be assumed to be periodic, which is not true in reality. The corrected vector S_{corr} can be represented as

$$S_{corr\,k} = A_k \cdot e^{-j2\pi\frac{2d_s}{c}fo} \cdot e^{-j2\pi\frac{2d_s}{c}\Delta f \cdot k}, \tag{5.11}$$

where $f = f_o + k \cdot \Delta f$, f_o is the initial frequency, Δf is the frequency step, and $0 \le k < N$.

The inverse Fourier Transform is applied to (5.11) as

$$s_{corr\,n} = A_k \cdot e^{-j2\pi\frac{2d_s}{c}fo} \cdot \sum_{k=0}^{N-1} e^{-j2\pi\frac{2d_s}{c}\Delta f \cdot k} \cdot e^{+j2\pi\frac{k \cdot n}{N}}, \tag{5.12}$$

if A_k is assummed to be 1,

$$s_{corr\,n} = e^{-j2\pi\frac{2d_s}{c}fo} \cdot \sum_{k=0}^{N-1} e^{j2\pi\frac{k}{N}\left(n - N\cdot\frac{2d_s}{c}\Delta f\right)}, \tag{5.13}$$

and by using the identity

$$\sum_{p=0}^{b-1} e^{ja \cdot p} = \frac{\sin\frac{ab}{2}}{\sin\frac{a}{2}} \cdot e^{j\frac{(b-1)a}{2}}, \tag{5.14}$$

which for $p = k$, $b = N$, $a = 2\pi\frac{y}{N}$, $y = \left(n - N \cdot \frac{2d_s}{c}\Delta f\right)$ yields,

$$s_{corr\,n} = e^{-j2\pi\frac{2d_s}{c}fo} \cdot \frac{\sin\pi y}{\sin\frac{\pi y}{N}} \cdot e^{j\frac{(N-1)\pi y}{N}}. \tag{5.15}$$

Hence, the obtained vector s_{corr} is a function of the distance d_s, and the response of a reflecting object will have a sinc shape. A range profile is obtained by taking the absolute

value of s_{corr}. In this work, the IFFT is applied with zero-padding of up to 3 times the length N of the data in order to have a better display of the obtained image in the later steps. Because the depth of the sand box used in this work is 30cm, and land mines are usually buried from 2 to 10cm, a depth of interest d_{int} is defined as the maximum imaging depth that will be observed, and it is set to $d_{\text{int}} = 20\,\text{cm}$. From the plots in Figure 5.4, it can be observed that the range profile s_{corr} is dominated by strong responses located at the center and the right side of the profile. Theoretically, these are responses of reflecting objects that are located beyond the range of interest of 20cm. Since these peaks obscure the weak reflections contained in the range of interest d_{int}, they are simply discarded. The vector containing the remaining range bins of interest is named s_{cf}.

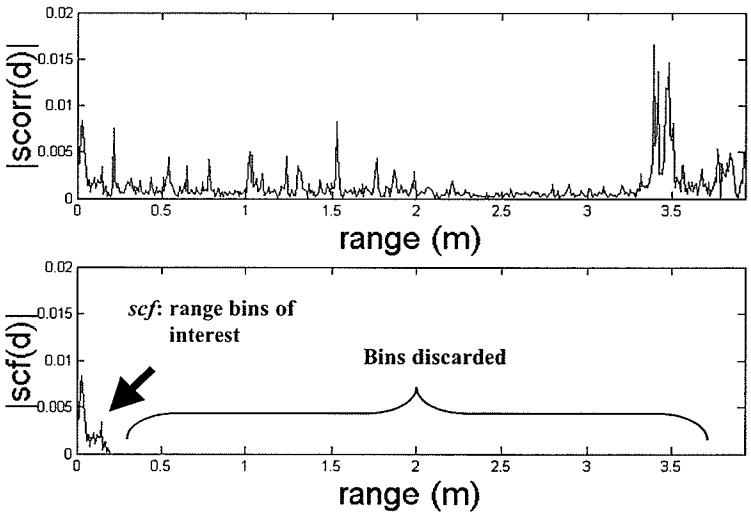

Figure 5.4 Range profile bins of interest.

5.4 First difference in range direction

Once a range complex profile s_{cf} is available that contains the responses of the reflecting objects located within the range of interest, the first difference is applied in the range domain. As in [10], the purpose is to detect transitions in the responses in order to emphasize the presence of the weak reflections from the plastic landmine. The first difference is applied as follows:

$$s_{der_n} = s_{cf_n} - s_{df_{n-1}}. \tag{5.16}$$

Figure 5.5 shows the result of applying the first difference to one complex range profile of a plastic landmine buried 5cm in sand.

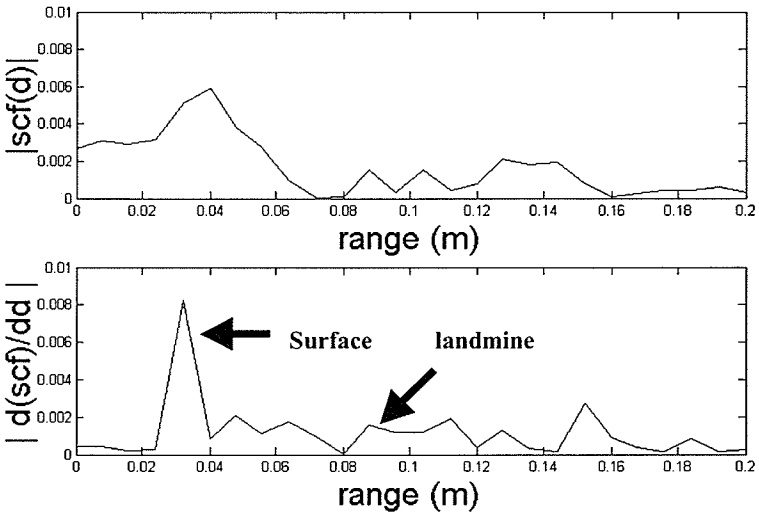

Figure 5.5 ***scf*** **range profile (top),** ***sder*** **range profile (bottom).**

5.5 Synthetic aperture array processing (SAR)

As soon as a complex profile s_{der_n} is available, it is appended as a column in the 2-dimensional SAR array $sar_{n,l}$ as explained in section 4. The subscripts k and l denote the range and cross-range indexes. In order to improve the final image when it is displayed, linear interpolation is performed between s_{der_n} and the latest complex profile stored in the SAR array, hence actually two columns are appended into the SAR array. The cross-range length of the array is chosen to be d_c = 20cm in order to achieve cross-range resolution of about 8mm as explained in section 4.

SAR range curvature correction

As explained in section 4, the quadratic distance δR from the top center cell in the SAR array to each of the other cells that causes the range curvature (hyperbolic response) is

pre-computed using (4.1). In this work the desired focusing center range R is set to 5cm which is one half of the maximum distance at which it is assumed that landmines are buried. Each δR is used to construct a two-dimensional correction exponential matrix as

$$E_{sar\,k,l} = e^{-j2\pi \frac{2\delta R_{k,l}}{c} f}. \tag{5.17}$$

Where k and l are rows and columns indexes respectively, and c is the propagation speed which depends on the characteristics of the medium. This exponential is point-by-point multiplied by the SAR array in the frequency domain as

$$SAR_{k,l} = E_{sar\,k,l} \cdot \Im\{sar_{n,l}\}. \tag{5.18}$$

Where $\Im\{\ \}$ denotes the Fourier Transform. Then, $SAR_{k,l}$ is transformed back hence producing the corrected array $sar_{f\,n,l}$. After the phase correction is done, the range responses from each reflecting cell are properly aligned as was explained in section 4.

SAR integration

As mentioned in section 3, the received signal is the sum of the reflections from all the objects illuminated by the antenna beam. Because in the corrected array $sar_{f\,n,l}$ the range responses from each reflecting cell are aligned, the columns in the array are summed horizontally in order to synthesize a single complex range profile $s_{cmp\,n}$

$$s_{cmp\,n,m} = \sum_{l=-\frac{L}{2}}^{\frac{L}{2}} sar_{f\,n,l}, \tag{5.19}$$

where, L is the number of columns in the SAR array, and the subscript m denotes the column number in the final image F. At this point, the first column of the $sar_{n,l}$ array is discarded. Because at the next antenna position a new column will be appended, the dimensions of the array are kept constant.

5.6 Adaptive Reference Subtraction

As seen in section 2, a reflected component of an incident wave will be reflected every time an interface is found (i.e. transition from sand to plastic). Hence, as the GPR moves in the cross-range direction, the goal is to detect these interfaces, or in other words, to detect differences in the characteristics of the medium, such as permitivity. The focus of this work is to enhance those differences in order to emphasize the response of weak reflectors such as a plastic landmine as the GPR moves to the next position. In order to achieve this objective, a subtraction approach is followed. It is applied as soon as a data vector $s_{cmp_{n,m}}$ is available instead of waiting until a two-dimensional data matrix is constructed.

As in (5.17), the first difference is applied to the incoming data vector $s_{cmp_{n,m}}$ in order to attempt to detect transitions in the cross-range direction within the depth of interest. It is applied as

$$s_{cder_{n,m}} = s_{cmp_{n,m}} - s_{cmp_{n,m-1}}. \tag{5.20}$$

In order to illustrate the purpose of this process, Figure 5.6 shows a two-dimensional image in which the absolute value of $s_{cder_{n,m}}$ is displayed. The image contains the response of a plastic landmine buried in sand. In this example, the range of interest d_{int} is 20cm, the cross-range step Δd_c is 1cm, L is 20cm and the GPR traveled distance is 1m. Figure 5.7 shows the absolute value of $s_{cmp_{n,m}}$, in which the first difference was not applied. By comparing these two images it is evident that the first difference works effectively in enhancing the weak responses of the plastic mine.

It can be observed in Figure 5.6 that the response from the sand surface is removed. This occurred in this specific example because the surface of the sand was flat and the difference between adjacent surface bins was close to zero. However, a drawback of applying the first difference is found when the surface of the sand is rough, since this causes the result of the differences to have a high values which obscure the weak responses of the plastic mine, as shown in Figure 5.8.

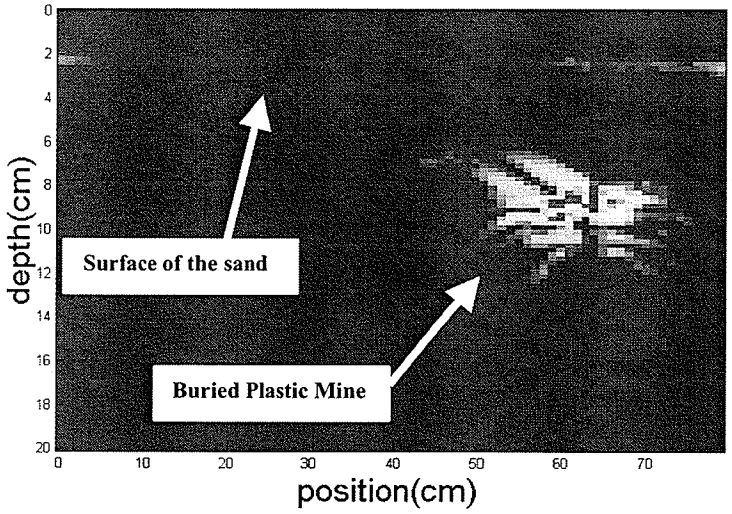

Figure 5.6 Image of the absolute value of $s_{cder_{n,m}}$. The reflections of a plastic mine buried in sand are noticeable.

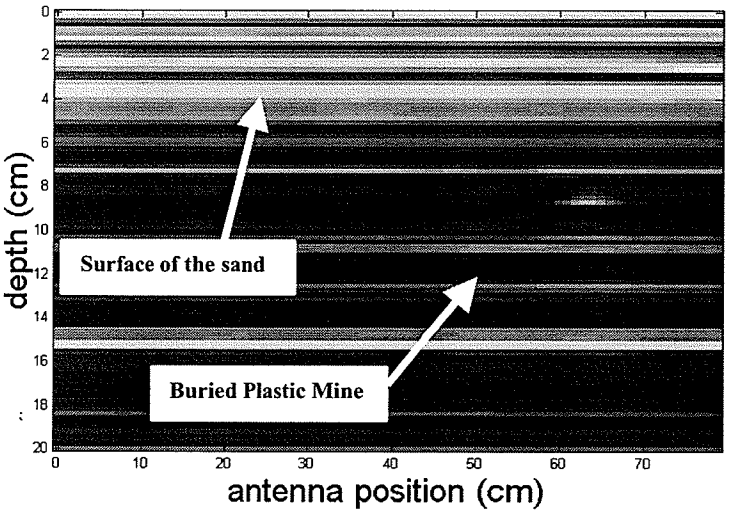

Figure 5.7 Absolute value of $s_{cmp_{n,m}}$ in which no derivative is applied.

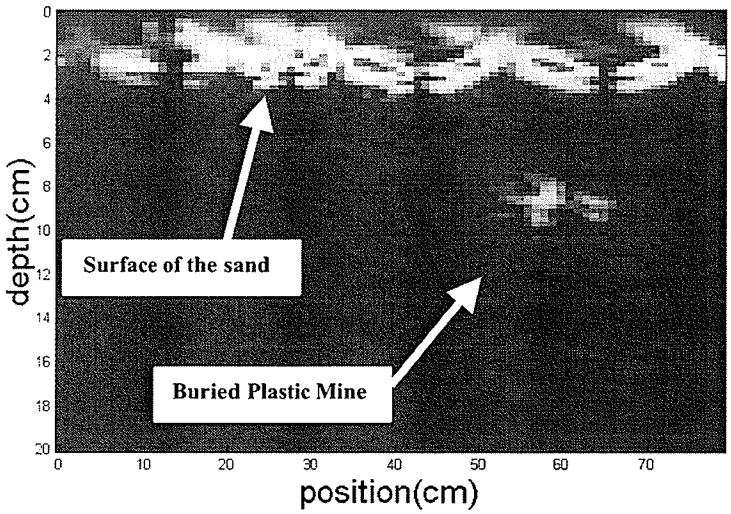

Figure 5.8 Absolute value of $s_{cder_{n,m}}$ with a rough sand surface.

Sand surface removal

In order to overcome the problem of the use of the first difference with a rough surface, an early range window [3] can be used to remove the strong surface reflections. This would be effective if the rough surface of the sand never crosses the boundary of the window, which is not likely to happen all the time. In this work, an adaptive time window is applied, in which the surface bin is *tracked* at each GPR cross-range position. The location of the surface is estimated by specifying a fixed distance d_z, measured downwards from the antenna as shown in Figure 5.9. For each incoming complex column $s_{cder_{n,m}}$, the first range bins contained in the distance d_z are examined in order to find the bin with the maximum value *sbin,* which is assumed to contain the maximum response of the sand surface. Once *sbin* is obtained, it is set to zero together with all the bins above it, and a set of neighbor range bins below it which obscure the response of the buried objects.

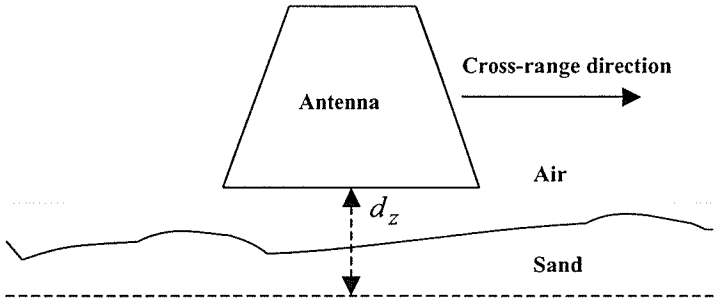

Figure 5.9 Distance *dx* in which the surface bin is searched.

Transition Detection

Once the sand surface bin *sbin* has been estimated in $s_{cder\,n,m}$ and removed, now the idea is to search for transitions in the responses under the surface of the sand as the GPR moves along in the cross-range direction. This is performed by computing the power of the difference vector $s_{cder\,n,m}$, which is equivalent to obtaining the *mean square error* between the two adjacent columns used to obtain $s_{cder\,n,m}$

$$sMSE_m = \frac{1}{N - sbin} \sum_{n=sbin}^{N} \left| s_{cder\,n,m} \right|^2 . \tag{5.21}$$

Figure 5.10 shows a plot of the mean square error *sMSE* obtained by applying (5.21) to all the incoming $s_{cder\,n,m}$ columns for the case of a plastic mine buried in sand. As it can be noticed, there is a significant contrast between the columns containing only sand, and the ones containing sand with a buried landmine. The MSE is helpful then as an indicator of the power changes from the current GPR position with respect to the previous one. A threshold T_1 is intuitively defined in order to detect significant changes. The threshold can be defined by visual analysis of the *sMSE* plot, or by analyzing its histogram as shown in Figure 5.11.

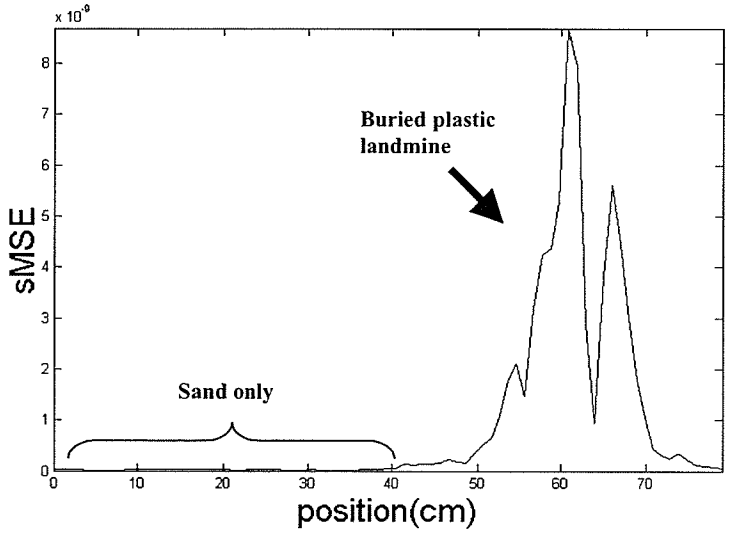

Figure 5.10 sMSE plot for the case of a plastic mine buried in sand.

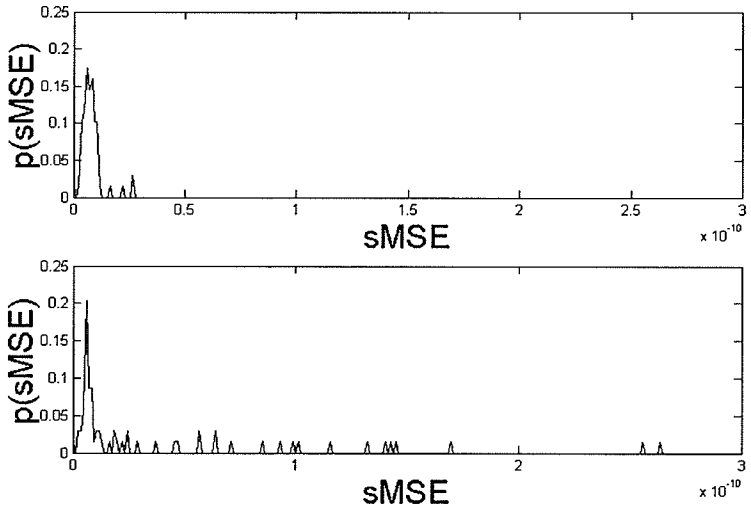

Figure 5.11 Estimated pdf for the sMSE of the data with sand only (top), and the data with a buried plastic mine (bottom).

In Figure 5.11 the sand-only plot shows MSE values up to 0.25×10^{-10}, then a threshold can be chosen at $T_1 = 0.5\times10^{-10}$. Hence, all the columns $s_{cder_{n,m}}$ with *sMSE* values above T_1 will be considered as candidates to contain a buried object response.

Reference Subtraction

A reference subtraction approach is followed in this thesis, in which the received signal is viewed as the sum of different contributors as follows:

$$s_{cmp_{n,m}} = c_{a_{n,m}} + c_{b_{n,m}} + t_{n,m}, \tag{5.22}$$

where $c_{a_{n,m}}$ is a homogeneous clutter (i.e. sand), $c_{b_{n,m}}$ is a non-homogeneous clutter contributor (i.e. rocks.), and $t_{n,m}$ is the contribution of a known target under search (i.e. plastic mine). A reference column s_{ref_n} is defined as an approximation of the homogeneous clutter response. It is initialized with the first incoming $s_{cmp_{n,m}}$ column as $s_{ref_n} = s_{cmp_{n,1}}$, which is generated by performing a scan with the GPR over a surface position in which it is assumed that no buried object is present. A reduction of the response contribution from $c_{a_{n,m}}$ is performed by applying the subtraction

$$s_{sub_{n,m}} = s_{cmp_{n,m}} - s_{ref_n}. \tag{5.23}$$

The obtained $s_{sub_{n,m}}$ column contains the combined responses of the desired target $t_{n,m}$ and the non-desired targets $c_{b_{n,m}}$ that can be any object which is not sand nor a plastic mine. The absolute value of $s_{sub_{n,m}}$ is appended as a new column into the final image *F*, s_{ref_n} is stored in memory and the GPR is moved to the next position.

Besides knowing that a power change occurred by monitoring *sMSE* as explained before, it is necessary to have an idea of how similar the new incoming column $s_{cmp_{n,m}}$ is to the stored reference s_{ref_n}, which is an "object-free" column. Hence, in order to have a similarity indicator, the mean square error *rMSE* is computed from $s_{sub_{n,m}}$ as

$$rMSE_m = \frac{1}{N - sbin} \sum_{n=sbin}^{N} \left| s_{sub_{n,m}} \right|^2. \tag{5.24}$$

A threshold T_2 is defined for *rMSE* in the same way as T_1.

At this point *sMSE* and *rMSE* are two indicators that will be used in order to detect transitions in the sand as well as differences with respect to an object-free area. The following cases are considered for the *sMSE* and *rMSE* indicators: (Refer to Figure 5.12).

1. -$sMSE < T_1$ and $rMSE < T_2$. This will indicate that there was no energy change, and that the new scan is similar to the one from an object-free region. An hypothetical example would be a region in which there is only sand and no buried object.

2. – $sMSE < T_1$ and $rMSE > T_2$. There was no energy change, and the scan is not similar to the one from an object-free region. An hypothetical example would be an object-free region in which the sand condition is slowly changing (i.e. if humidity of the sand changes gradually).

3. - $sMSE > T_1$ and $rMSE < T_2$. There was a change in the energy, and the scan is similar to the one from an object-free region. An hypothetical example would be a region that has a small strong reflector that caused a sharp transition, however small enough to be comparable to an object-free region.

4. -$sMSE > T_1$ and $rMSE > T_2$. There was a change in the energy, and the scan is not similar to the one from an object-free region. An hypothetical example would be a region in which there is a buried object and the region is definitely not an object-free region.

Reference update

In this work, the occurrence of cases 1 or 3 are used to take the decision of updating the reference column s_{ref_n}. The update is performed by simply copying the latest $s_{cmp_{n,m}}$ column into s_{ref_n}. If cases 2 or 4 occur, s_{ref_n} is not updated until the updating criteria is met again. Figure 5.12 shows the plots for *sMSE* and *rMSE* for the case of a landmine buried in sand. Figure 5.14 shows the final image obtained by applying the whole algorithm while a GPR scans a 1-meter long strip of the surface of the sand in which a plastic landmine is buried at a depth of 5cm. It can be noticed that the weak responses of the plastic landmine are significantly enhanced. Because the estimated surface bin is available, the system draws the surface on the image. For comparison purposes, Figure 5.15 shows the image obtained by the conventional image formation method, by applying range processing (without the use of derivative) and SAR processing, according to the

flow diagram shown in Figure 5.1. For illustration purposes, Figure 5.13 shows the obtained final image without SAR processing.

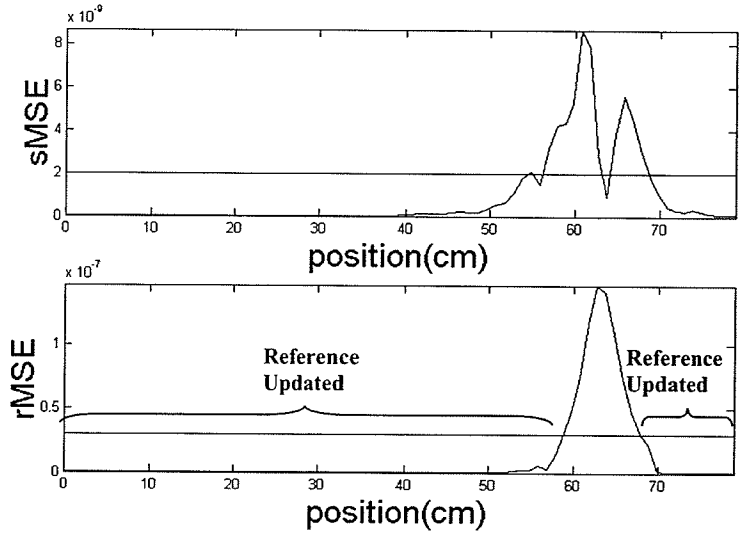

Figure 5.12 Plots of *sMSE* and *rMSE* indicators and thresholds showing where the reference vector is updated.

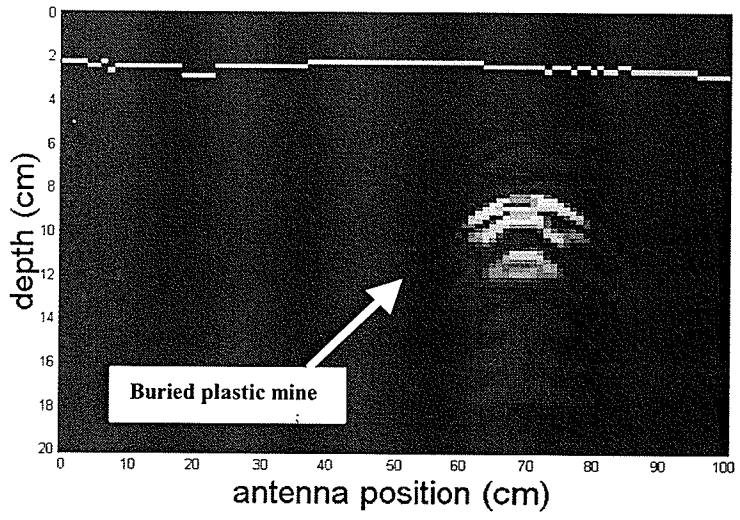

Figure 5.13 Image obtained by applying the algorithm without SAR processing.

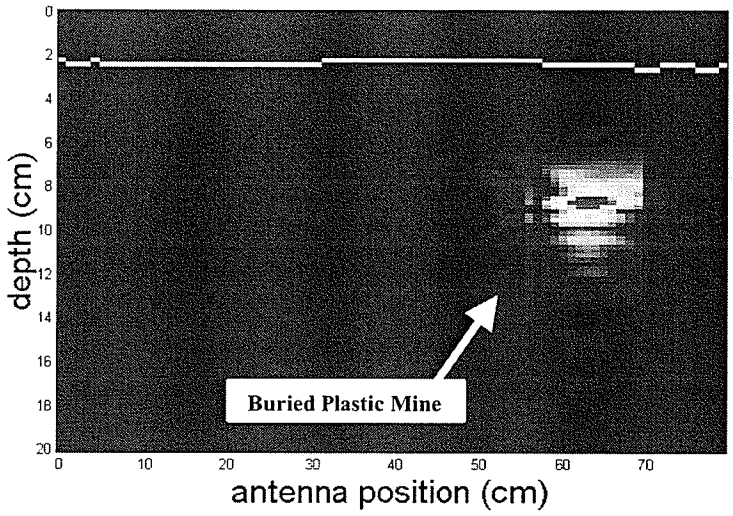

Figure 5.14 Final obtained image of a plastic mine buried in sand after applying the algorithm.

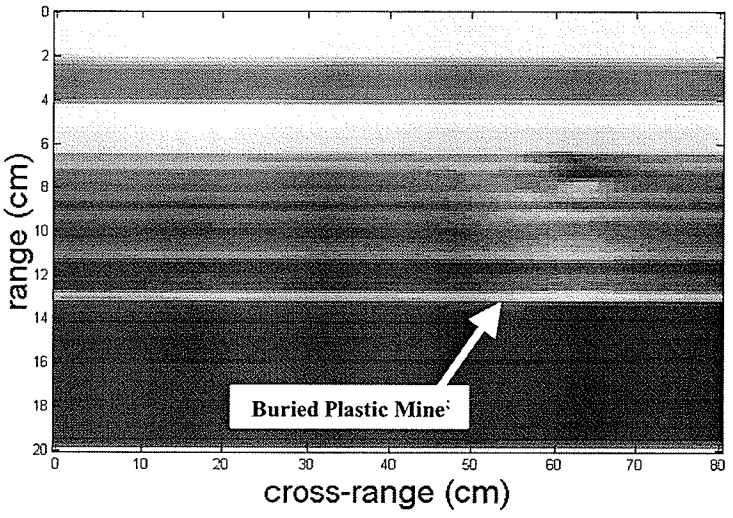

Figure 5.15 Image obtained by applying range processing (without the use of derivative) and SAR processing only.

6. System set up and implementation

6.1 Sandbox setup

In order to perform laboratory experiments to develop and test the imaging algorithm explained in the previous section, a wooden sandbox was designed and constructed. Its dimensions are: length=4.35m, width=1.1m, and height of the box=0.6m. A 15cm layer of anechoic chamber microwave absorbers was installed in the bottom of the box in order to attempt to reduce the reflections from the floor, then the sandbox was filled up with dry children-playground type sand, achieving an approximated depth of 25cm. The sand is homogeneous (it does not contain small rocks or any other bodies) with uniform grain size and an approximate permitivity of $\varepsilon = 3$. The sandbox was installed on the fifth floor of the engineering building at the University of Manitoba. Figure 6.1 shows a picture of the sandbox, and Figure 6.2 depicts a cross section diagram of the sandbox.

Figure 6.1 Sandbox used in this thesis.

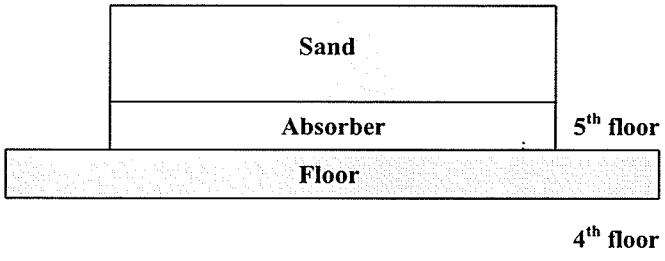

Figure 6.2 Cross section of the sandbox.

The horn-type antenna shown in Figure 6.3 was used in monostatic mode with a zero angle of incidence. It was mounted on a motorized mechanism in order to enable

automatic scanning. Table 6.1 summarizes the antenna specifications. The physical dimensions of the antenna are shown in Figure 4.5.

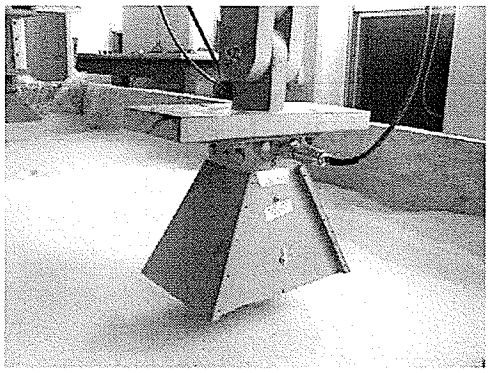

Figure 6.3 Horn type antenna.

Part #	Gain (dB)	Frequency Range (GHz)	Beamwidth (Degrees)
AEL H-1479	11 dB	1 ~ 12.4 GHz	50

Table 6.1 Antenna specifications.

The plastic landmine to be detected is shown in the Figure 6.4. It is made of plastic and it does not contain any conductive components. It was filled with candle wax in order to simulate the explosive material, which is assumed to be TNT. The physical dimensions of the landmine are: 14cm x 6.5cm x 3.5cm. Limestone rocks such as the one in the figure were also buried during the experiments. Table 6.2 summarizes the dielectric constants of the involved materials in the imaging problem.

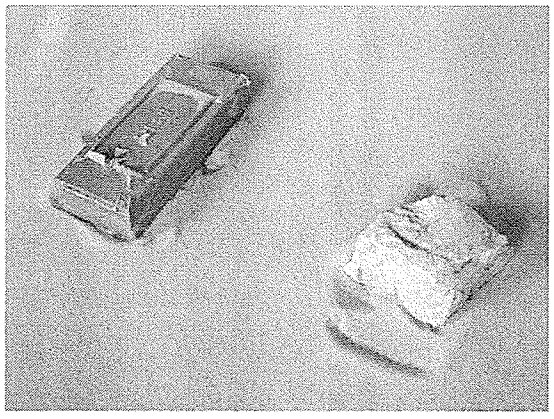

Figure 6.4 Plastic landmine and rock .

Material	Dielectric Constant (ε)
Sand	3~6
Plastic	2.67
Candle wax	2.2~2.3
Limestone rock	7~9
TNT	2.86

Table 6.2 Dielectric constants of the objects involved in the imaging problem.

6.2 GPR imaging system implementation using a 360B network analyzer

The system developed in this thesis was originally targeted to complement the GPR hardware shown in Figure 3.1. However, due to the limited 1 GHz bandwidth supported by that GPR, and the requirement of high range resolution by the algorithm presented in section 5, a network analyzer is used instead of that GPR hardware in the implementation of the system. In fact, all the images and plots shown in the explanation of the algorithm in section 5 where generated by using this system. Although the network analyzer can reach frequencies up to 40 GHz, the images were generated considering the maximum frequency operating range of the horn antenna.

Hardware Architecture

A Wiltron 360B network analyzer was used to transmit and receive the microwave signals. It is operated in a single channel mode S11, hence requiring the use of a single antenna to transmit and receive. Figure 6.5 shows a picture of the network analyzer.

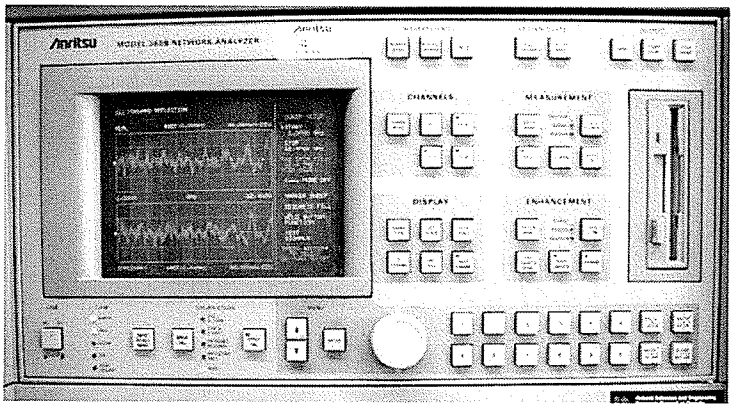

Figure 6.5 360B network analyzer used to transmit and receive the microwave signals.

A computer is used to fully control the network analyzer by using its IEEE-488 GPIB interface. A National Instruments GPIB-ENET/100 Ethernet-to-GPIB interface box is used to link the computer with the instrument. After one scan is performed by the network analyzer at a cross-range position, both I and Q data vectors are transferred to the computer in order to apply on-the-fly processing. Then, the computer activates the

motor at the sandbox in order to move the antenna automatically to the next cross-range position. Figure 6.6 shows a diagram of the system.

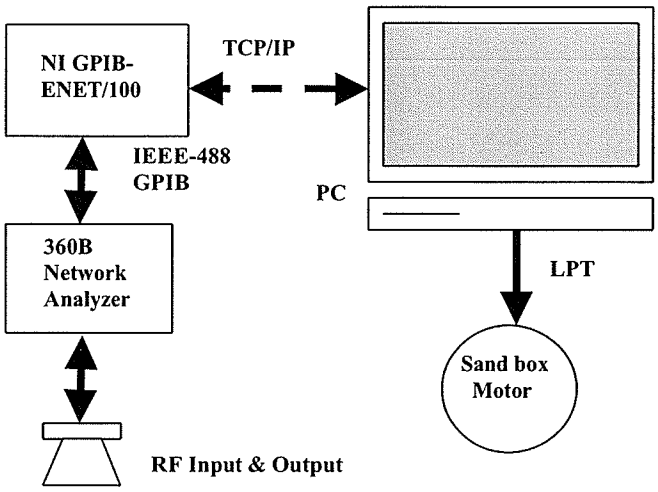

Figure 6.6 Diagram of the GPR imaging system hardware implementation with a network analyzer.

Software Architecture

A graphical user interface was developed in order to control the system as shown in Figure 6.7. By using this GUI, the user is able to specify the GPR parameters, control the motor for positioning, control the scanning mode and save the formed image and the acquired raw data at the computer. All of the controls in the GUI are self-explanatory except for the "# of freq points frame" in which there are three options: Max, Medium and Min. By selecting any of these options, the network analyzer will define the "maximum, normal or minimum" number of steps that it can support based on the specified start and end frequencies. Therefore, the user does not have direct control of the frequency step Δf.

The GUI was developed in Visual C++. It uses the National Instruments GPIB-ENET/100 box application program interface to make a link between the computer and the network analyzer through the GPIB box.

The signal processing algorithm explained in section 5 was implemented in Matlab in order to take advantage of its mathematical and graphical libraries. The GUI controls the Matlab program by making use of the functions provided by the Matlab Engine. When a vector containing the I and Q data is received from the network analyzer, it is copied into a Matlab array and the signal processing code is run immediately, hence displaying an updated GPR image at the computer monitor. Figure 6.8 shows the software architecture diagram for this system.

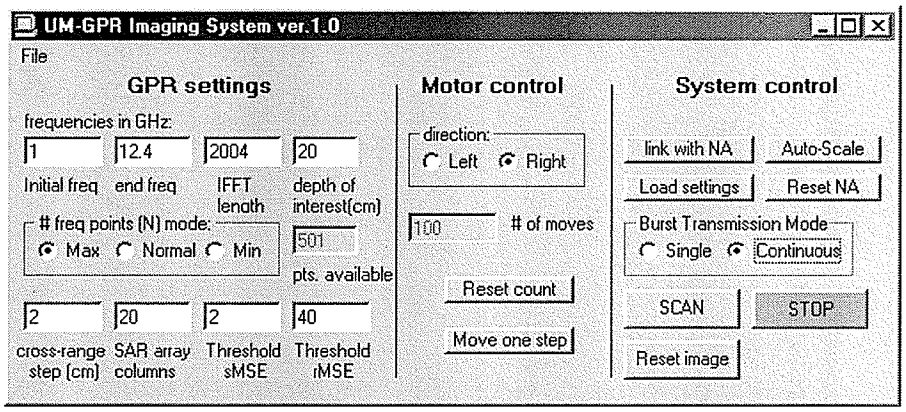

Figure 6.7 GPR imaging system graphical user interface.

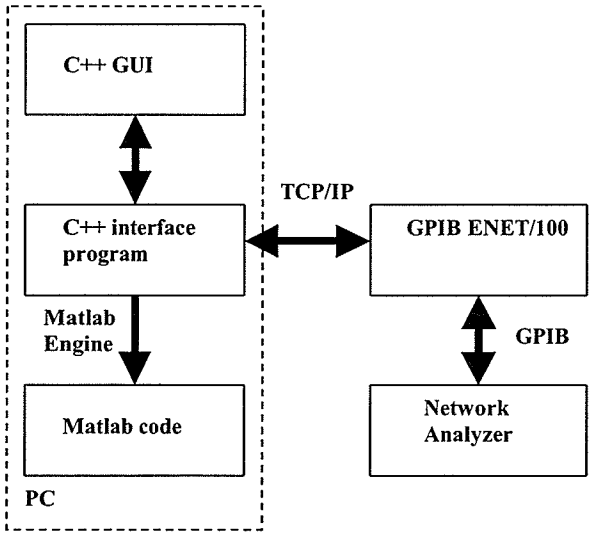

Figure 6.8 Software architecture used in the system.

6.3 GPR imaging system implementation with a TMS320C6211 DSP board

Because a second version of the hardware shown in Figure 3.1 will support a higher bandwidth, a signal processing system was implemented to control the hardware in order to generate the transmitted frequencies, sample the I and Q analog signals and process the data in order to produce an output image at the computer monitor.

Hardware Architecture

The GPR hardware was previously controlled by a Microchip PIC16C774 8-bit micro-controller running at 4MHz which has an A/D converter in order to sample and store the data in an EEPROM memory. However, after each cross-range position scan, the acquired data vector had to be manually transferred to an external computer in order to apply post-recording processing in a Matlab program. The flexibility of the system was very limited, because no parameters other than the number of frequencies N could be modified for experimentation. In order to improve the scanning speed and the flexibility of the system, an embedded real-time processing system was implemented. A Texas Instruments TMS320C6211 digital signal processing development kit (DSK) was used with a 12-bit analog-to-digital conversion daughter board THS1206 EVM in order to sample the I and Q analog signals from the GPR. Figure 6.9 shows a picture of the DSK with the ADC module mounted on it.

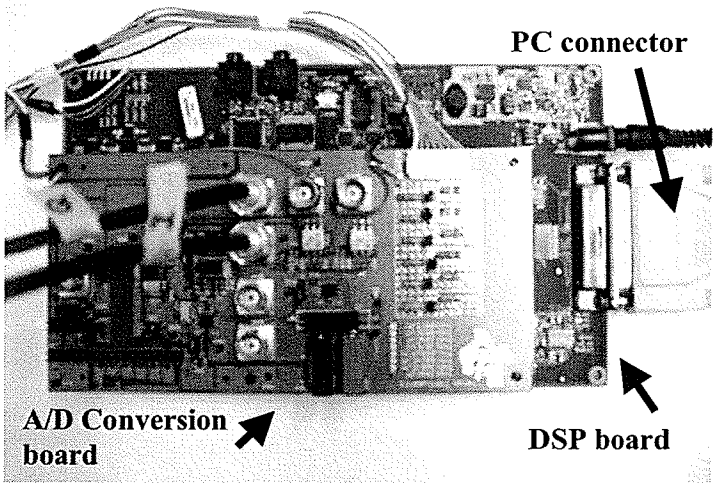

Figure 6.9 TMS320C6211 DSP board used in the implementation of the system.

The board was programmed in C language in the Code Composer Studio IDE at a computer connected to the DSK board. Then, each time a version of the program is built, it is easily loaded from the PC into the DSK board in order to start running. A diagram showing the complete system is shown in Figure 6.10.

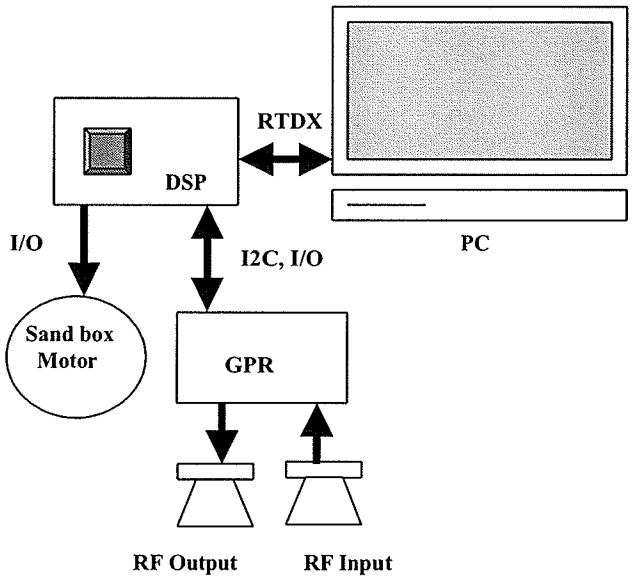

Figure 6.10 Diagram of the system implementation using the GPR hardware developed at the university of Manitoba.

The I/O ports of the board were used to implement the I2C Phillips communications protocol to control four voltage control oscillators (which produce the generated output frequency) at the GPR as explained in section 3. Other I/O lines were used to control the RF switch to select the output of the desired VCO and the motor driver installed on the sandbox. Finally, the transceiver's I and Q analog signals at the IQ demodulator operational amplifier outputs are directly connected to the inputs of the THS1206 ADC in order to be sampled.

Software Architecture

At the PC, a graphical user interface was developed in order to control the program running on the DSP board. The RTDX (real-time data exchange) Texas Instruments system was used to send control commands to the DSK while the program is running, hence greatly improving the flexibility for the user to modify the GPR parameters. This protocol was also used to transfer the output data vector from the DSK to the computer. The graphical interface was made in Visual Basic. The program running at the DSK was written in C language, and the post-processing and image display program at the PC was written in Matlab. In order to control the Matlab program running at the PC from within the GUI, a link was made by using Windows COM/Activex technology. Figure 6.11 shows the software architecture diagram for this system, and Figure 6.12 shows a picture of the actual system.

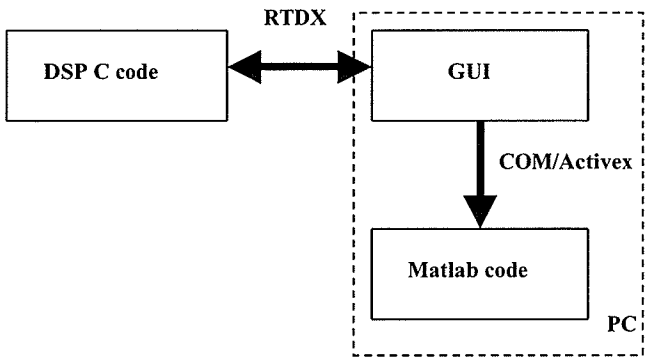

Figure 6.11 Software architecture used with the GPR hardware.

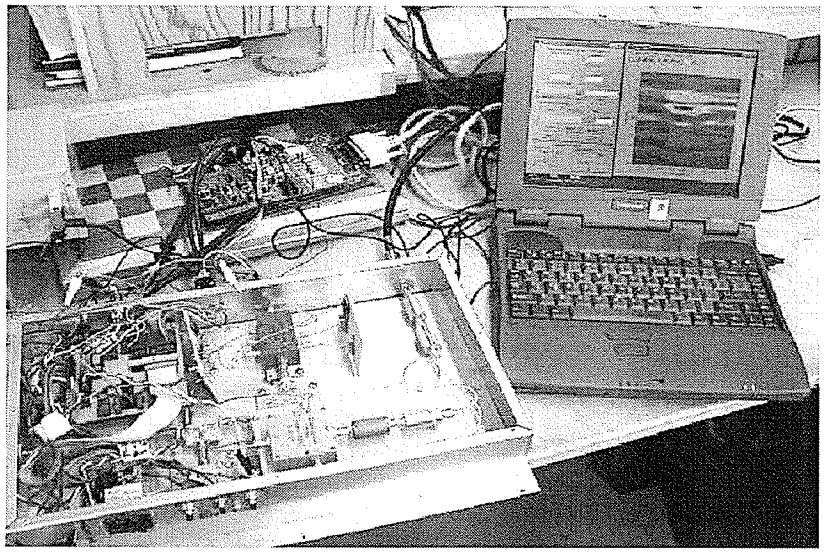

Figure 6.12 Imaging system using the GPR hardware developed at the University of Manitoba.

7. Experiments with the imaging system

This section presents a set of experiments performed with the imaging system by using the network analyzer. In the experiments, the plastic landmine is buried in sand, and images are generated in order to obtain its response and be able to identify it.

The objectives of the experiments are:

- To test each process of the system and confirm its operation.
- To detect limitations of the system.
- To compare the images with images obtained with clutter reduction techniques.
- To define new research points.

As mentioned in section 6, the selection of the frequency step Δf and the number of steps N in the network analyzer is restricted. Table 7.1 summarizes the possible instrument settings to achieve a range resolution close to $\Delta rs = 8$ mm in sand as defined in section 4. The setting #3 was used in the experiments shown throughout this section and the transmission power of the network analyzer was fixed at 5dBm.

Instrument setting	data points N+1	freq step Δf	bandwidth β	max range *dmax*	resolution Δrs
1	85	136.8MHz	11.49GHz	66.68cm	7.84mm
2	168	68.4MHz	11.42GHz	1.33m	7.9mm
3	501	22.8MHz	11.4GHz	4m	8mm

Table 7.1 360B network analyzer settings to obtain a range resolution close to 7mm.

The setup shown in Figure 7.1 was used in the experiments. A coordinates system with origin (x = 0, y = 0, z = 0) was defined in order to locate the buried objects. Scans are performed along three paths on the y-axis. Table 7.2 lists all of the objects (and their physical dimensions) used in different experiments, which include a plastic landmine.

Note: Since SAR processing is applied as explained in section 4, the set of columns corresponding to the first and the last 10cm of collected data in the cross-range direction are not displayed in the images shown in this section. The reason of not displaying the columns at those locations is that those columns were only used to synthesize the first and the last displayed columns in the images. Therefore an offset of 10cm should be added to the horizontal axis of the images shown in this section.

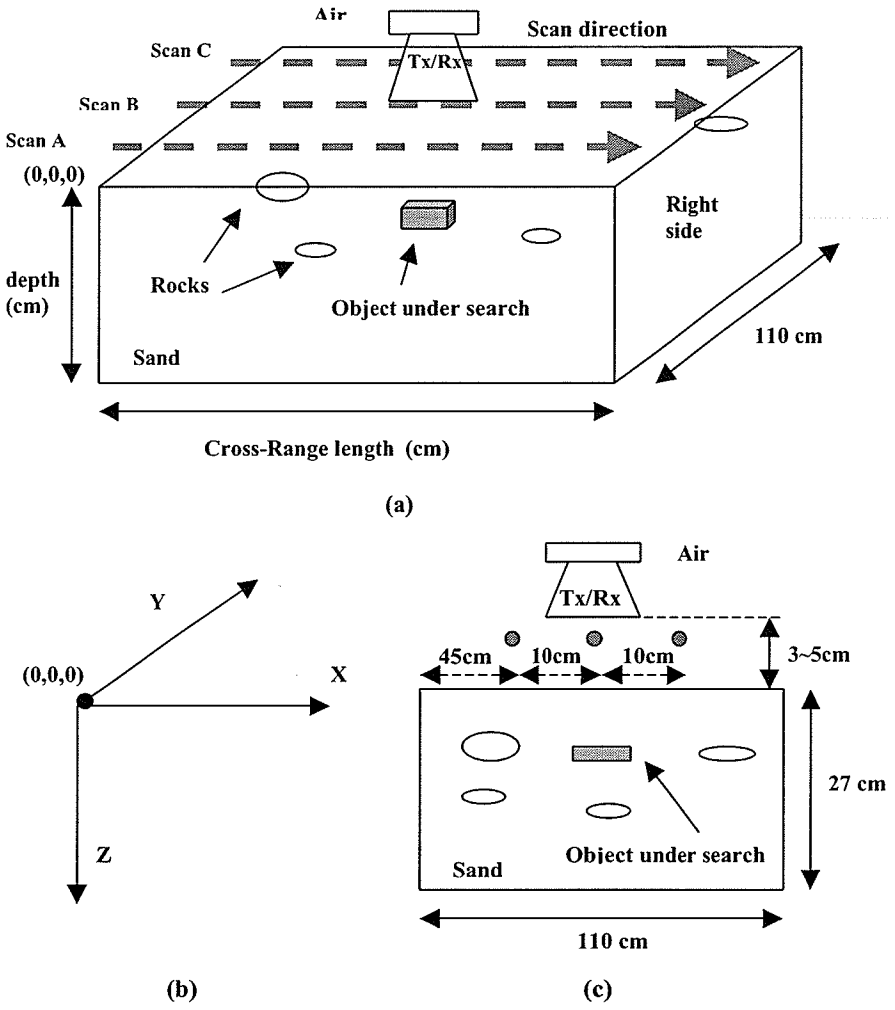

Figure 7.1 (a) Experiments setup showing the three scanning lines, (b) Used coordinates system, (c) Side view of experiments set up.

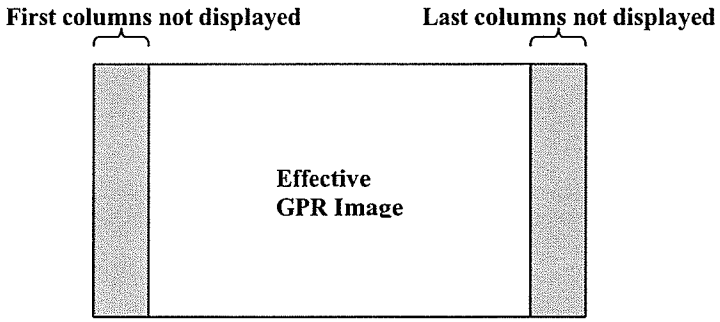

Figure 7.2 Columns not displayed in the images.

	Object dimensions (cm)		
Object	Length	Width	Height
Square Mine	14	6.5	3.5
Rock 1	8	7	4
Rock 2	7.5	4	4
Rock 3	8	8	6
Rock 4	8	5	4
Rock 5	8	4.5	2.5
Rock 6	7	5	3.5
Rock 7	7	4	3
Rock 8	5.5	3.5	3
Rock 9	7.5	4	3
Rock 10	7	5	3
Rock 11	6.5	3.5	3
Rock 12	6	4	3.5
Rock 13	6	4	3

Table 7.2 Objects used in the experiments and their physical dimensions.

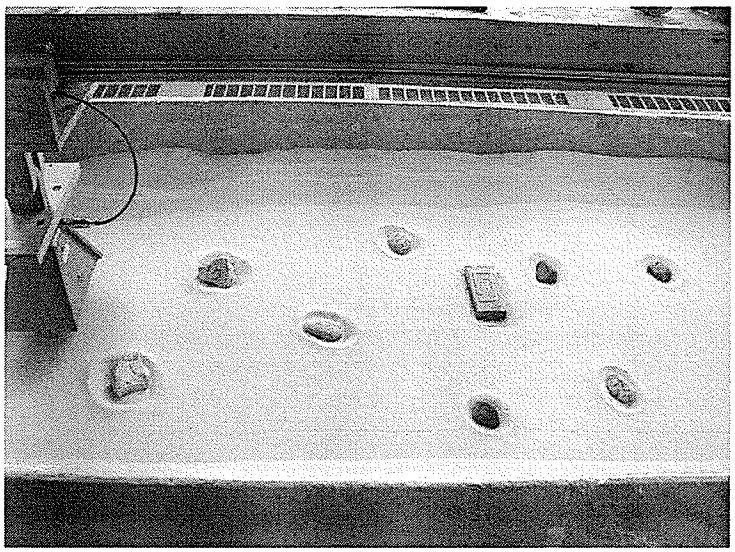

Figure 7.3 Example of objects locations before burying them.

7.1 Experiment 1. Imaging of plastic mine and rock with flat and rough surface.

Objectives:

1. -To verify the performance of the surface removal process in the algorithm.
2. -To confirm the detection of the plastic mine when it is alone and when other objects are buried.

Conditions:

Eight scans are taken in this experiment. The following table summarizes the conditions.

Conditions:		
Separation Antenna-Sand:	2cm	0 = Not present
Cross Range step in x axis:	1cm	1 = present (buried)
Cross Range length:	100cm	
Antenna scan position:	B	

Scan	Sand's surface	Rock1 @(30,55,5)	Mine @(70,55,5)
1	Flat	0	0
2	Flat	0	1
3	Flat	1	0
4	Flat	1	1
5	Rough	0	0
6	Rough	0	1
7	Rough	1	0
8	Rough	1	1

Table 7.3 Conditions for experiment 1.

Examples of the two sand surface conditions are shown in Figures 7.5 and 7.6 for flat and rough surfaces respectively.

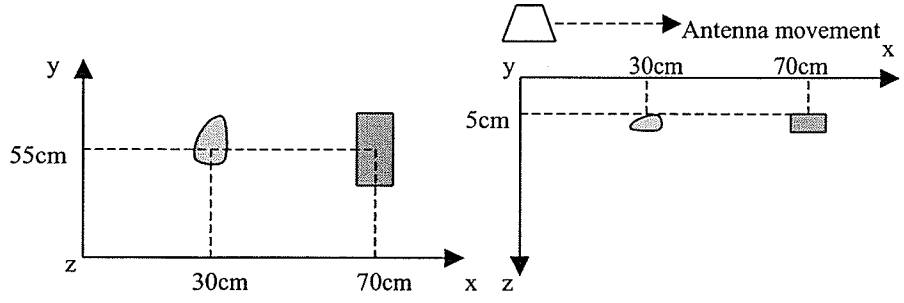

Figure 7.4 Experiment 1 (Left) Top view, (Right) Side view.

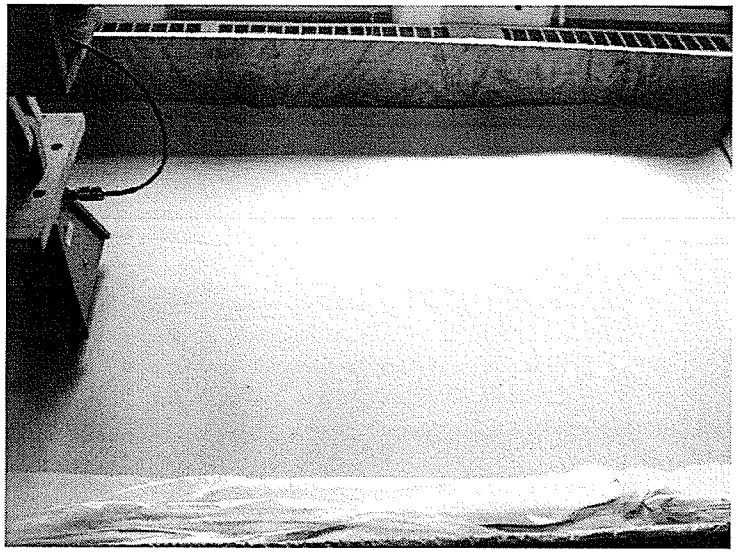

Figure 7.5 Flat surface.

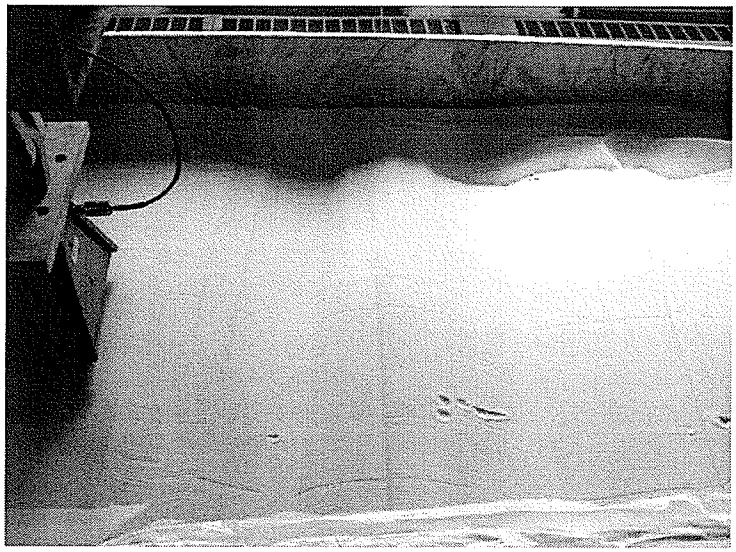

Figure 7.6 Rough surface. The peak-to-peak amplitude of the waves is from 1 to 2 cm.

Results: The images obtained from the 8 scans of experiment 1 are shown in the figures 7.7 to 7.14.

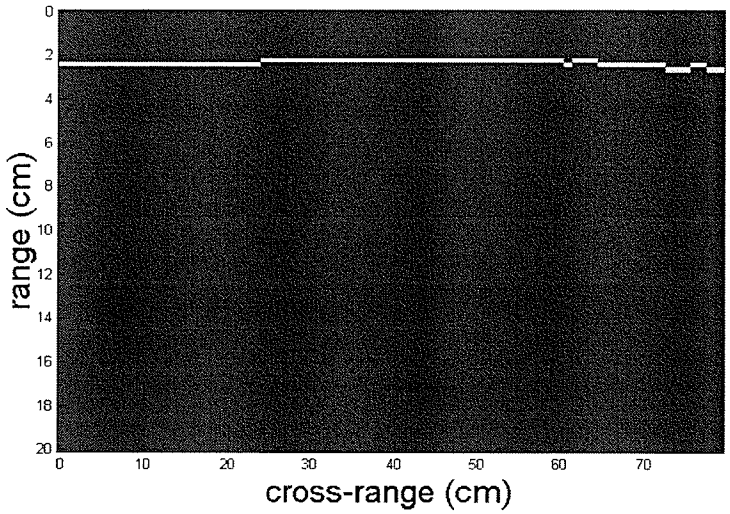

Figure 7.7 Sand with flat surface (scan 1).

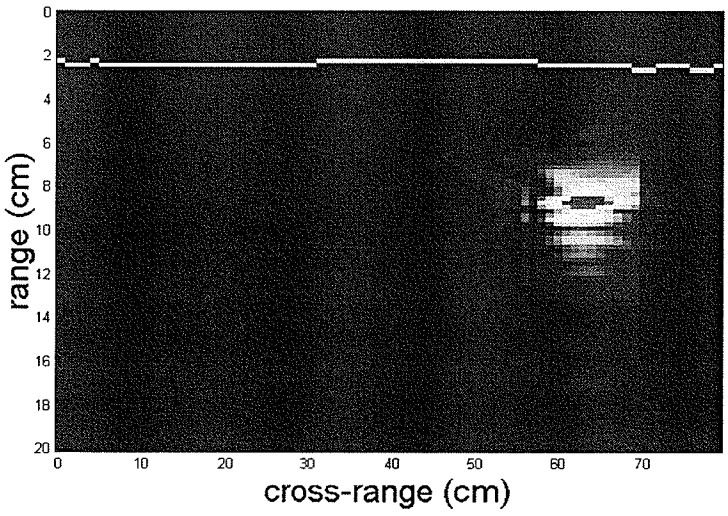

Figure 7.8 Buried mine in sand with flat surface (scan 2).

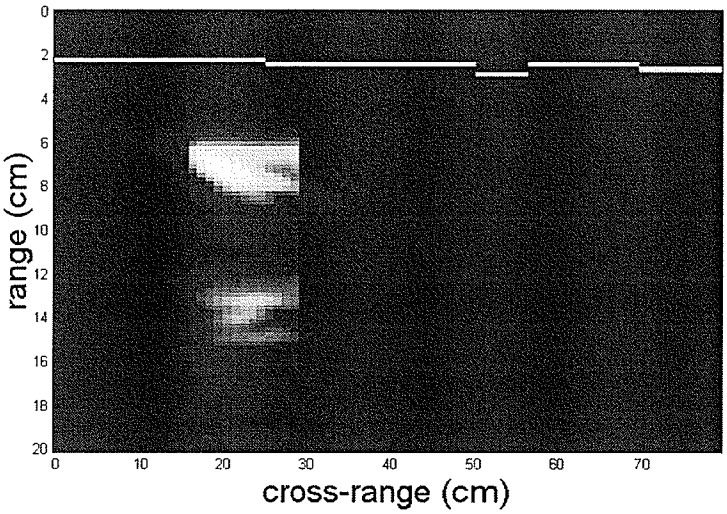

Figure 7.9 Buried rock1 in sand with flat surface (scan 3).

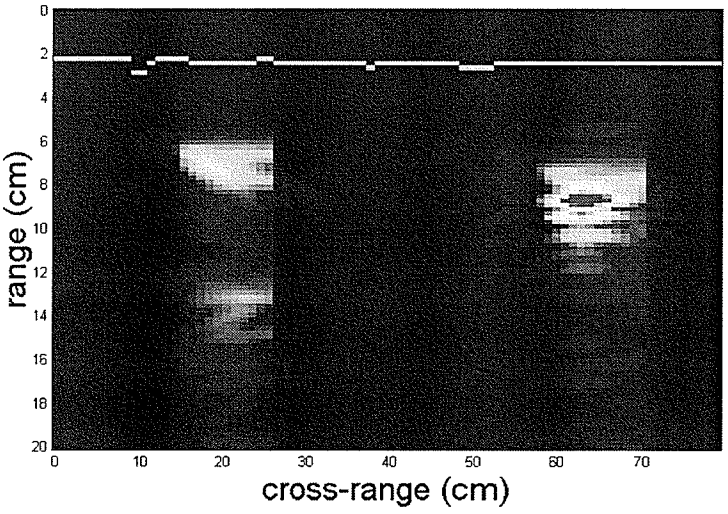

Figure 7.10 Buried mine and rock1 in sand with flat surface (scan 4).

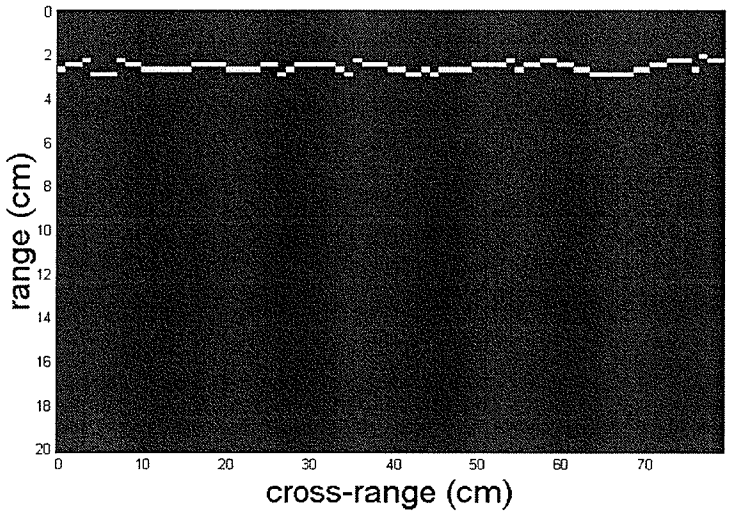

Figure 7.11 Sand with rough surface (scan 5).

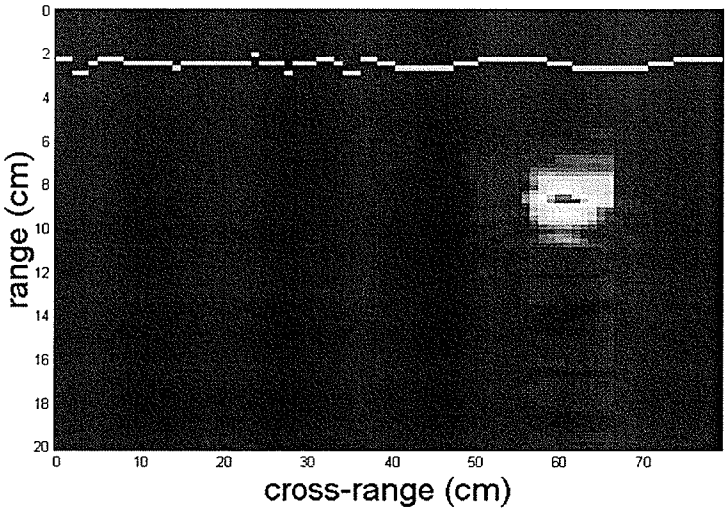

Figure 7.12 Buried mine in sand with rough surface (scan 6).

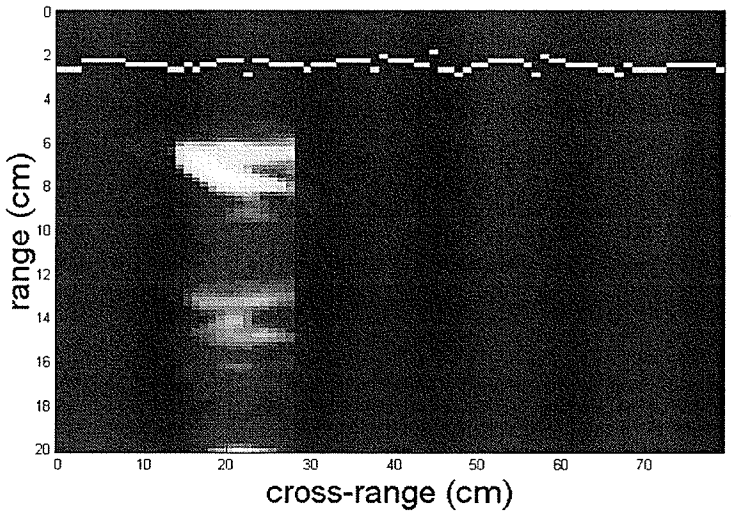

Figure 7.13 Buried rock1 in sand with rough surface (scan 7).

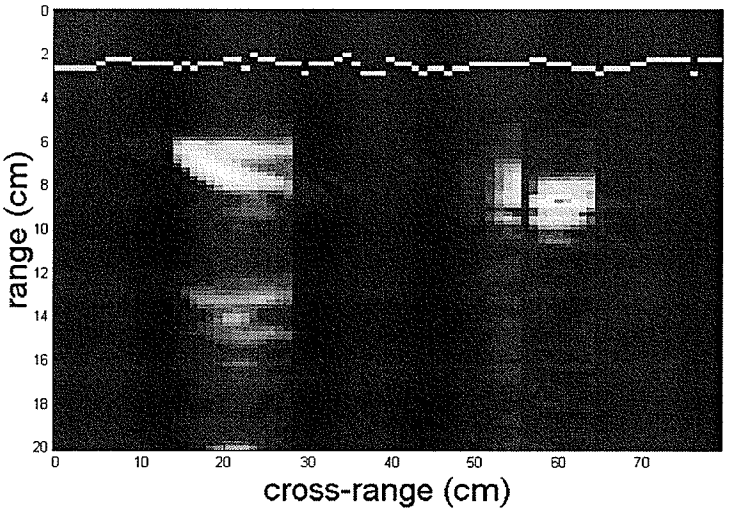

Figure 7.14 Buried mine and rock1 in sand with rough surface (scan 8).

Conclusions from experiment 1

1. -Visually, it was confirmed that a reasonable clean image of the plastic mine can be obtained with the algorithm in real-time, even if the surface is rough and a rock is present.

2. -The surface removal is helpful to overcome the drawback of having strong responses at the surface due to the use of the first derivative. Otherwise, the transitions generated by the surface changes would have a strong influence in the reference updating process.

3. - It is observed that the shapes of the mine and rock responses are different. As explained in [19], the characteristics of the rock, such as geometry, dielectric constant and moisture play an important role in its response pattern and in the propagation speed of the microwave signals that penetrate it. However, this response pattern difference can be exploited in order to discriminate the rock response and perform detection of the landmine.

4. – The beginning and the end of the reference updating can be viewed visually as it can be noticed in Figure 7.8, in which an update occurs at bins 57 and 70 in the cross-range direction.

5. – The responses of the buried objects are weaker when the surface is rough. A possible reason can be that the signals are reflected in a different angle, and the antenna receives less energy. This represents a problem if object recognition is to be performed.

7.2 Experiment 2. Imaging of plastic mine at different depths.

Objective: To confirm the system performance, and observe the effects when the plastic mine is buried at different depths.

Conditions: Six scans were taken in this experiment. The following table summarizes the conditions.

Conditions:	
Separation Antenna-Sand:	2cm
Cross Range step in x axis:	1cm
Cross Range length:	100cm
Antenna scan position:	B
Sand surface:	Flat

	Mine @(45,55,*)
Scan	**depth (cm)**
1	0
2	2
3	4
4	6
5	8
6	10

Table 7.4 Conditions for experiment 2.

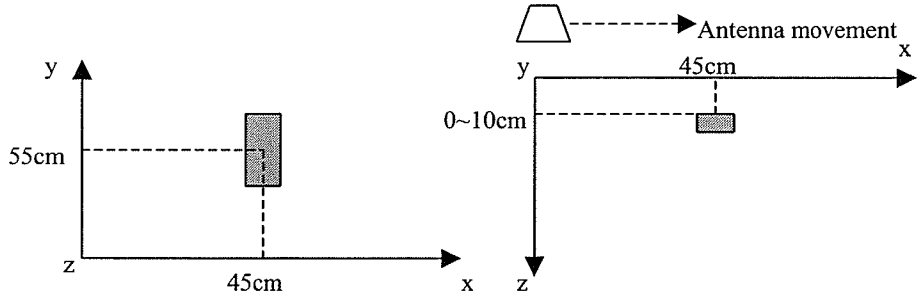

Figure 7.15 Experiment 2 (Left) Top view, (Right) Side view.

Results:

Figures 7.16 to 7.21 show the obtained images with the mine buried at different depths.

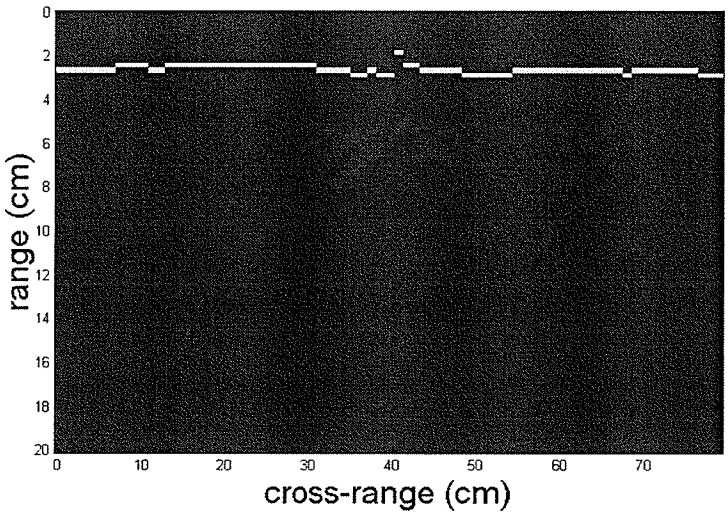

Figure 7.16 Plastic mine buried 0 cm (scan 1).

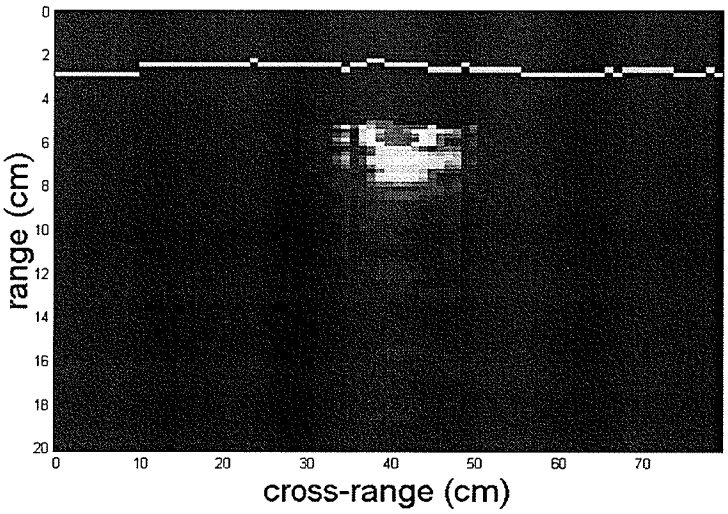

Figure 7.17 Plastic mine buried 2 cm (scan 2).

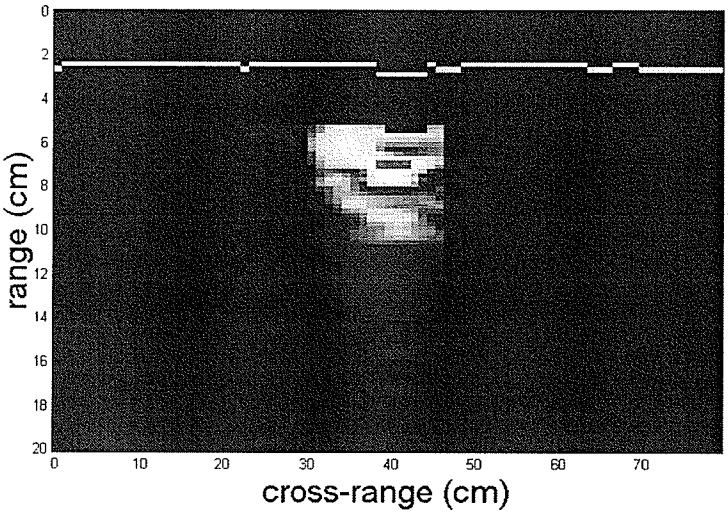

Figure 7.18 Plastic mine buried 4 cm (scan 3).

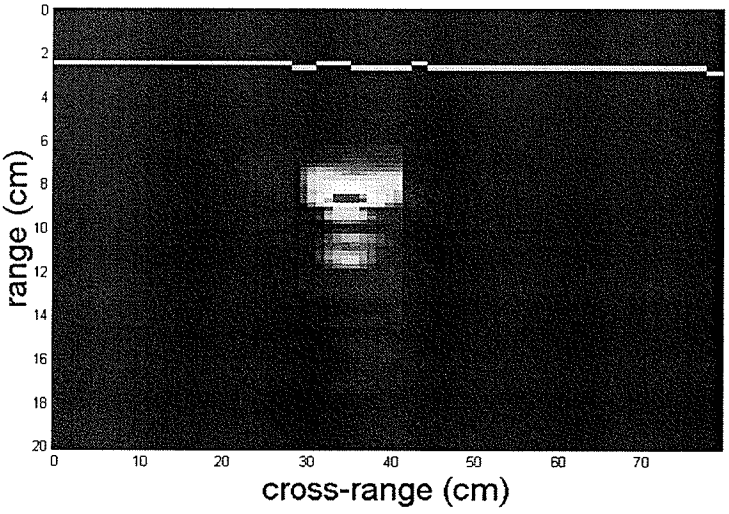

Figure 7.19 Plastic mine buried 6 cm (scan 4).

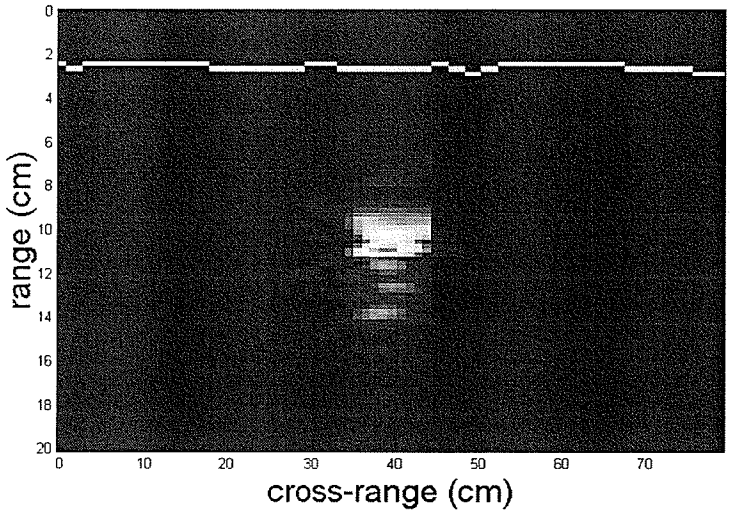

Figure 7.20 Plastic mine buried 8 cm (scan 5).

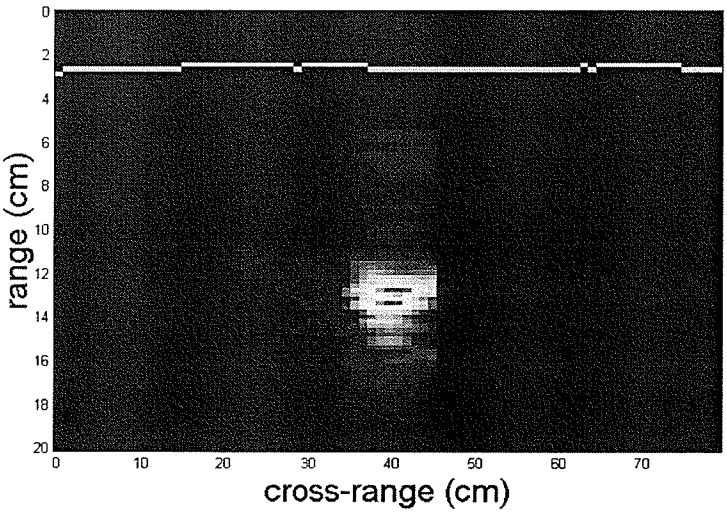

Figure 7.21 Plastic mine buried 10 cm (scan 6).

Conclusions from experiment 2

1. –Visually, it was observed that the mine depths in the images correspond to the actual measured depths. Hence the system works properly.
2. –When the object is at the same level of the surface or at short depths, the algorithm fails, as it can be observed in Figure 7.16. This happens because the surface removal process sets the first bins under the surface to zero. This is a drawback of the algorithm.
3. –The shape and intensity of the responses of the mine change with depth. Both of them may be caused by the exponential damping of the traveling signal in sand as explained in section 2, and by angular changes caused when the mine was buried. These are problems that have to be analyzed if automatic object recognition is to be performed.

Note: The horizontal location of the buried objects in the images vary sometimes because of variation in the accuracy of the motorized mechanism.

7.3 Experiment 3. The effect of burying a rock over and under a plastic mine.

Objective: To observe the effect of burying a rock over and under a plastic mine.

Conditions: Two scans are taken. The following table summarizes the conditions for the experiment.

Conditions:	
Separation Antenna-Sand:	2cm
Cross Range step in x axis:	1cm
Cross Range length:	100cm
Antenna scan position:	B
Sand surface:	Flat

	Rock1 @(50,55,*)	Mine @(50,55,*)
Scan	**depth (cm)**	**depth (cm)**
1	3	10
2	10	3

Table 7.5 Conditions for experiment 3.

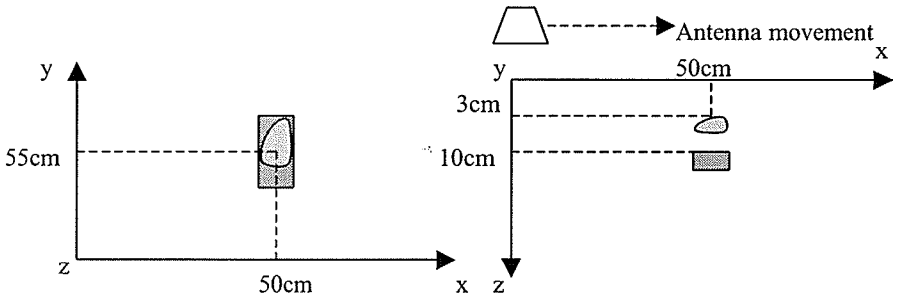

Figure 7.22 Experiment 3 (Left) Top view, (Right) Side view.

Results:

Figures 7.23 to 7.24 show the obtained images.

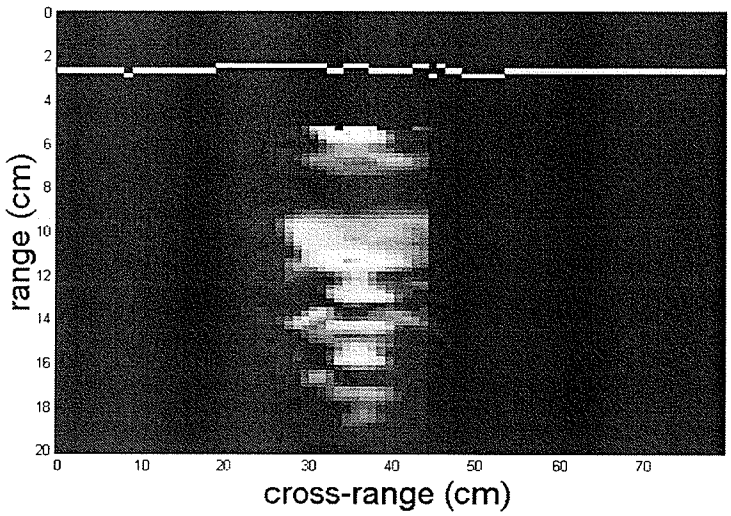

Figure 7.23 Rock over a plastic mine.

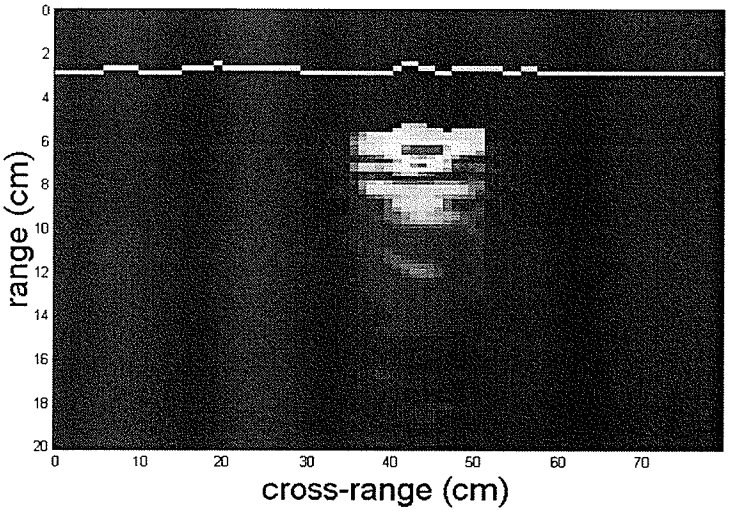

Figure 7.24 Mine over a rock.

Conclusions from experiment 3

1. –The response from the landmine seems to dominate the image. However, it can be noticed that its response is weaker when a rock is over it.
2. –It is more difficult to recognize the mine due to the interference between both objects.

7.4 Experiment 4. Imaging of a plastic mine and rock with different separations in the cross-range direction.

Objective: To observe the effect of the separation between a mine and a rock.

Conditions: Six scans were taken in this experiment. The following table summarizes the conditions for the experiment.

Conditions:	
Separation Antenna-Sand:	2cm
Cross Range step in x axis:	1cm
Cross Range length:	100cm
Antenna scan position:	B
Sand surface:	Flat
Mine:	(50,55,5)
Rock1:	(*,55,5)

Scan	separation (cm)
1	0
2	2
3	4
4	6
5	8
6	10

Table 7.6 Conditions for experiment 4.

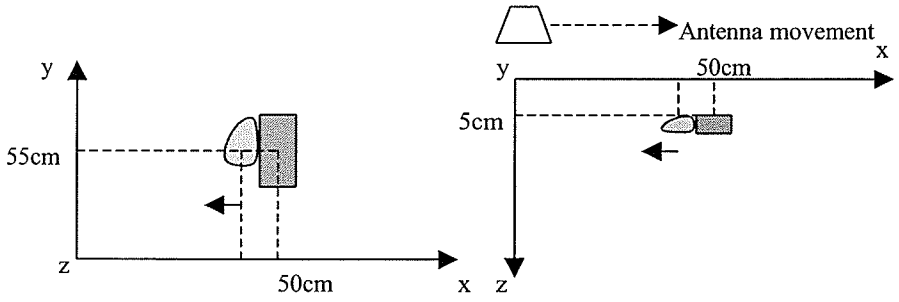

Figure 7.25 Experiment 4 (Left) Top view, (Right) Side view.

Results

Figures 7.26 to 7.31 show the obtained images.

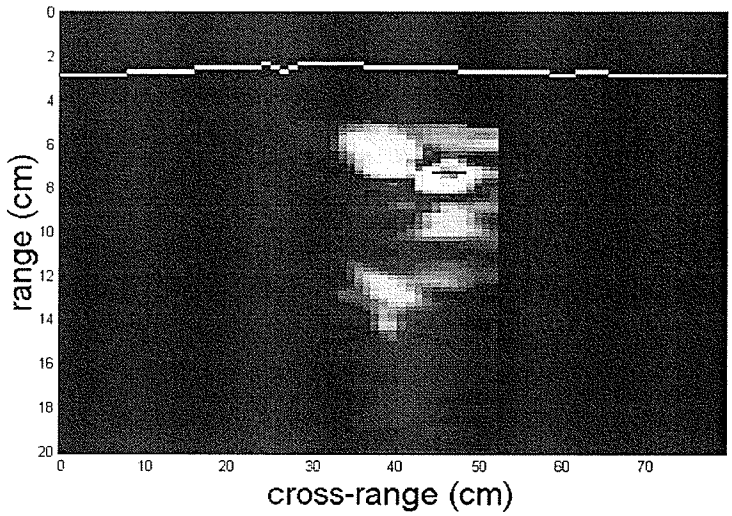

Figure 7.26 Mine and rock separated by 0 cm.

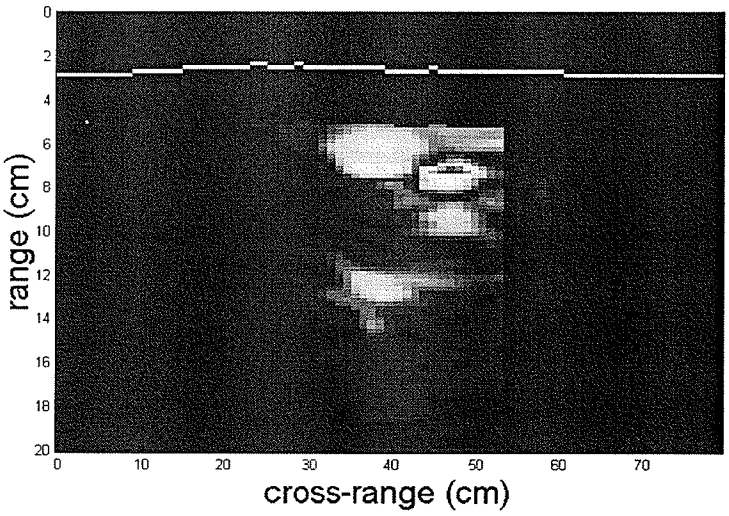

Figure 7.27 Mine and Rock separated by 2 cm.

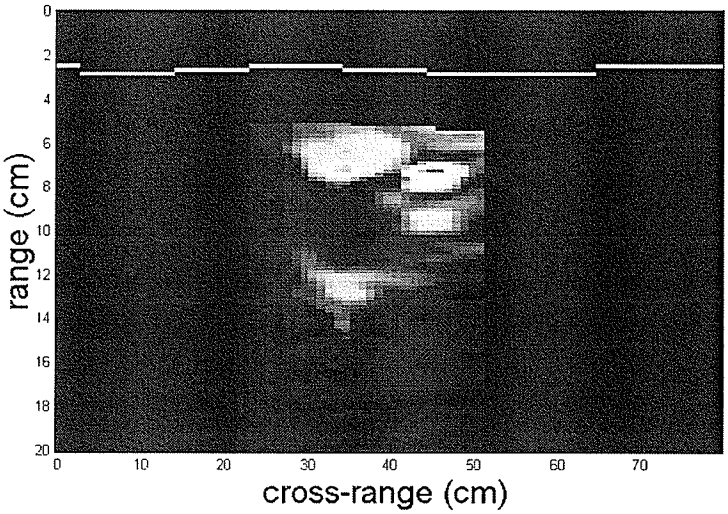

Figure 7.28 Mine and rock separated by 4 cm.

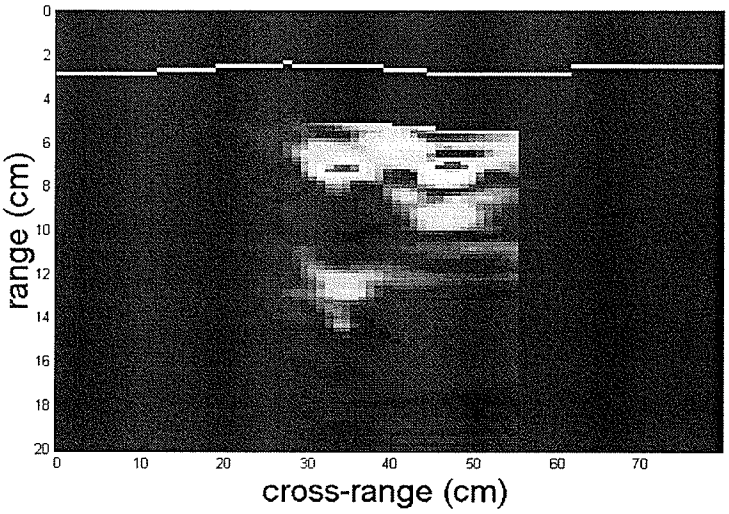

Figure 7.29 Mine and rock separated by 6 cm.

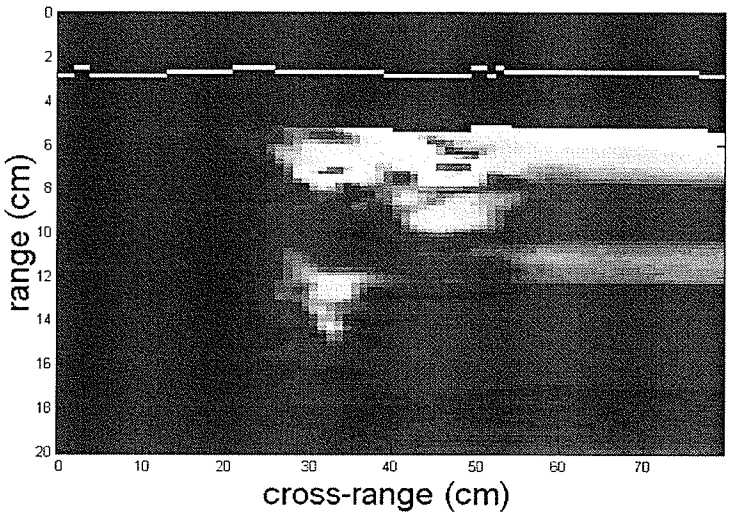

Figure 7.30 Mine and rock separated by 8 cm.

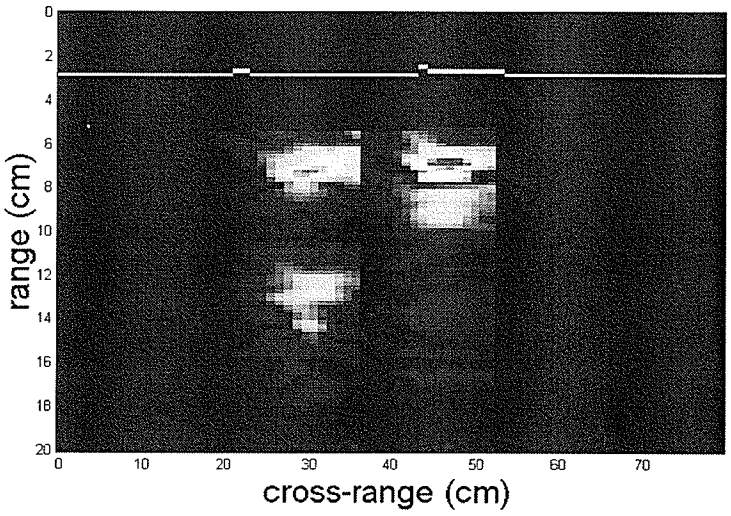

Figure 7.31 Mine and rock separated by 10 cm.

Conclusions from experiment 4

1. –The achieved cross-range resolution is enough to be able to visually differentiate the mine from the rock, even when their separation gap is zero.
2. –The reference was not updated until there was a separation of 10 cm. Hence, the algorithm considered both objects as a single object with respect to the reference updating process.
3. –In Figure 7.30, the reference was not updated after the 50^{th} antenna cross-range position. This is due to the selection of the thresholds. Adjustment might be necessary, or manual reference update.

7.5 Experiment 5. Imaging of a sand region containing a plastic mine and several rocks buried in diverse locations.

Objective: To observe the responses of the buried objects when they are not located exactly under the scanning path of the antenna.

Conditions: Three cross-range scans A, B and C were performed in a single set up as shown in Figure 7.1. Although 30 scans were performed with 10 different set ups, the results from only one which shows the typical results obtained are shown. Unlike the previous experiments in which the buried object is located exactly in the center of the antenna scanning path, here the objects are not necessary located in the center. The following table summarizes the conditions for the chosen set up.

Conditions:

Separation Antenna-Sand:	3cm
Cross Range step in x axis:	1cm
Cross Range length:	144cm
Antenna scan position:	A,B,C
Sand surface:	Rough

No.	Object	X(cm)	Y(cm)	Z(cm)
1	Square Mine	25	57	6
2	Round Mine	36	68	4.5
3	Rock 1	21	41	5
4	Rock 2	63.5	63	3
5	Rock 3	97	62	3
6	Rock 4	80	60	0
7	Rock 5	123	62	7
8	Rock 6	40	42	0
9	Rock 7	54	77	10
10	Rock 8	35	72	4
11	Rock 9	99	97	6
12	Rock 10			
13	Rock 11			
14	Rock 12			
15	Rock 13	100	42	2

Table 7.7 Conditions for experiment 5.

Results:

Figures 7.32 to 7.34 show the images obtained.

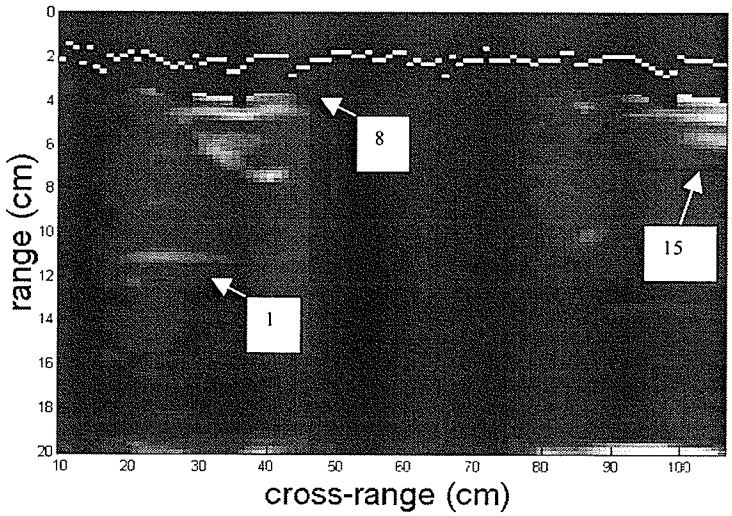

Figure 7.32 Scan A of experiment 5.

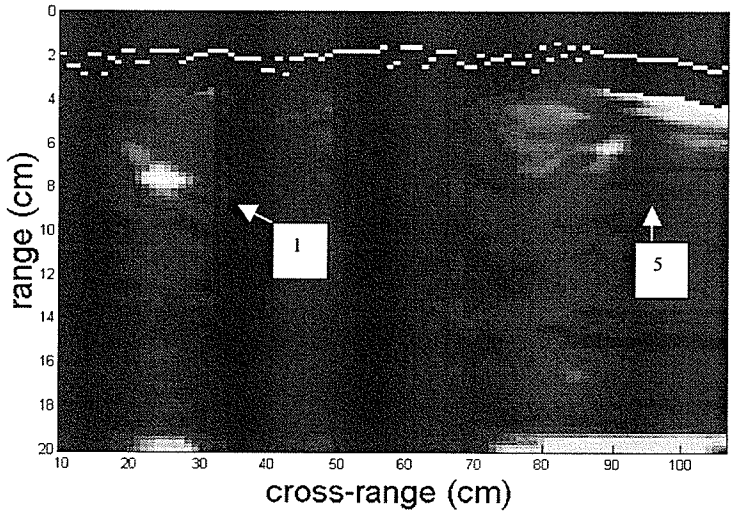

Figure 7.33 Scan B of experiment 5.

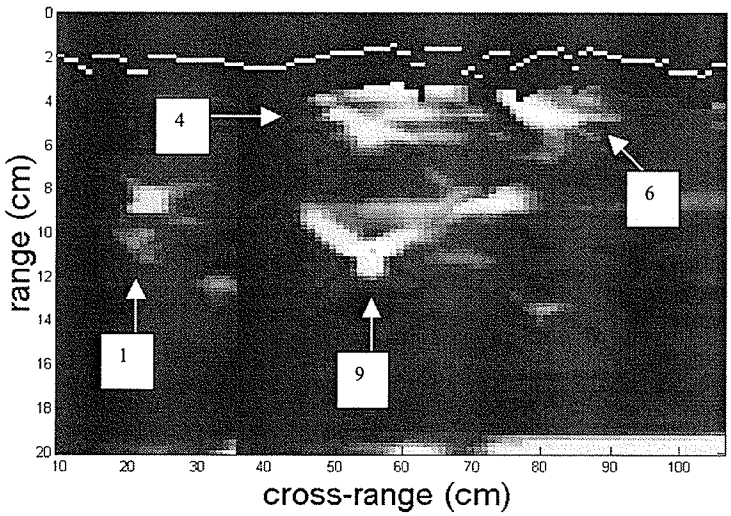

Figure 7.34 Scan C of experiment 5.

Conclusions from experiment 5

1. –It is observed that responses from the plastic mine appear in the three scans. However, their shapes, magnitudes and range positions are different. This occurs because when the antenna is moved in the y-axis in order to perform a new scan (i.e. from scan B or C), range curvature occurs in the y-direction in the same way as explained in section 4. Therefore, correction of the data in that direction is necessary. These changes in the responses, are a problem that has to be solved if automatic object recognition is to be performed.
2. –The response from object 9 is similar to the response of the plastic mine, therefore it can be mistakenly considered as a possible buried mine.
3. –Not all of the buried rocks appeared in the image since there are located out of the scanning path.

7.6 Experiment 6. Comparison with clutter reduction techniques.

Objective: To visually compare the quality of the images obtained with the presented algorithm against images obtained with the conventional SAR image formation method and with the following clutter reduction techniques:

1. – Complex average subtraction.
2. – Pre-recorded complex reference matrix subtraction.

Conditions:

All of the images were generated from the same complex raw data obtained from experiment 1. The images obtained with the three clutter reduction techniques were generated by applying range processing (without derivative), and SAR processing only. Refer to Figure 5.1.

Conventional SAR image formation with time window

The conventional SAR image formation process was applied in order to generate an image. In this case, no reference data is subtracted. Therefore, the image is expected to show strong responses from the sand surface which obscure the weak reflections from the plastic landmine as shown in Figure 7.35. In order to attempt to enhance the response of the mine, an early time (range) window [3] is applied to the data to set to zero all the range bins from the surface. The result is observed in Figure 7.36.

Complex average subtraction

In this case, the complex data from scan 1 of experiment 1 is used because it contains the responses from the sand without any buried object. Hence, two complex images were generated by the conventional method: one for the case of sand alone, and the other for the case in which an object is buried in sand. From the sand-only data, a single complex average column is obtained by averaging the data matrix in the cross-range direction. Then, the obtained average column is subtracted from each of the columns of the data containing a buried object [13]. The absolute value is then displayed as shown in Figure 7.37.

Pre-recorded complex reference subtraction

As in the previous case, the complex data from scan 1 of experiment 1 is used because it contains the responses from the sand without any buried object. Hence, two complex images were generated by the conventional method, one for the case of sand alone, and the other for the case in which an object is buried in sand. Then, the sand-only complex matrix is subtracted from the complex matrix containing the responses of the buried object in order to attempt to keep only the responses from the buried objects [5]. The absolute value is then displayed as shown in Figure 7.38.

Results:

Figures 7.35 to 7.39 show the obtained images.

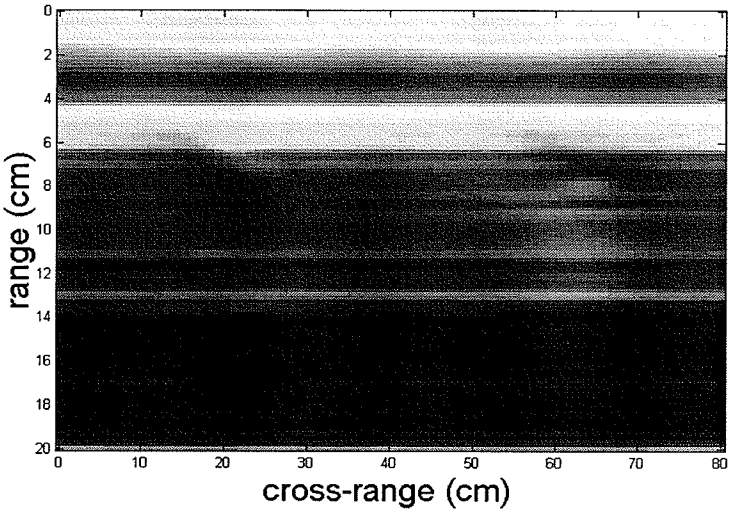

Figure 7.35 Image obtained with the conventional SAR image formation method.

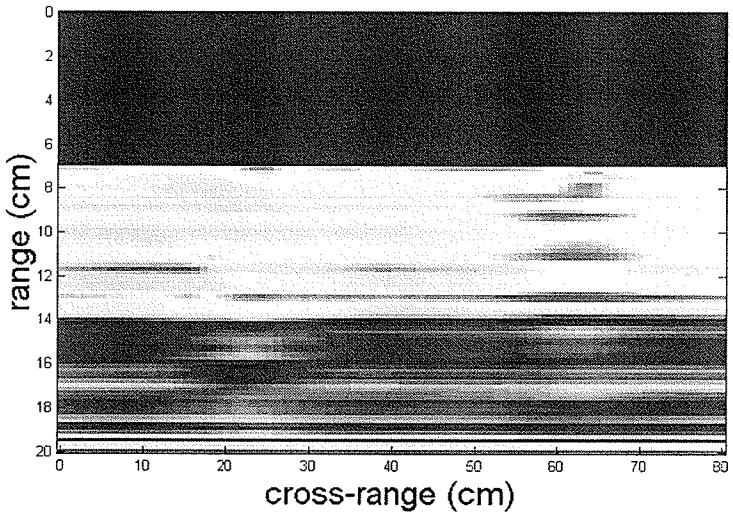

Figure 7,36 Conventional image formation method with time window.

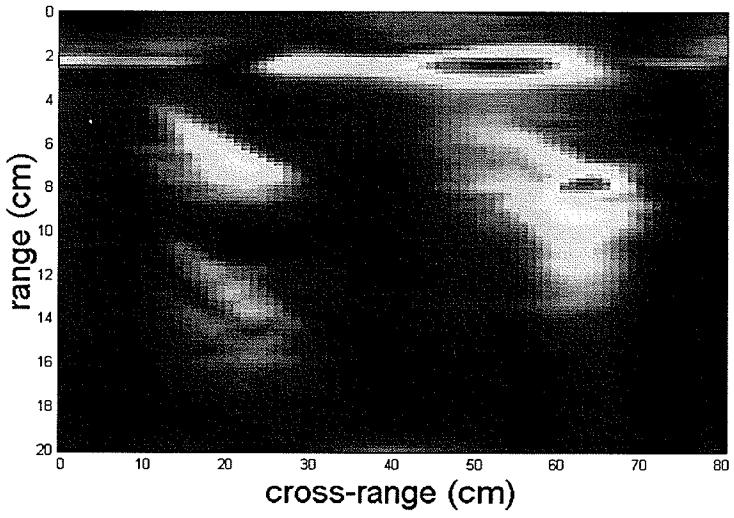

Figure 7.37 Image obtained with the complex average subtraction method.

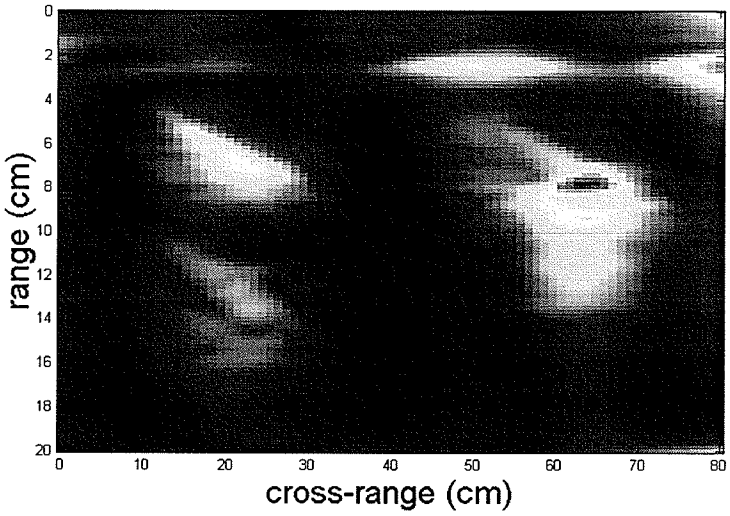

Figure 7.38 Image obtained with the pre-recorded complex reference matrix subtraction method.

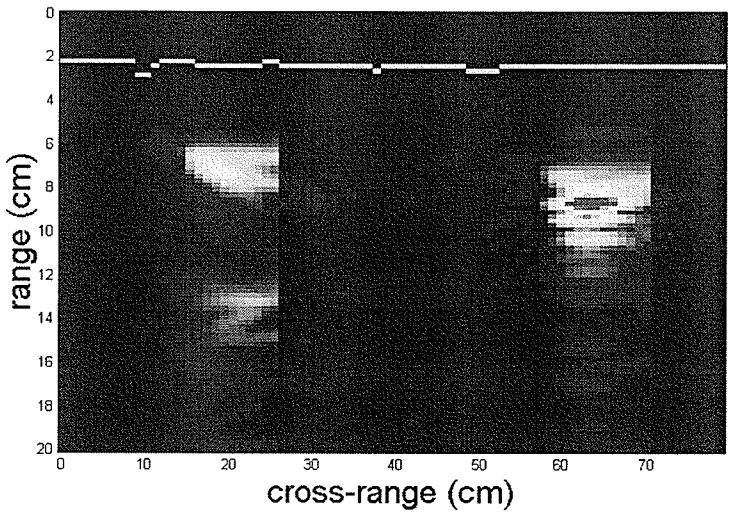

Figure 7.39 Image obtained with the algorithm developed in this thesis.

Conclusions from experiment 6

1. -It is very difficult to visually locate the reflections of the plastic mine in the image formed with the conventional method. The surface responses clearly dominate the image, and the weak responses from the mine are obscured. Even if a range window is applied, it is still difficult to visually identify the presence of the mine.
2. –The complex average column subtraction effectively reduces the responses from the sand, hence enhancing the responses from the buried objects. Some responses from the surface produced by the subtraction will still occur. However, a time window can be used to remove them.
3. –In the case of the image generated with the pre-recorded complex matrix subtraction, it can be noticed that the results are quite similar to those from the complex average subtraction. However, the same problem occurs: if there are differences in the conditions of the sand in the stored reference matrix and in the new collected data, other responses appear. For the surface responses, a time window can be used here too.
4. –The image obtained with the proposed algorithm has better visual quality than the other images.

8. Object Recognition

Although the focus of this work is the formation of GPR images in real time to enhance the reflections of weak reflecting objects rather than pattern recognition, a simple signature detection system was implemented. In this system, a small signature matrix containing the known responses of a buried landmine in sand is extracted from a GPR image, as shown in Figure 8.1. This signature matrix is stored in order to be correlated with images while they are being formed. A fast correlation is performed in the range direction between the signature and a set of columns of the image under formation. A threshold is applied to the resulting peaks from the correlation and a set of range bins is obtained which indicate the locations of possible buried landmines. The next step is to compute the mean square error between the landmine signature and each sub-area of the image with the same size of the signature, which is centered at each range bin obtained from the correlation. The lower the value of the MSE, the more likely is that a mine with a similar signature is present in that area of the image. When the MSE value is lower than a specified level, a frame is drawn in the image in order to indicate the location of the possible mine. Figure 8.2 shows how the signature is correlated while the image is being formed, and Figure 8.3 shows an actual mine detected in the image from Figure 7.8.

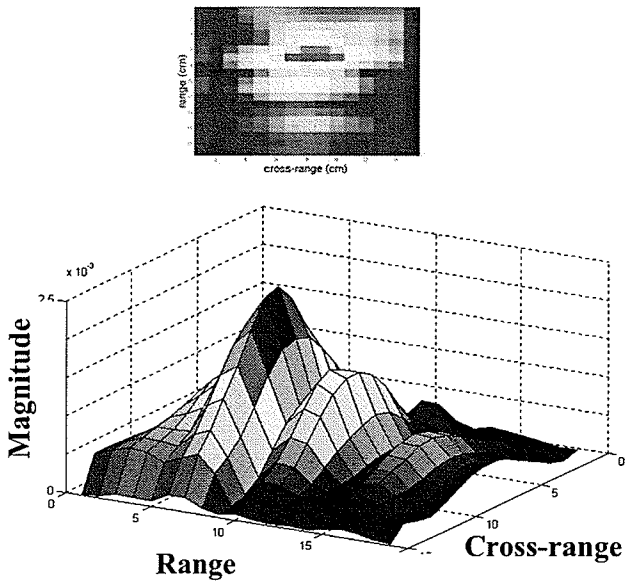

Figure 8.1 Extracted signature matrix (top). Surf plot of the signature (bottom).

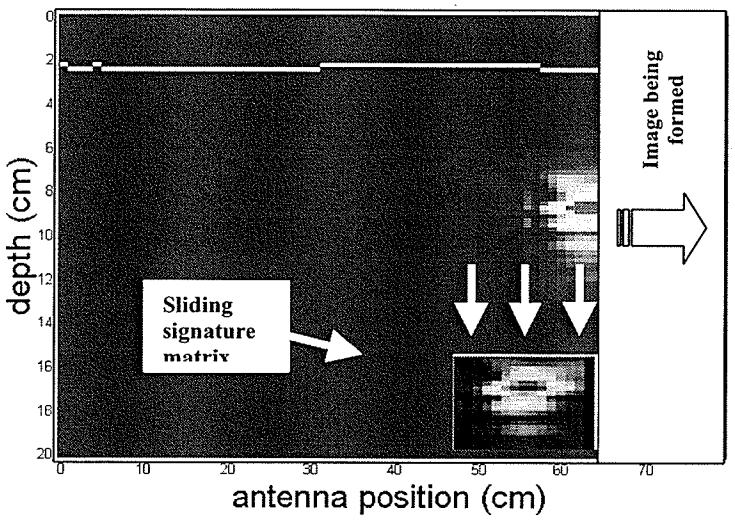

Figure 8.2 Fast correlation being applied between a signature and an image being formed.

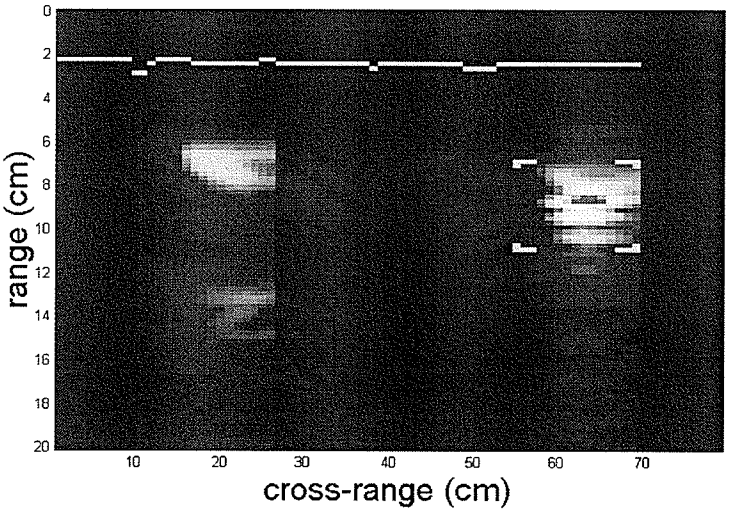

Figure 8.3 Plastic mine of fig. 7.8 detected with a signature matrix.

Although this system works, it is not robust. All of the images of the landmine shown so far were generated with the same mine orientation, which is as shown in Figure 7.2. If the mine is tilted or rotated, the shape and magnitude (i.e. the pattern) of its response in the GPR image will change. Furthermore, the response will also change if the mine is located

off-the scanning path, or if it is buried at different depths as shown in the experiment 2 of the previous section. Therefore, the automatic landmine pattern recognition is left as a future research point, since it requires a considerable amount of research and experimentation, which is out of the scope and time constraints of this thesis.

9. Bandwidth extrapolation

The bandwidth supported by the GPR hardware shown in Figure 3.1 offers a range resolution that is limited by the total number of frequencies sent and by the frequency step size of the system. Higher resolution will be obtained with the development of a second version of the hardware by expanding its operational bandwidth. However, considering that achieving larger bandwidths is directly related to higher costs and hardware complexity, the bandwidth of the second version of the hardware is not expected to be significantly larger. Hence, this section presents a signal processing technique, which attempts to further increase the range resolution.

The use of superresolution in GPR systems has been suggested before [14]. The majority of modern spectral estimation techniques used in radar signal processing which obtain higher resolution are based on the extrapolation of the signal [15, 16, 17]. A technique to improve resolution was shown in [18]. The data was extrapolated using a parametric method and it is explained next.

The range resolution of the obtained range profiles was given in section 4 as

$$\Delta rs = \frac{c_{sand}}{2 \cdot N \cdot \Delta f}, \tag{9.1}$$

where the product of the number of steps N, and the selected frequency step size Δf, can not exceed the maximum bandwidth supported by the GPR hardware. After a burst containing N pairs of I and Q data is collected, the spacing between each pair of data in the frequency domain is Δf. If more bandwidth were available, then additional I and Q samples with the same spacing could be appended into the data vector, in order to increase its length. However, since this can not be achieved with the hardware, then the available data vector is extrapolated in the frequency domain.

Let $S(k)$ be a data vector containing N pairs of I and Q samples. Then a predicted value of $S(k)$ can be obtained as

$$\hat{S}(k) = -\sum_{i=1}^{p} a_p(i) \cdot S(k-i) \ . \tag{9.2}$$

where, a_p is the *pth* prediction coefficient of the one-step linear predictor and p is the predictor order. In order to obtain the prediction coefficients a_p that minimize the error

between the predicted and the actual $S(k)$ values the Burg method is used in this work in order to compute the reflection coefficients based on the minimization of the error.

Once the a_p coefficients are obtained, the available samples from $S(k)$ are extended by applying (9.2) as

$$\hat{S}(k) = -a_1 S(k-1) - a_2 S(k-2) - \ldots - a_p S(k-p). \tag{9.3}$$

Hence, an estimation of the future values of $S(k)$ can be obtained based on the past values. These estimated values are considered as an extrapolated portion of the signal. In order to illustrate the extrapolation process with GPR data, consider the following example:

An I and Q data vector $S_1(k)$ containing the responses of a plastic mine buried in sand is available, which was obtained with the network analyzer with a start frequency $f_o = 1\,\text{GHz}$, end frequency $f_{end} = 7\,\text{GHz}$, and N=501 steps. Then the available bandwidth is $\beta_1 = 6GHz$ and the frequency step is Δf = 12MHz. If a vector $S_2(k)$ is defined by taking the first half of the data points from $S_1(k)$, then $S_2(k)$ can be viewed as an I and Q data vector of length M obtained with a GPR system with a lower bandwidth of $\beta_2 = 3GHz$. Hence, if (9.2) is applied to $S_2(k)$, for $k = M$+1 to L, where L is the desired extrapolated length, then M new predicted I and Q data values will be obtained which will produce an extended data vector $S_3(k)$. Figure 9.1 shows the plots of the real part (I channel) of the data vectors from this example. The plots were generated from actual data, and the mean square error between $S_1(k)$ and $S_3(k)$ was computed for 240 values of p. The order was then chosen to be $p=110$, based on the minimum MSE obtained in the plot of Figure 9.2. Although the extrapolated part of $S_3(k)$ is not identical to $S_1(k)$, these values were generated from the previous values of the vector, and therefore, it will be attempted to use them to improve range resolution.

If a GPR image is obtained using a 1-GHz bandwidth, then it will look like the one shown in Figure 9.3. The image shows a plastic mine buried 5cm in sand with a flat surface obtained by the conventional SAR image formation method explained in section 4. The network analyzer was used, in order to transmit 501 frequencies, starting from $f_o = 1\,\text{GHz}$, up to $f_{end} = 2\,\text{GHz}$, which yield the 1-GHz bandwidth supported by the

GPR hardware mentioned before. The average complex column subtraction clutter reduction technique explained in the previous section was applied to the data.

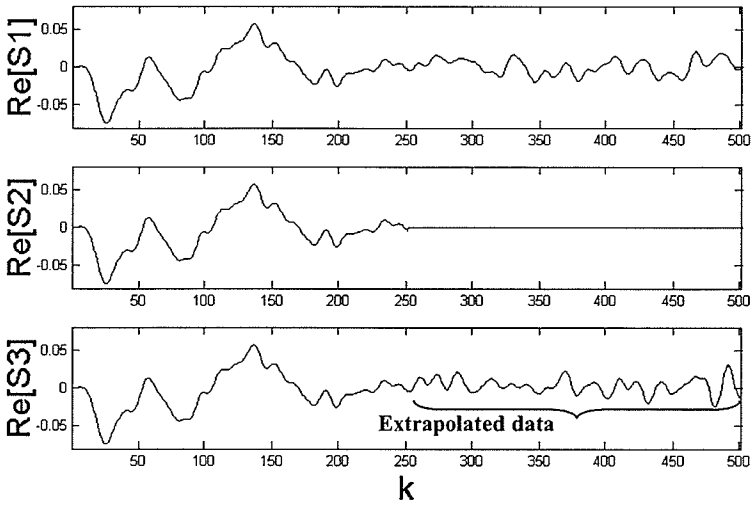

Figure 9.1 S1 vector obtained with a 6GHz bandwidth system (top), S2 vector obtained with a 3GHz bandwidth system (middle), S2 vector extrapolated to 6GHz (bottom).

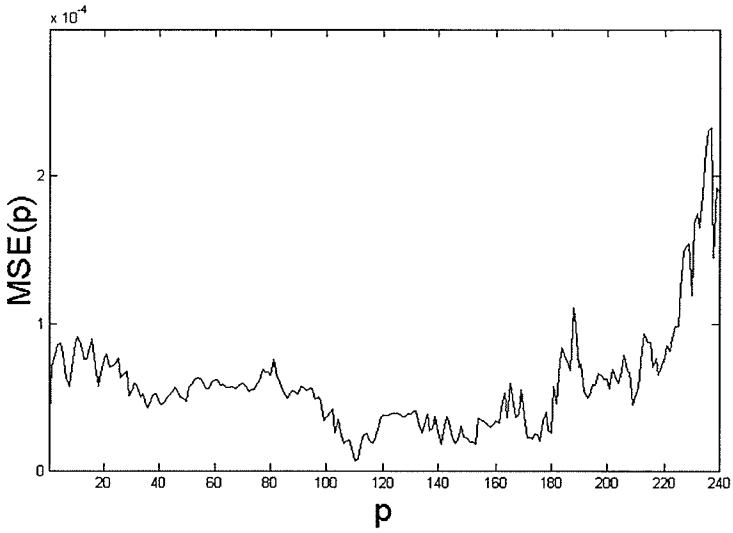

Figure 9.2 Mean square error plot used to select the order p in the extrapolation of the vector S2.

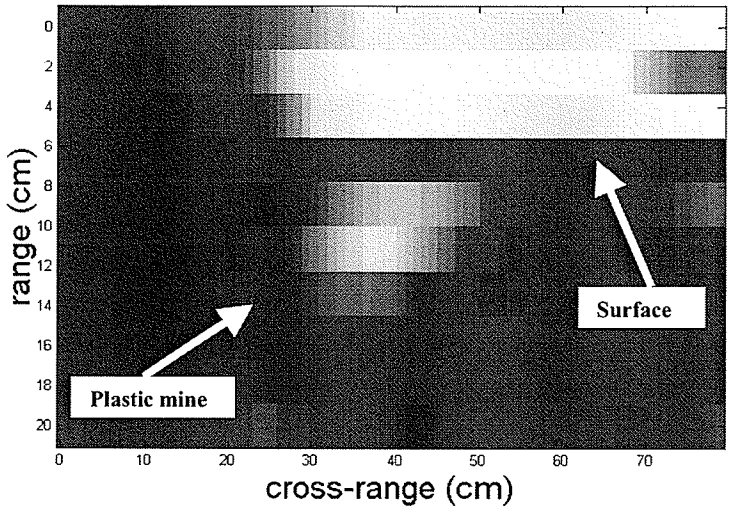

Figure 9.3 Image of a buried mine obtained with a bandwidth of 1GHz by using the SAR image formation method explained in section 4.

By using (4.3), the available range resolution is $\Delta rs = 8cm$ cm, assuming an approximate sand permitivity of $\varepsilon = 3.5$. Assuming that a new version of the hardware is developed which supports a bandwidth of 3GHz, then, the obtained image would look like the one shown in Figure 9.4. Then, by using (9.1) to attempt to extrapolate the bandwidth up to 6GHz, the obtained image would look like the one shown in Figure 9.5. As it can be noticed, the resolution is improved. However, there is a price to pay, which is the appearance of undesired responses in the image (i.e. artifacts). They occur since the same order p was used for each data column, even though the frequency response at each GPR cross-range location over the ground was different, then increasing the prediction error in the extrapolated data. For this reason, the extrapolation process was not considered in the algorithm presented at section 5. However, further research has to be done in order to improve the accuracy of the extrapolation for off-line processing of the data.

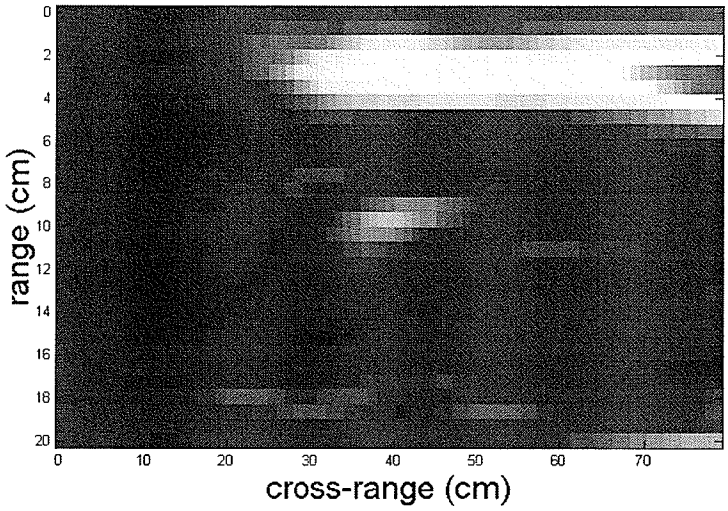

Figure 9.4 Image of a buried mine obtained with a bandwidth of 3GHz.

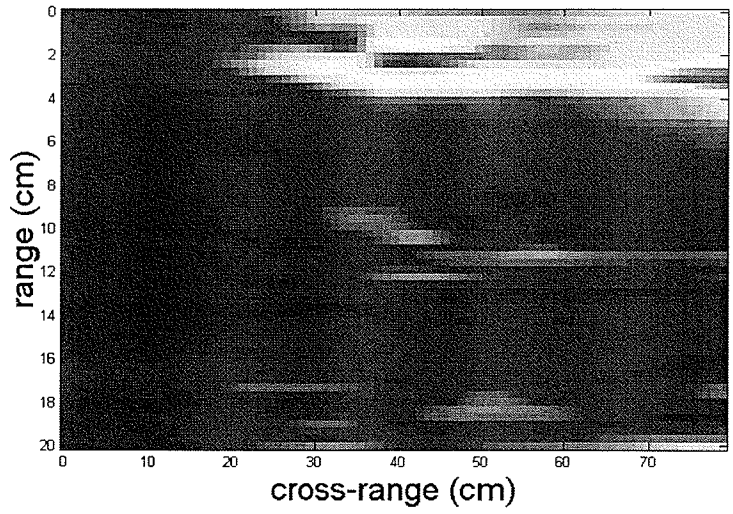

Figure 9.5 Image obtained by extrapolating the bandwidth from to 6GHz.

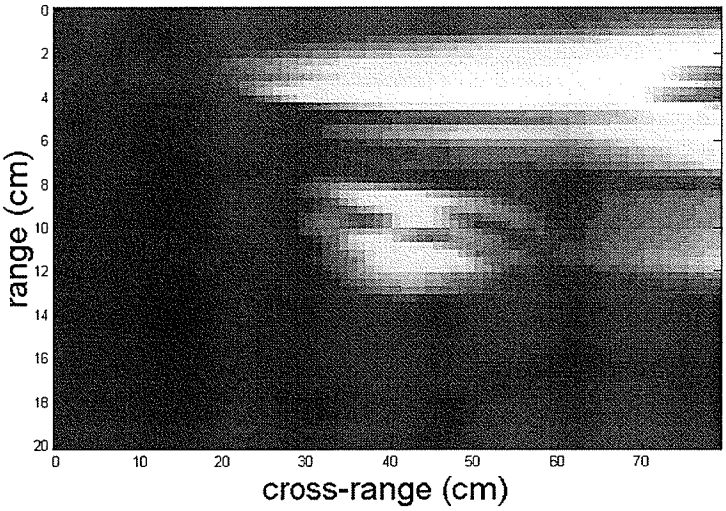

Figure 9.6 Image of a buried mine obtained with a bandwidth of 6GHz.

10. Conclusions

This thesis has introduced a digital signal processing algorithm that generates two-dimensional focused radar images of weak reflecting objects buried in sand. Although a low contrast exists between the plastic landmine and the sand responses, the algorithm was able to enhance the weak responses of the landmine in the obtained images. The proposed surface removal method outperforms a simple fixed time window. Because it tracks the surface in order to remove adaptively its responses, it allows the responses from shallow objects to appear in the image.

The main advantages of the proposed system are that images of buried weak reflectors are obtained without the need of a pre-scanned complex matrix as in the case of the mentioned clutter reduction techniques, and that the system is implemented in real time. The results from the performed experiments have confirmed the functionality of the system and objects can be imaged at their correct depth and cross-range locations with flat and rough surfaces. The selection of the thresholds depends on the terrain characteristics. A trial scan can be performed over a ground area of the terrain in order to observe the mean square error plots in order to decide the threshold values. The reference update can be eventually refreshed manually. Although SAR focusing applied in GPR is not found often in the literature, this work showed that it worked effectively and helped achieve the required cross-range resolution. However, a good estimate of the permitivity of the medium and a definition of a focusing region are required. No objective image quality metric such as the Peak Signal to Noise Ratio (PSNR) was used in this work because of the lack of a reference image. However, the obtained images have a better visual quality than the ones obtained with the clutter reduction techniques mentioned in [3, 5, 13]. Although a simple system was implemented for target signature recognition, the signature of the object under search changes drastically with depth, location, angle, and surface conditions. Furthermore, in some cases other objects such as rocks show responses similar to those from the landmines which can cause misclassifications. The object recognition is left as an interesting future research topic. A method to attempt to increase the range resolution of short-bandwidths systems was presented. Although it was not implemented because of the computation time requirements, further research has to

be performed in order to reduce the prediction error in the extrapolation in order to obtain better images.

The drawbacks of the system presented in this thesis are that the imaging of shallow objects is limited by the surface removal method and that the system requires a high bandwidth.

Some future research topics include imaging in wet sand, motion compensation for continuous scanning in cross-range, parallel processing and 3-D GPR imaging.

References

[1] K.O'Neill, "Radar Sensing of Thin Surface Layers and Near-Surface Layers and Near-Surface Buried Objects". IEEE Transactions on Geo Science and Remote Sensing, Vol. 38, No. 1, January 2000.

[2] G.Farquharson, A. Langman, M.R. Inggs, "Detection of Water in an Airport Tarmac using SFCW Ground Penetrating Radar". IEEE 1999.

[3] A. van der Merwe, J.Gupta, "A Novel Signal Processing Technique for Clutter Reduction in GPR Measurements of Small, Shallow Land Mines", IEEE Transactions on Geoscience and Remote Sensing, Vol. 38, No. 6, November 2000.

[4] Y.Sun, J.Li, "Time-Frequency Analysis for Plastic Landmine Detection via Forward-Looking Ground Penetrating Radar", IEE Proceedings-Radar, Sonar and Navigation Special Issue on Time-Frequency Analysis for Synthetic Aperture Radar and Feature Extraction, 2002.

[5] R.Wu, et al, "Adaptive Ground Bounce Removal", IEE 2001, Electronics Letters Online, No: 20010855.

[6] D. M. Pozar, Microwave Engineering Second Edition, John Wiley & Sons, 1998.

[7] H. Feng et al, "A Statistical Approach to Rough Surface Underground Imaging", IEEE 2000.

[8] S. Peters, et. al. Design and testing of a 1-3 GHz SFCW ground penetrating radar

[9] J.Proakis, D.Manolakis, Digital Signal Processing, Upper Saddle River, NJ, Prentice Hall, 2002.

[10] R.Gonzalez, R.Woods, Digital Image Processing, Upper Saddle River, NJ, Prentice Hall, 2002.

[11] G. W. Stimson, Introduction to Airborne Radar Second Edition, Mendham, NJ, SciTech Publishing Inc, 1998.

[12] D. R. Wehner, *High-Resolution Radar*, Artech House, Norwood, MA, 1995.

[13] R. Caldecott, J. D. Young, J. P. Hall, A. J. Terzouli, "An underground obstacle detection and mapping system", Tech. Rep. EL-3984, ElectroSci. Lab., The Ohio State Univ. and the Elect. Power Res. Inst., Palo Alto, CA, May 1985.

[14] S.M. Shrestha, I. Arai, T. Miwa, and Y. Tomizawa, "Signal processing of ground penetrating radar using super resolution technique," IEEE Radar Conference, pp 300-305, 2001.

[15] S.R. DeGraaf, " SAR Imaging via Modern 2D Spectral Estimation Methods," *IEEE Trans. on Image Processing*, Vol. 7, No. 5, May 1998.

[16] H. C. Stankwitz, and M. R. Kozek, "Superresolution for SAR/ISAR RCS Measurements Using Spatially Variant Apodization," *Proc. AMTA Symp.*, Williamsburg, VA, Nov. 1995.

[17] S. D. Cabrera, B. C. Flores, E. Rodriguez, and G. Thomas, "Two-Dimensional Extrapolation and Spectral Estimation from Arbitrary Sampling Configurations for SAR/ISAR Imaging," IEEE Proc. ASILOMAR, Pacific Grove, CA, USA, November 1994.

[18] G.Thomas,E.Corral,J.LoVetri, "High Resolution Imaging Using a SFCW GPR", America Electromagnetics 2002 Conference AMEREM'02, Annapolis, Maryland, U.S.A., june, 2002

[19] J. M. Reynolds, *An Introduction to Applied and Environmental Geophysics*, John Wiley & Sons, New York, 796 pp.

[20] B. Sai, I. Morrow, P. van Genderen, "Limits of Detection of Buried Landmines on Local Echo Contrasts", Delft University of Technology, Faculty of Information Technology and Systems, International Research Centre for Telecommunications-transmission and Radar, The Netherlands.

APPENDIX A (Signal Processing Matlab Code)

```
%*************************************************************************
% UM Ground-Penetrating Radar Imaging System
% By: Eduardo Corral (student # 6774732)
% The University of Manitoba, Canada
% Dept. of Electrical and Computer Engineering
%
% Description: This code implements the algorithm presented in the thesis. It processes an
%              incoming IQ complex data vector whith length N in order to generate a column of
%              a GPR image. The displayed image is updated each time this code runs.
%              The code runs once in each call from a GUI
%*************************************************************************
%function New_program_with_focusing(T1,T2)
%New_program_with_focusing(4e-10,1.2e-8)
T1 = 4e-10;
T2 = 2e-8;
ifft_desired_length = 4*501;

% Load pre-recorded sampled data in order to work off-line
% Experiment 1
 load Thesis_Exp1_SR_R1_M1

% The following matrices are initialized in when the GUI is started:
unprocessed_data = ''; %
focused_data = '';
derivative_data ='';
subtraction_data = '';
Image_focused = '';
Image_derivative = '';
Image_subtraction = '';
Synthetic_aperture_matrix ='';
Azimuth_sum ='';
sig_MSE = '';  % Empty MSE vector for object recognition
ref_image_column = ''; %OK
rMSE_vector=''; %OK
sMSE_vector=''; %OK
freq_start = 1e9;
freq_end = 12.4e9;

for scan = 1:size(NA_raw_data,2) % <--For off-line processing of pre-recorded data

 S = NA_raw_data(:,scan); % Incoming IQ complex data vector

%*************************************************************************
% For real time processing:
%clear data_vector;
% S = ( I_channel + j*Q_channel ).';  % Incoming IQ complex data vector
unprocessed_data = [unprocessed_data S];

%*************************************************************************
% INITIALIZATION
%Do this ONLY ONCE. (When the very first scan is performed)
%*************************************************************************
if (isempty(ref_image_column)) & (isempty(Synthetic_aperture_matrix))
'Initializing parameters...'
%-------------------------------------------------------------------------------------------------------------------
% System / Range Parameters
N = size(S,1);  % Length of incomming vector
Bandwidth = freq_end - freq_start;
delta_F = Bandwidth / (N-1);  %frequency step
```

```
epsilon_sand = 3.5; % Estimated permitivity of the ground
c_sand =  sqrt(1/(epsilon_sand * 8.854e-12 * 4*pi*1e-7)); %Estimated traveling speed in sand
c_air = 3e8; %Traveling speed in free-space
rng_extent =  c_sand / (2*delta_F); %Unambiguous range (meters) extent covered with this delta_F
range_resolution =  c_sand / (2*Bandwidth); % Will be used to adjust image scale
%ifft_desired_length =  512;  % <====== times the data length
ifft_one_bin_length_meters = rng_extent / ifft_desired_length; %Length of one bin in the ifft
dint = 0.2;   %range of interest in meters (desired depth to be imaged)
range_bins_of_interest = round(dint / ifft_one_bin_length_meters); % # bins in the range of interest
range_display_vector = 100 * linspace(0, dint, range_bins_of_interest); %to adjust display axis

%-------------------------------------------------------------------------------------------------------------------
% Phase correction Parameters (system delay)
cable_length = 10.8; %meters
antenna_length = 0.12; %meters
dist_antenna_sand = 0.03; %meters
other_system_delays = 5.76; % other delays
dsyst = 2*cable_length  +  2*antenna_length + 2*dist_antenna_sand + other_system_delays; %total distance
% Create exponential vector to correct the signal phase shift due to traveled distance
E = ( exp( j*2*pi* (dsyst/c_air)*delta_F *[0:N-1]) ).';

%-------------------------------------------------------------------------------------------------------------------
% Surface detection Parameters
surface_check=''; %Vector used to search for the surface bin
surf_bin_a = 0;
clear surf_temp
dx = 0.03; % distance in which the surface will be searched for
surface_search_region_bins = round( dx / ifft_one_bin_length_meters);
dus = 0.02; % distance under the surface which will be discarded since it contains surface noise
under_surface_subtr_start_bin = round( dus / ifft_one_bin_length_meters);
%-------------------------------------------------------------------------------------------------------------------
% SAR Parameters
mx_step_size_cross_rng = 0.01;  % Cross-range step size
cross_rng_interpolation_factor = 2;
L_aperture_length = 20 + 1;  % SAR aperture: 21 bins --> 21 cm
R = 0.05;  % <== Range of the focusing region
Xcenter = ceil(L_aperture_length/2);  % Center column in the Synthetic Array

dF_sar = (ifft_desired_length/N) * delta_F;  % frequency step
f_sar = dF_sar;
dfoc = dus; % distance from which focusing is started
focus_start_bin = round(dfoc/ifft_one_bin_length_meters); %

Esar =  (0 * Synthetic_aperture_matrix) + 1 ; %Prepare empty matrix of same dimensions

% fill in the correction matrix
for a = 1 : range_bins_of_interest
  y=-(mx_step_size_cross_rng/cross_rng_interpolation_factor) * Xcenter;%cell cross-rng distance
  for b=1:(L_aperture_length * cross_rng_interpolation_factor)-1 % -1 because the first column
                                                                 % was not interpolated
     Esar(a,b) = exp(j*4*(pi/c_sand)* (sqrt(R.^2 + y.^2) - R) * f_sar );
     % Esar(a,b) = exp(j*4*(pi/c_sand)* ( y.^2 /(2*R) ) * f_sar ); % Another way to do it
     y = y + (mx_step_size_cross_rng/cross_rng_interpolation_factor);
  end
  f_sar = f_sar + dF_sar;
end
%-------------------------------------------------------------------------------------------------------------------
% Low-Pass Filter Parameters (Optional)
freq_norm = 0.12; %Cut-off freq
LPF_order = 30;
LPF_b_coeffs = fir1(LPF_order, freq_norm); % Uses hamming window by default
LPF_a_coeffs =1;
```

```
%-------------------------------------------------------------------------------------------------------------
% Object recognition (Optional)
% load signature
%[sig_rows, sig_cols] = size(signature); %Get the dimensions of the signature
%sig_pixels = sig_rows * sig_cols; % Total # of cells in the signature
%ha = round(sig_rows/2);
%hb = round(sig_cols/2);
%sig_norm = (1/max(max(signature)) )* signature;  %Normalize signature
%signature2 = conj( flipud(signature) ); %Flip, complex-conjugate for the fast correlation
%sig_padd = zeros(range_bins_of_interest + sig_rows,sig_cols);% Padding: make s of the same length as I
%sig_padd(1:sig_rows,1:sig_cols) = signature2;  % Copy the signature
%I_window = 0 * sig_padd;  % Initialize empty matrix, same size as s
%sig_padd_fft =  fft(sig_padd); % Go to the frequency domain
%mark_Len = 2; %cells length of the frame lines to be drawn when object is detected
end % end of : if (isempty(ref_image_column)) .
%-------------------------------------------------------------------------------------------------------------

tic

%*****************************************************************************
% NA Cables Delay removal (shift) .
%*****************************************************************************
Scorr = E .* S; % <-- Correction is done here

%*****************************************************************************
% LOW-PASS Filter (Optional)
%*****************************************************************************
Scorr = filter(LPF_b_coeffs,LPF_a_coeffs,Scorr);

%*****************************************************************************
% IFFT & Remove (Truncate) unwanted right-side bins which are beyond the desired range
%*****************************************************************************
scorr =  ifft(Scorr, ifft_desired_length) ; % Zero-padded FFT for better display
scf =  real(scorr(1:range_bins_of_interest ) ); % Keep only the bins of interest

%*****************************************************************************
% Apply first derivative in the rows direction (range direction)
%*****************************************************************************
sder = '';
for d=2:range_bins_of_interest
   sder = [sder; [scf(d) - scf(d-1)];];
end
sder = [sder(1); sder;]; % Vector containing the first derivative of the range profile

%*****************************************************************************
% Interpolate in Cross-Range direction (one column only), and append the incomming vector
% and the interpolated vector into our Synthetic_aperture_matrix
%*****************************************************************************
SAR_length = size(Synthetic_aperture_matrix,2); % Get the current size of the SAR array

  if ( SAR_length >= 1 )
     % Interpolate only if the SAR array has more than one columns
     inter = 0.5 * (sder + Synthetic_aperture_matrix(:,end)); % Average of new and last columns
     % Form the Synthetic Array short matrix
     Synthetic_aperture_matrix = [Synthetic_aperture_matrix  inter  sder]; %Append columns
  else
     % Dont interpolate the very first time, since there's no "last column" yet
     Synthetic_aperture_matrix = [Synthetic_aperture_matrix  sder]; % Append the very first one
  end

  % If the SAR array is full:
```

```
  % Update the Synthetic Aperture, discard the oldest column since the antenna has moved on
 if ( (SAR_length + cross_rng_interpolation_factor) >= ((L_aperture_length * cross_rng_interpolation_factor)+1)  )
   Synthetic_aperture_matrix = Synthetic_aperture_matrix(:,cross_rng_interpolation_factor + 1:end );
   % Apply the azimuthal phase correction by point-to-point multiplication in the frequency domain
   sarf = ifft( Esar .* fft(Synthetic_aperture_matrix) ); %Range-corrected SAR array
   % Integrate horizontally
   scmp = sum(sarf,2); %single Azimuth-compressed column
   %Replace surface bins with original ones because they are needed for surface detection
   scmp(1:focus_start_bin) = Synthetic_aperture_matrix(1:focus_start_bin,round((L_aperture_length-1)/2));
   image_column = abs(scmp); % Prepare the new image column



%*************************************************************************
% Apply the adaptive reference subtraction algorithm
%*************************************************************************
% If no reference column exists (we are at the beginning of the image), then create it.
if (isempty(ref_image_column))

  sref = scmp;  %Create initial reference
  ref_image_column = image_column; %<--Create Initial Reference vector

else % A previously-generated reference vector exists, Start the normal process...

  if (isempty(focused_data)) % is the data matrix empty still?
    cross_rng_difference = scmp - sref;  %Only the first time: subtract using reference
  else   % if matrix is not empty...
    cross_rng_difference = scmp - focused_data(:,end); % Derivative in cross-range direction
  end

    derivative_image_slice = abs(cross_rng_difference); % Generate a range profile

    % Estimate the bin of the sand's surface:
    %-------------------------------------------------------------------------
    surf_temp = derivative_image_slice(1:surface_search_region_bins); %Get vector with the
                                                                      %first range bins
    surf_max_value = mean(max(surf_temp));
    surf_max_bin = find(surf_temp == surf_max_value) ; % Find the one bin with highest
                                       %magnitude
                                       % mean is used because there can be more than one bins
    surface_check = [surface_check max(surf_temp)]; % Store the surface response values

    if (isempty(focused_data)) % is the data matrix still empty?
      surf_bin_a = surf_max_bin; % Initialize previous columns surface bin
      deeper_surface_bin = surf_bin_a; % So far this is the deepest surface bin
    else
      if  (surf_max_value > 5e-6) % If the transition is higher than a threshold...
        surf_bin_b = surf_max_bin; % The new surface bin
        % Compare the current surface bin against the previous column's surface bin
        deeper_surface_bin = min([surf_bin_a surf_bin_b]); %Get the deepest one
        surf_bin_a = surf_bin_b; %update the "last" surface bin
      else
        % If the transition is very low (No change)
        surf_max_bin = surf_bin_a; % The new surface bin will be equal to the previous one
        deeper_surface_bin = surf_bin_a;
      end

    end
    %-------------------------------------------------------------------------

    ssub = scmp - sref; % Apply reference subtraction
```

```
    new_image_substr_slice = abs(ssub);% Generate a range profile from the result
    %ELIMINATE SURFACE
    new_image_substr_slice(1:deeper_surface_bin + under_surface_subtr_start_bin) = 0;

    %Get the existing image's dimensions
    Ne = length(image_column); %rows

    if (isempty(Image_focused)) %
       rMSE =  (1/Ne) .* (sum(  (abs(ssub)).^2 ));
       sMSE =  rMSE;
    else %Compute mean square errors of the response differences under the ground...
       rMSE =  (1/Ne) .* (sum((abs(cross_rng_difference(deeper_surface_bin + under_surface_subtr_start_bin:end))
).^2));
       sMSE =  (1/Ne) .* (sum((abs(ssub(deeper_surface_bin + under_surface_subtr_start_bin:end)) ).^2));
    end

       %Make MSE vectors
       rMSE_vector = [rMSE_vector rMSE];
       sMSE_vector = [sMSE_vector sMSE];

       %UPDATE the Reference
%        if( ((rMSE < T1)&(sMSE < T2)) | ((rMSE < T1)&(sMSE > T2)) )
       if( ((rMSE < T1)&(sMSE < T2)) )
          sref = scmp; % Update reference
          ref_image_column = image_column; %<--Create Initial Reference vector
       end
       new_image_substr_slice(surf_max_bin) = (7.5e-3) / 10; % Draw surface

       %Update Complex data matrices...
       focused_data = [focused_data scmp]; %Append focused column
       derivative_data = [derivative_data cross_rng_difference];
       subtraction_data = [subtraction_data ssub];

       %Update Absolute value data matrices...
       Image_focused = [Image_focused image_column ];% SAR-focused image
       Image_subtraction = [Image_subtraction new_image_substr_slice]; % Image after subtraction
       Image_derivative = [Image_derivative derivative_image_slice] ; % Image of derivative in cross-range

end %end of checking if reference is empty


toc


% Normalize with respect the plastic landmine maximum response

I = (255 / (3 * 2.5e-3) ) * Image_subtraction; % OUTPUT Image of the Algorithm


%*************************************************************************
% Object recognition (Optional)
%*************************************************************************
recognize = 0;

if (recognize==1) % Only run this code if recognize == 1
%*************************************************************************
[I_rows,I_cols] = size(I); % Get current dimensions
if (I_cols >= sig_cols)  % Continue only if image I has enough columns to fit the signature in it
 right_col = I_cols;
 left_col  = right_col - sig_cols + 1;
 I_window(1:I_rows,:) = I(:, left_col : right_col); %Copy next set of columns from I
 corr_F =  fft(I_window) .* sig_padd_fft ; % FFT, multiplication in freq domain
```

```
corr = real(ifft(corr_F)); % Go back to time domain

% Detect peaks of correlation which are within the target's range
within = find( (corr > 14000) & (corr < 20000) );
[r_ctr c_ctr] =  find ( corr == (max( max(corr(within)) )) ); %Get the coordinates of the maximum
% If the coordinates exist (from a maximum) ...
if (isempty(r_ctr)==0)
   ctr_line = r_ctr - ha;  % Remove padding-related offset
   top_line = ctr_line - ha;
   %Compute MSE at this row
   T = I_window(top_line : top_line + sig_rows-1 , :); % Extract T
   T = (1/max(max(T))  ) * T; %Normalize it
   sig_MSE = [sig_MSE  (1/(sig_pixels)) * sum(sum( (sig_norm - T).^2 ))] ;

   if sig_MSE(end)< 0.045
     % Draw a rectangle around the detected signature
     for i = 1 : mark_Len
       I( ctr_line - ha-1 + i, left_col ) = 30  ;
       I( ctr_line + ha+1 - i, left_col ) = 30  ;
       I( ctr_line - ha-1 + i, right_col ) = 30  ;
       I( ctr_line + ha+1 - i, right_col ) = 30  ;
       I( ctr_line - ha , left_col + i) = 30  ;
       I( ctr_line - ha , right_col - i) = 30  ;
       I( ctr_line + ha , left_col + i) = 30  ;
       I( ctr_line + ha , right_col - i) = 30  ;
     end
   end
 end  % (isempty(r_ctr)==0)

end % if (I_cols >= sig_cols)

%**************************************************************************
end  % if recognize==1

end  % if (isempty(ref_image_column))

end % end of :  ( (SAR_length + cross_rng_interpolation_factor) >= .....


%**************************************************************************
% DISPLAY SECTION
%**************************************************************************
if (~isempty(Image_focused))
m = size(Image_focused,2); %Get the new columns size of the new image
%cross_rng_display_vector = 100 * linspace(0, (mx_step_size_cross_rng/cross_rng_interpolation_factor)* m,m);
cross_rng_display_vector = linspace(0,m,m);
end

if (~isempty(Image_focused))
figure(1)
%COLOR                    ;
imagesc(cross_rng_display_vector,range_display_vector, Image_focused)
colormap('default')
% INVERTED, BLACK AND WHITE
%imagesc(cross_rng_display_vector,range_display_vector,(255/max(max(Image_focused))) *  (-1 * Image_focused +
max(max(Image_focused)))  )
%colormap('gray')
title('SAR-focused Image')
ylabel('depth (cm)','Fontsize',23)
xlabel('antenna position (cm)','Fontsize',23)
set(figure(1),'Color','w')  % Control figure color
end
```

```
if (~isempty(Image_subtraction))
figure(2)
image(10+cross_rng_display_vector,range_display_vector,I)
colormap('default')
title('Subtraction Image')
ylabel('depth (cm)','Fontsize',23)
xlabel('antenna position (cm)','Fontsize',23)
set(figure(2),'Color','w')  % Control figure color
end

if(~isempty(Image_derivative))
figure(3)
imagesc(cross_rng_display_vector,range_display_vector,Image_derivative)
colormap('default')
title('Derivative Image')
ylabel('depth (cm)','Fontsize',23)
xlabel('antenna position (cm)','Fontsize',23)
set(figure(3),'Color','w')  % Control figure color
end


if( (isempty(rMSE_vector)==0) & (isempty(sMSE_vector)==0) )
Thr_1 = T1 * ones(1,length(rMSE_vector));
Thr_2 = T2 * ones(1,length(rMSE_vector));

figure(4)
subplot(2,1,1)
plot(cross_rng_display_vector,rMSE_vector,'k', cross_rng_display_vector, Thr_1,'k')
xlabel('position(cm)','Fontsize',23)
ylabel('sMSE','Fontsize',23)
set(figure(4),'Color','w')  % Control figure color
axis([0 length(rMSE_vector) 0 max(rMSE_vector) ])
subplot(2,1,2)
plot(cross_rng_display_vector,sMSE_vector,'k', cross_rng_display_vector, Thr_2,'k')
xlabel('position(cm)','Fontsize',23)
ylabel('rMSE','Fontsize',23)
axis([0 length(sMSE_vector) 0 max(sMSE_vector) ])
set(figure(4),'Color','w')  % Control figure color
end


return
```